University of Sussex

Bio-magnetic imaging using highly sensitive quantum magnetometers

Aikaterini Gialopsou

Submitted for the degree of Doctor of Philosophy

University of Sussex

March 2022

Declaration

I hereby declare that this thesis has not been and will not be submitted in whole or in part to another University for the award of any other degree.

Signature: Aikaterini Gialopsou

_____

Date: March 2022

_____

UNIVERSITY OF SUSSEX

Aikaterini Gialopsou, Doctor of Philosophy

Bio-magnetic imaging using highly sensitive quantum magnetometers

Summary

This thesis describes the experimental results of highly sensitive quantum magnetometers, known as optically pumped magnetometers (OPMs), for bio-magnetic measurements. First, I show that commercially available OPMs can achieve enhanced spatio-temporal resolution compared to superconducting quantum interference devices (SQUIDs) when recording visual-evoked fields, using a standard visual paradigm. The improved resolution enabled the observation of novel neuronal findings in healthy participants. As OPMs were not originally developed for this neurophysiological application, the technology is not optimised for it, and the product design limits the final performance. In our lab, we developed a modular OPM sensor to surpass these limitations in terms of bandwidth and scalability. I tested the performance of this prototype for bio-magnetic measurements, and validated its use through a series of alpha-rhythm experiments over the visual cortex. Finally, I designed an experiment to explore the possibility of measuring the spinal cord evoked response using both the modular and the commercially available OPMs. Using peripheral nerve stimulations, I demonstrate the importance of the broader bandwidth for spinal cord measurements compared to the brain ones, and thus highlight the suitability of the modular OPM sensor for more sensitive measurements. Preliminary in-vivo spinal cord data using the commercial OPMs show simultaneous evoked fields of the brain and spinal cord.

Acknowledgements

I would like to thank my supervisors Peter Krüger and Mara Cercignani for their valuable guidance, help and the support through out the PhD project. I would also like to thank both School of Mathematical and Physical Sciences and Brighton and Sussex Medical School of University of Sussex for funding this interdisciplinary project.

This thesis would not have been possible without the support of friends and colleagues, who took the time to assist, provide advice and participate in my research. A big thank you to: Matt Withers, Chris Abel, Tom Coussens, Tim James, Shobita Bhumbra, Fedja Orucevic, Michael Woodley and everyone who helped, participated and offered their time, knowledge and efforts.

Lastly, I would like to thank my family, especially my partner and our cat for always being there, taking the anxiety away.

Contents

Chapter 1

Introduction

The human brain is not easy to comprehend, and it has been described as the most complex, multi-functional body organ (1). The human brain is malleable and adaptable and has been shaped by millions of years of evolution. Some of the earliest studies used post-mortem examinations to study the brain which provided the bases for the understanding its shape and structure (2). Technological progress of the past two centuries provided significant improvement in tools and techniques used to study the brain such that modern methods can study the structure and dynamics of the brain in-vivo (3; 4; 5). Computed tomography (CT) was introduced in the late 1970's and brought a revolutionary three-dimensional view of the brain structure, resulting in better identification of brain traumas or inflammations (6). Positron Emission Tomography (PET) was invented during the 1980s, utilizing radionuclides to detect any metabolic processes or changes in the brain (7). CT and PET are non invasive techniques and rely on the use of ionising radiation. The development of Magnetic Resonance Imaging (MRI) came a few years later (late 1970s) (8). In MRI a strong magnetic field is used along with radiofrequency waves that excite hydrogen atoms, resulting in detailed anatomical images of the body. Today, it is widely used to explore the brain's structural properties in research and clinical applications.

Thanks to the improved contrast between soft tissue provided by MRI, detailed anatomical images of the brain can be obtained. However, knowledge of anatomy is not sufficient to understand the human brain, and tools able to assess brain function are also needed. As neural activation produces current flows, neurophysiological techniques, namely electroencephalography (EEG) (9) and magnetoencephalo-

graphy (MEG)(10) can be used to measure instantaneous voltage and the magnetic fields generated by neural currents. An alternative way of measuring brain function is functional MRI (fMRI) (11; 12), further exploiting the MRI technology and correlating changes in the cerebellum blood flow to cortical activations.

Technological improvements in functional neuroimaging provided a more detailed characterisation of the neural patterns to an external stimulus (13), focusing on the spatial and temporal features of the response (14). The spatio-temporal attributes of a neurophysiological signal are crucial for a better understanding of the basic cortical circuits and for the early distinction between the physiological and pathological neural functions. The early detection of the pathological brain function provided reliable biomarkers for neurodegenerative diseases (15; 16) and could aid and prognosticate the treatment response or clinical progression (17).

Currently, available neuroimaging methods are hampered by intrinsically low signal strength and spatial or temporal resolution (18; 19). fMRI allows increased spatial resolution for activation mapping but has only moderate temporal resolution ($\sim 1\,\mathrm{s}$) (20). EEG allows real-time recordings of the concurrent neural changes but changes in electrical permittivity distort the spatial distribution of the electric signal, which degrades source localization. EEG is limited to a spatial resolution of $\sim 10\,\mathrm{mm}$ (21). Although MEG provides increased temporal and spatial resolution, the method is limited by weak cortical signals (pT to fT) whose amplitudes are comparable to noise sources, such as the Earth's magnetic fields (30-60 µT). This necessitates the use of magnetically-shielded rooms (MSRs) to attenuate the environmental magnetic fields to less than the detectable biomagnetic fields.

A beating heart produced the first biomagnetic signal ever recorded in the 1960s. For this measurement, Baule and McFee used two coils twisted around two separate ferrite cores as a sensor (22). These measurements were sensitive to urban noise and thus were recorded in an open field. Cohen continued this line of the experiment using similar sensors to record both the cardiac rhythm (23) and the first cortical signal(24) within a MSR, though the results were deemed too noisy. Soon after, SQUID sensors were developed by Jim Zimmerman (25) and the first magnetocardiography (MCG) signal using a SQUID sensor was recorded in 1970 (26). Three years after, the first distinguishable cortical biomagnetic signal was measured with

a single SQUID over the occipital lobe (4), leading the way to the commercialised cortical neuroimaging method known as MEG.

Since the first measurements, SQUID technology and MEG applications have been widely used for a better understanding of the central nervous system (CNS) and cardiovascular system. Recent studies indicated through MEG measurements one can identify abnormal cortical activity in patients with Parkinson's disease (27), autism spectrum disorder (28), Alzheimer's disease (29), and post-traumatic stress disorder (30). In addition to cortical measurements, SQUIDs have been used to study the spinal cord biomagnetic fields in response to peripheral stimuli (31). Spinal cord biomagnetic fields are measured by an integrated SQUID system, minimizing the skin-to-sensor distance ($\sim 12\,\mathrm{mm}$) and improving the signal-to-noise ratio (31). This non-invasive method is known as magnetospinography (MSG) and could be an alternative spinal cord imaging method to the widely used surface electrodes (32) or catheter epidural electrodes systems (33). A recent MSG system consists of a 120 SQUID array, which can measure neuronal activation on selected spinal regions, such as the cervical spine (34) and lumbar spine (35; 36). MSG has been shown to detect pathological spinal cord signals in spondylotic myelopathy patient (37), leading the way to a range of clinical applications.

SQUIDs are extremely sensitive, low-noise magnetometers able to measure low and high-frequency signals. For decades, alternative magnetometers could not reach the sensitivity levels of the SQUIDs. Recent advances in magnetometry, however, have led to the development of extremely sensitive spin-exchange relaxation-free (SERF) optically-pumped magnetometers (OPMs) (38) that are near-to-ideal for neuromagnetic measurements.

The fundamentals for the development of the OPM were first studied in the early 1960s, when Bell and Bloom showed that through optical pumping one could detect extremely weak magnetic fields (39; 40). Despite the OPM's sensitivity levels ranging in the orders of $\sim \mathrm{fT/Hz^{1/2}}$ by the early 1970s (41; 42), the first biomagnetic signal was measured nearly 30 years later. By the turn of the millennium, OPM sensors had reduced in size and reached similar sensitivity levels to SQUIDs ($\sim 5\,\mathrm{fT/Hz^{1/2}}$) using the gains of near-zero magnetic field environments combined with high-density alkali vapour cells (spin-exchange relaxation free regime- SERF regime)

(43). A few years later, Kominis et al, developed an OPM with sub-femtotesla sensitivity ($0.54\,\mathrm{fT/Hz^{1/2}}$) (44) which provided the basis for the OPM development used in biomagnetic imaging.

The advances in OPM technology led to the first cardiomagnetic measurement in 2003 (45) and the first cortical measurement in 2006 (46). Compatible, small-sized OPM sensors could measure cortical biomagnetic fields to showcase the improved spatiotemporal resolution and signal-to-noise ratio which led to the development of the OPM-MEG system (47). The capabilities of the new system were demonstrated through a series of studies focused on the primary motor cortex (48), the somatosensory cortex (49) and the visual cortex (50). A recent study validated the suitability of the system in epileptic patients (51), as previously shown in animal models (52). As OPM technology emerged, different types of OPM sensors were developed, providing additional advantages that could integrate the individual OPM sensors into a multi-channel OPM system array, with increased bandwidth and further reduced noise (53; 54).

Despite the great potential of the OPM sensors, this technology is still in its infancy, leaving space for further characterisation of their capabilities and hardware optimisation. This thesis highlights considerations on the use of OPM arrays for neuroimaging, presenting a range of bio-magnetic measurements and experiments. Through the use of three key experiments, examples of improved capabilities of OPM systems were highlighted and compared to previously used methods. Apart from the advantages, significant limitations of the current technology and the effects on the experiments are explained while alternative solutions are proposed and tested. The thesis consists of six chapters. The current chapter, chapter 1, is an overview and history of neuroimaging with a focus on neuromagnetic imaging. Chapter 2 describes the biomagnetic signals, the requirements for a detectable signal, the theoretical understanding of OPMs and SQUIDs, and a detailed discussion on the differences in neuroimaging research. The 3rd chapter documents the study of visually evoked fields measured with OPM-MEG and SQUID-MEG. The measurement were obtained in the MSR at Physikalisch- Technische Bundesanstalt (PTB), Berlin. The results demonstrated the improved spatio-temporal resolution of the OPM-MEG system compared to the SQUID-MEG system. The activation patterns

of neighbouring cortical regions were better defined and easier distinguished in the OPM measurements when compared to SQUID recordings. Although the study had a small sample size, the results were highly reproducible. Future research is required to further validate the spatio-temporal resolution of the OPM-MEG system.

Although advantages of the OPM sensors in neurological measurements have been shown (48; 51), the full potential of the OPM is limited by the design and characteristics. In chapter 4, we introduce a newly built modular OPM sensor for neuroimaging. The sensors were found more suitable for neuroimaging based on an alpha rhythm experiment conducted in two participants. These measurements were obtained in a magnetically shielded cylinder at the University of Sussex. The future applications and advantages over the currently available OPM sensors are described.

In Chapter 5, we show the potential for a novel spinal cord imaging system using commercially available OPMs and the modular OPM. A phantom (simulation) study indicates the high bandwidth and the lack of a built-in filters in the modular OPM, providing accurate recordings of high-frequency signals compared to a commercial OPM. Although the performance of the sensors was comparable, the simulation results showed the suitability of both sensors in spinal cord imaging. Following these results, an in-vivo spinal cord experiment showed the performance, limitations, and possible novel characteristics of spinal cord evoked fields measured by the commercially available sensors. The simulated data were obtained in a small magnetically shielded cylinder at the University of Sussex. The in-vivo experiment, was measured in the MSR at Cardiff University Research Imaging Centre (CUBRIC).

Chapter 6 summarises the experimental findings and discusses the OPM technology, the advantages over other sensors and also limitations. Potential topics for future research are discussed, including a variety of stimuli, sensor configurations, and comparisons between sensors to further characterise the OPM neuroimaging system and the novel neurophysiological findings described in the previous chapters.

Chapter 2

Bio-magnetic Imaging

Optically pumped magnetometers measure weak biomagnetic signals, which arise from synchronous neuronal signaling. This chapter briefly discusses the theoretical basis of the neuronal signaling in cortical and spinal cord measurements. As these biomagnetic signals are extremely weak, noise reduction and data analysis methods are required to isolate the neurophysiological response. These requirements apply to both SQUID and OPM systems, which are described in the last section of this chapter.

2.1 Biomagnetic Signals

2.1.1 Neuronal Signaling

The central nervous system (CNS) consists of the brain and spinal cord (55). Neurons within the CNS process and store information from environmental inputs. Neuronal communication is based on electrical activity, where the information is transmitted through electrochemical signals (10; 56). Neuroimaging methods, such as EEG or MEG, measure the electric current or magnetic field, respectively, induced by the neuronal activity (21; 56).

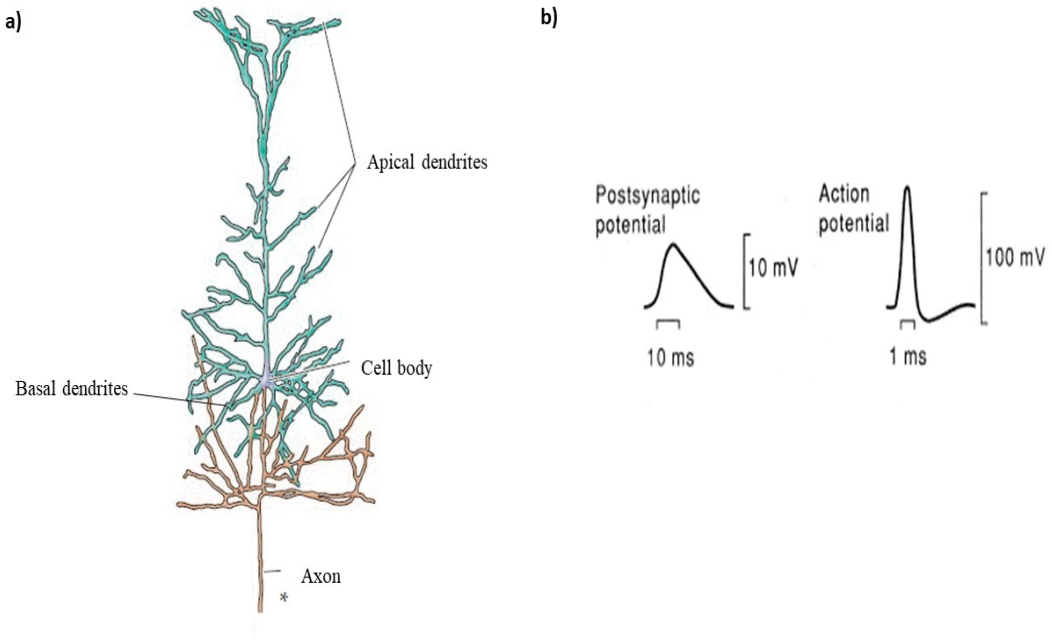

Figure 2.1: Neuronal structure and signaling of the human brain. (a) Diagram of a typical pyramidal neuron. From the cell body (soma) extend the apical dendrites, the basal dendrites (receive information), the axon (responsible for the propagation of information). Figure adapted from (57). (b) Differences in duration and amplitude of the postsynaptic potential (PSP) and the action potential (AP). PSPs have longer duration ($\sim$ 10 ms) and have an amplitude of 10 mV. APs are fast activations (1 ms) with 10 times larger amplitude than the PSPs. Figure adapted from (58).

Neurons are the basic building blocks of communication within the nervous system and are characterised by four basic structures; the soma (cell body), the axon, the dendrites and the presynaptic conjunctions 2.1 (57).The soma contains the nucleus, the neuronal metabolic centre. The dendrites or dendtiatic arborization extend from the soma and aid the neuronal communication by receiving electrical signals from surrounding neurons. The axon extends away from the soma, conveying the signal to other neurons and can be up to 3 m in length (21). Long axons are wrapped in a myelin sheath, which when combined with nodes of Ranvier (gaps found in myelinated neuronal axons), help to maintain the electric signal propagation. Telodendria are formed at the end of the axon, with the axon terminal connecting to the dendrites of another neuron (see figure 2.1 *b*).

A synapse is the connection point of the two neurons, where information is transferred (55; 57; 59). The neuron that transmits the information is called a presynaptic neuron and the one receiving the information is called a postsynaptic neuron. The synapse is formed by a gap, known as the synaptic cleft, where the signal propagates from the presynaptic terminal to the postsynaptic dendrite or soma (60). The human brain includes different types of synapses which are categorized as electrical or chemical synapses. Although there are many fewer electrical synapses than chemical ones, the former are still observed throughout the CNS. In an electrical synapse, ionic current passes through the synaptic cleft from the presynaptic to the postsynaptic neuron. In the chemical synapse, there is a secretion of neurotransmitters in the synaptic cleft which activates the postsynaptic neuron's molecule receptors and induces the propagating current flow (57; 59).

In the resting state, the neuronal membrane potential is $-70\,\mathrm{mV}$, which denotes the negative intracellular potential with respect to the extracellular environment. The interior of the cell has a high concentration of potassium cations (K^+) while the positive extracellular environment has an excess of both sodium cations (Na^+) and chloride anions (Cl^-)(61). Neurons generate time varying electrical currents, which can transmit information by depolarizing or hyperpolarizing a resting membrane. The action potential (AP) is a regenerative signal that rapidly and transiently reverses the membrane equilibrium after $\sim$1 ms. The short and rapid electric impulse propagates along the axon, with a constant $\sim$100 mV amplitude. The nodes of Ranvier regenerate the signal and maintain its intensity along the length of transmission. Slower postsynaptic potentials (PSP) occur through chemical synapses. These PSPs depend highly on the released neurotransmitters and receptors and can be either excitatory (EPSP) or inhibitory (IPSP) potentials. In EPSP, the neuron releases neurotransmitters or ions that are captured by the postsynaptic dendrites and represent the original action potential. Depending on the selected neurotransmitters and receptors, the duration of the EPSP ranges from 2 ms - 100 ms (61; 58).

2.1.2 Neuronal electromagnetism

Maxwell's equations describe the relationship between electric and magnetic fields. In neuroimaging, the use of Maxwell's equations allow the modeling of the magnetic

fields induced by specific neuronal currents (58; 62). A current density (J) induces a given electric current (E) and magnetic field (B). As electrophysiological signals typically have frequencies below 1 kHz, we use the quasi-static approximation of Maxwell's equations (58; 63; 56). As the cortical tissue, scalp and skull don't effect the magnetic field, the permeability of those tissues is equal to the permeability of the free space ($\mu_0 = 4\pi \times 10^{-7}$ H m^{-1}).

The Biot-Sarvat law describes the relation between the quasi-static current density J (r') at the location r' and the induced magnetic field $B(r)$ at location r as:

$$B(r) = \frac{\mu_0}{4\pi} \int J(r') \times \frac{r - r'}{(r - r')^3} d^3r' \tag{2.1}$$

where μ_0 is the permeability of free space, and d^3r' is the differential volume element. The cortical current density $J(r')$ consists of two components: the primary current density J_p induced by current flow of the axons, dendrites and tissue, and the volume current density J_v, induced by the extracellular electric field. Hence the total neuronal current density can be described as the sum of the primary current density and the volume current density.

$$J(r') = J_p(r') + J_v(r') = J_p(r') + \sigma(r')E(r') = J_p(r') - \sigma(r')\nabla V(r') \tag{2.2}$$

with $\sigma(r')$ the isotopic conductivity at the location r', E the electric field which is equivalent to the negative electric potential gradient and represent the charge carries of the medium. The magnetic field (B_0) for the primary current density is:

$$B_0(r) = \frac{\mu_0}{4\pi} \int J_p(r') \frac{r - r'}{(r - r')^3} d^3r' \tag{2.3}$$

with J_p(r') the primary current density at the location r'. Similarly, the magnetic field for the volume current density (B_v) across the surface intervals (brain-skull-scalp-air boundaries) is:

$$B_v(r) = \frac{\mu_0}{4\pi} \sum_{ij} (\sigma_i - \sigma_j) \int V(r') \frac{r - r'}{(r - r')^3} dS_{ij} \tag{2.4}$$

where $\sigma_i - \sigma_j$ is the conductivity difference between surface intervals, such as brain-skull, V(r') is the potential at the location r' to the volume current distribution and S_{ij} are the selected surface regions ranging from surface i to j.

Hence, the magnetic field B(r) at the location r induced in response to the primary current density J_p and the volume current density J_v can be measured from equations 2.3, 2.4.

$$B(r) = B_0(r) + B_v(r) \tag{2.5}$$

Quantum sensors can measure biomagnetic fields produced in response to a stimulus. The estimation of this magnetic field as a result of the current source is known as the forward problem and can be calculated for cortical (10; 64) and spinal cord recordings (31).

2.1.3 Cortical measurements

Quantum sensors measure the magnetic fields associated with the current produced by the action potential and postsynaptic potential in response to an environmental stimulus. The primary source of measurable magnetic signal is due to cortical activations along the cerebral cortex, the outermost cortical layer (65). A multilayered neuronal arrangement consists of grey matter, a thick layer (2-3 mm), creating the distinguishable cortical folding, called gyri and sulci of the brain. Layer I is close to pia matter (outermost cortical layer) and layer VI is above the white matter (55). The neurons are organized into small columns (80-100 neurons/column) with a 50 µm cross-section. Almost 75% of the cortical neuronal population are pyramidal cells. These cells are multipolar neurons (one axon, numerous dendrite and dendrite branches), which extend the apical dendrites toward the cortical surface. The orientation and parallel alignment of pyramidal neurons is considered to be the origin of the detectable biomagnetic signal (56; 66).

Neuronal activity generates a current flow along the neuronal axon or telodendria resulting in a magnetic field perpendicular to the current flow. In the cerebral cortex, a brain response is detectable when a coherent magnetic field is generated along the neuronal axons or apical dendrites. Due to the cortical folding, the detectable magnetic fields occur from current components tangential to the cortical surface (see figure 2.3). Any electric components oriented radially to the skull can not be measured (10; 56).

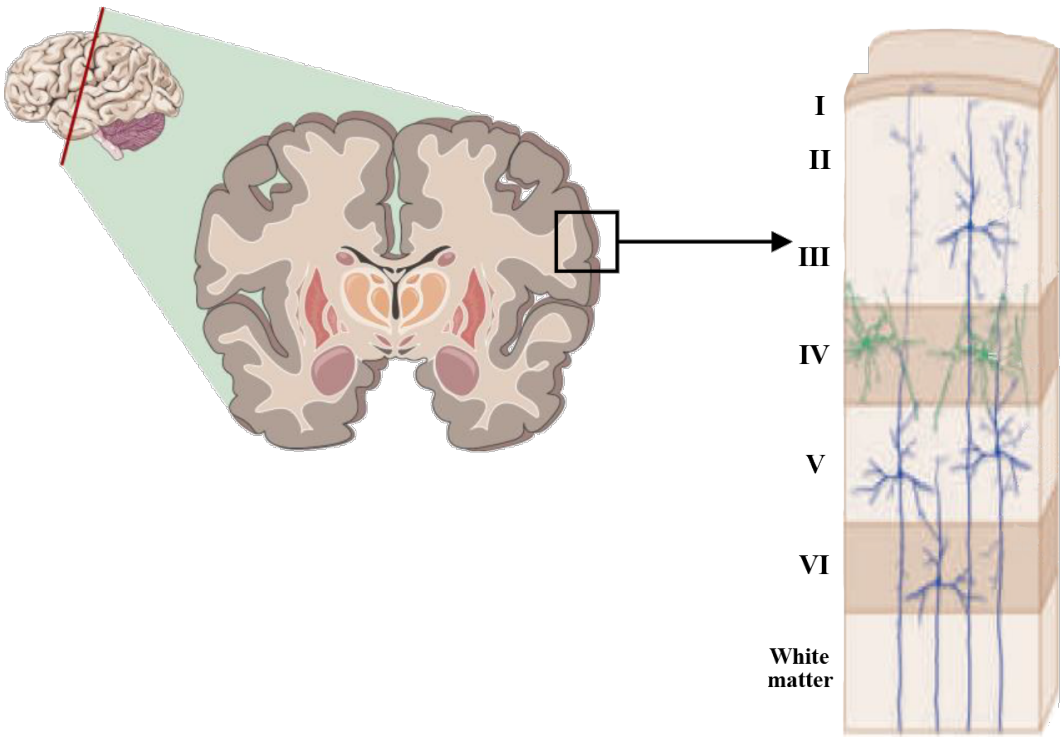

Figure 2.2: The cross section of the human brain illustrates the multilayered neuronal arrangement of the grey matter. The layer I is close to the outermost cortical layer (pia matter) and the VI layer is above the white matter. The cytoarchitecture of the cortical layers shows the pyramidal soma in V layer and dentrite branches reaching the cortical surface (adapted from (57)).

A biomagnetic field measured by a quantum sensor can be the product of simultaneous neuron activations, otherwise known as sychronous AP and PSP. Action potentials are more difficult to measure, as the propagation of the signal can be bidirectional, with measured magnetic field reduced by counter propagating currents and volume currents. Thus, the action potential current flow is estimated by two current dipoles, opposite to each other. Based on (58) the separation between the dipoles is estimated as 1 mm for a conduction velocity (v) of v= 1 m/s and magnitude of 100 fA m. The resulting circulated magnetic field is a quadruple, which decays faster as the distance, r, increases from the source (here neuron), described as $1/r^3$. In contrary, a PSP is usually illustrated as a current dipole, where the current intensity decreases slower with distance from the source ($1/r^2$). The longer duration of the PSP allows larger current flow summation of the neighboring neurons, than

the short and rapid AP. Hence, the majority of the recorded signal arises from the PSPs.

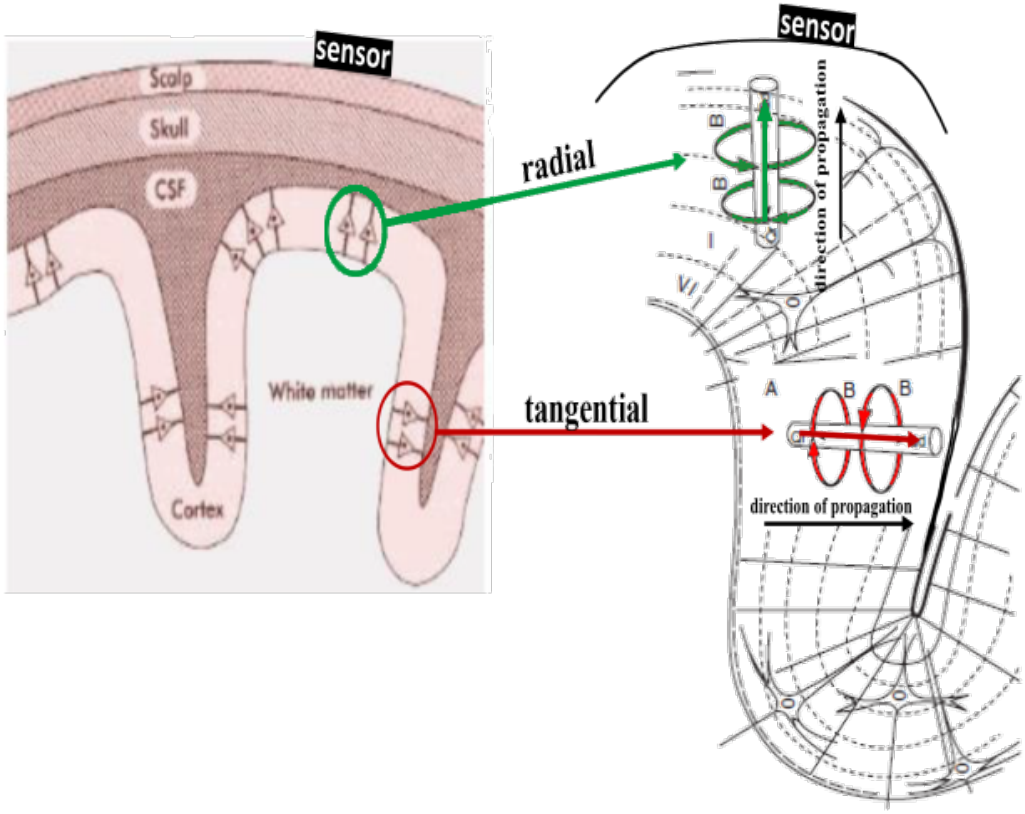

Figure 2.3: Detectable cortical biomagnetic signals. Illustration of the scalp, skull, cerebrospinal fluid (CSF) and the cortex. Current dipoles show the alignment of the pyramidal neurons with respect to the cortex and the sensor (black box). The radial neurons (green circle) produce a magnetic field tangential to the cortex, thus the sensor cannot detect the biomagnetic signal. Contrary, the tangential pyramidal cells (red circle) produce detectable biomagnetic signals. The green and red circular arrows indicate the magnetic flux of the radial and tangential pyramidal cells. The black arrows the direction of the propagating signal. Figures adapted from (56).

Cortical measurements demand a large population of neurons to "fire" together to produce a detectable signal (55; 57). If a 2 mm pyramidal neuron in the neocortex is modeled as a current dipole of 0.2 pA m, the intensity of minimum detectable signal was calculated as 10 nA m. It is estimated that approximately 50,000 neurons need to be synchronised and fire together to produce a 10 pA m signal. If the cortical column is ∼40 µm, the 50,000 neurons will cover a cortical patch of 0.63 mm^2 or a

circular cortical patch with a diameter of 0.9 mm (56; 58).

2.1.4 Spinal Cord Measurements

The communication within the CNS is also based on neuronal signaling, it transmits the sensory information of the surrounding tissue to the spinal cord and brain. Similar to the brain, the spinal cord consist of neurons, grey matter and white matter (67). The cross section of the spinal cord shows a butterfly shaped grey matter at the central core, surrounded by white matter (see figure 2.4). The grey matter is divided into three regions, the dorsal, the intermediate and ventral horns. The dorsal horn consists of sensory nuclei or neurons with axons externally extended to receive peripheral stimuli, while the ventral horn includes motor nuclei or neurons with axons reaching the skeletal muscles (55; 67). Long columns of neurons extend along the spinal cord, while the sensory neurons are arranged in distinct clusters. The cytoarchitecture of the spinal grey matter can be separated into a 10 layer structure that is based on the nuclei type. Layers I to VI corresponds to the dorsal horn region, layer VII to the intermediate region, layers VII to IX comprise the ventral horn and layer X is grey matter wrapped around the central canal (56).

Similarly, spinal white matter consists of dorsal, lateral and ventral columns, with both ascending and descending axons to the brain stem (67; 55).

The spinal cord consist of four distinct regions known as the cervical spine (CS), the thoracic spine(TS), the lumbar spine (LS) and the sacral spine (SLS). These regions are categorised into 30 segments by the dorsal and ventral roots connections (8 CS, 12 TS, 5 LS, 5 SLS). The dorsal root ganglia convey somatosensory information obtained from muscles, joints or limbs into the spinal cord (see figure 2.4).

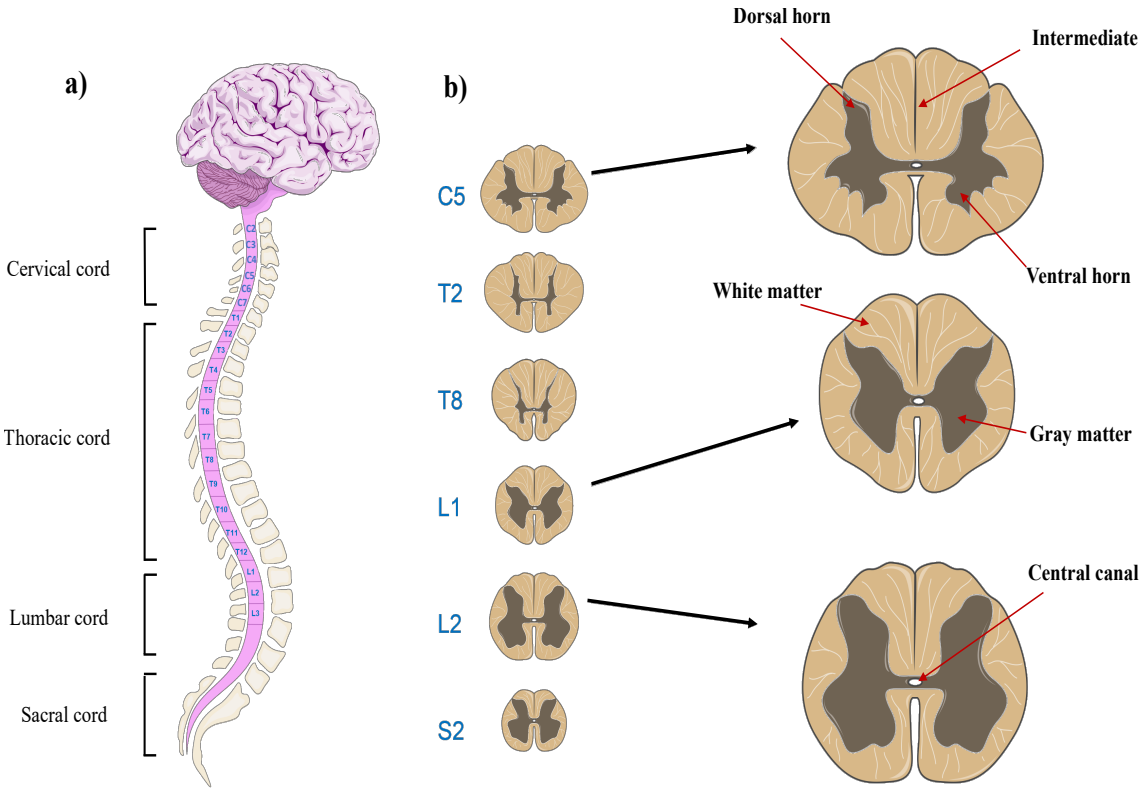

Figure 2.4: Spinal cord anatomy. (a) The central nervous system. The spinal cord consists of four regions, the cervical spine, the thoracic spine, the lumbar spine and the sacral spine. (b) Cross section of the spinal cord from the cervical spine (C5), Thoracic spine (T2,T8), lumbar spine (L1,L2) and sacral spine (S2). The red arrows show the anatomical characteristics of the spinal cord. Both figures adapted from (https://smart.servier.com/)

The connection between the brain and the cortex relies on specialised tracts, extending from spinal white matter to the brain stem. One of these tracts is the spinothalamic track (STT) (68). As its name indicates, STT is a sensory pathway that conveys nociceptic stimuli into the thalamus and somatosensory area. From there, the sensory signal propagates through the spinoreticulothalamic (SRT) and spinotectal (ST) tract to reach the targeted somatosensory cortical area. The system is known as the anterolateral system. STT consists of two adjacent axons, the anterior axon and the lateral axon. Due to the parallel extension of the axons, they are considered as one pathway. Each STT axon passes different types of sensory inputs; the anterior STT carries light touch inputs and the lateral STT carries

nociceptic inputs i.e. pain or thermal information. The STT consist of three different types of somatosensory fibers; type III fibers, unmyelinated C fibers and myelinated α-δ fibers (68; 55).

In our study, we used peripheral electric stimulation to excite and measure the spinal cord evoked field. The peripheral sensory neurons were projected into the dorsal spinal horn. Then the sensory neurons synapsed with the fast-conducting α-δ fibers and C fibers. The signal propagated through the STT, SRT and ST to the somatosensory cortex. The current flow along the neuronal axon or dendrites generated the detectable magnetic field over the CS, LS and the somatosensory cortical region.

2.2 Noise reduction methods

Neuronal activation measurements depend on the simultaneous activation and alignment of neurons at the recording site along with the environmental stimulus. The intensity of the biomagnetic fields are extremely low (on the order of fT) (10) and differ according to the recording location (69). As such these measured fields are dominated by the Earth's magnetic field and urban noise (see figure 2.5). Thus, the study of neuronal activity is challenging and requires sensors with low noise floors combined with environmental noise suppression. In order to gain sufficient suppression of this noise, we need specifically designed equipment and computational methods. During cortical and spinal cord recordings, the measurements have an inherent variability caused by other signals present due to background noise. To distinguish the evoked response we average over distinctive repeated stimulations and thus reduce the background noise yielding the "clean" neuronal response. Ferromagnetic materials are used to construct magnetically shielded environments (MSE) of different sizes, where the environmental magnetic noise is extremely low (on the order of nT). The biomagnetic measurements are usually obtained in magnetically shielded rooms (MSR) (70) or magnetically shielded constructions large enough to fit a human participant (71). The magnetically shielded environments consist of layers of μ-metal and aluminium. The aluminium plates are placed in between the μ-metal layers, and usually are equipped with active compensation

coils. The shielding factor depends on the number of layers of shielding and the dimensions of the MSE. An equally important consideration is the location of the MSE : mechanical vibrations, such as train lines or passing cars, could interfere with the recordings and produce significant artifacts in the data (56).

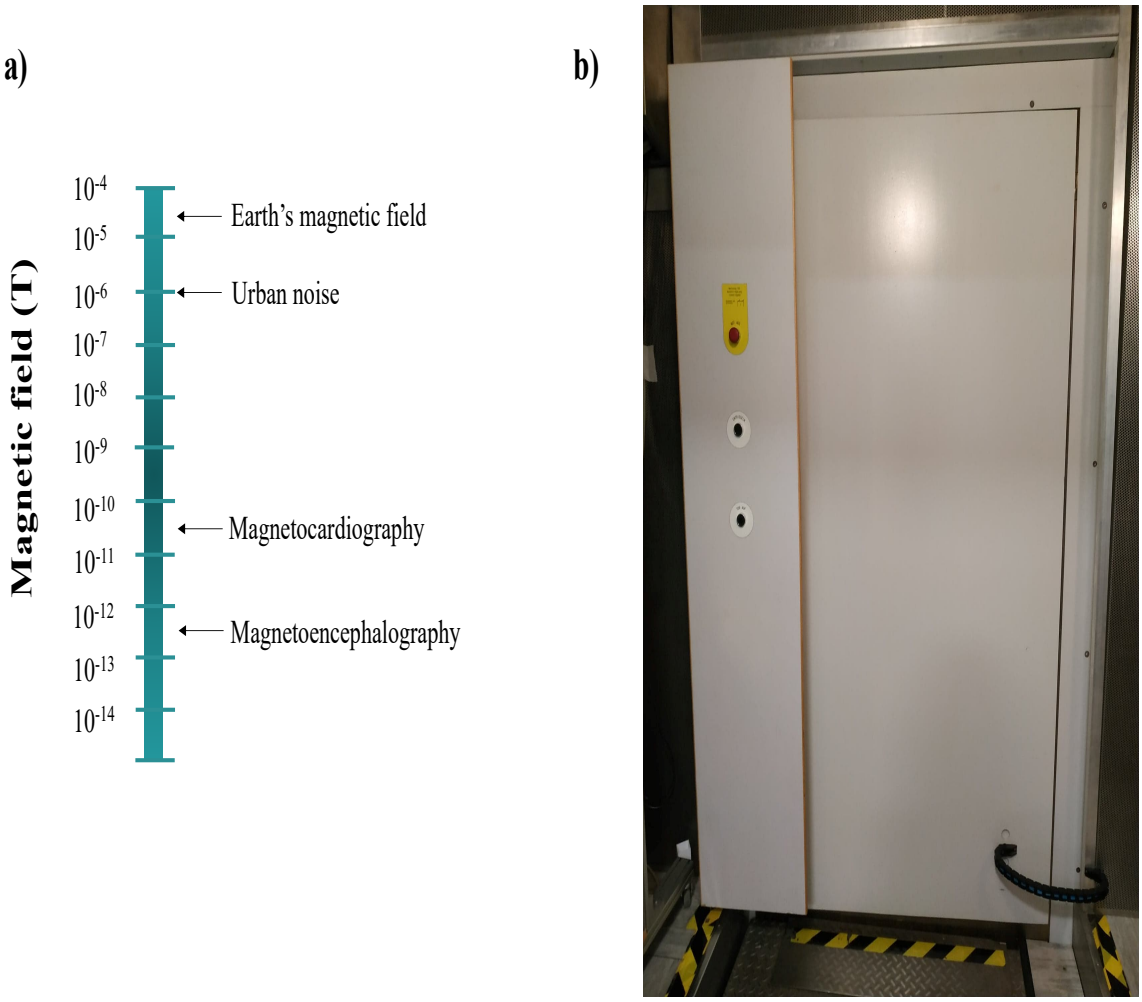

Figure 2.5: Scale of the environmental magnetic noise & Magnetically Shielded Room (MSR). (a) Amplitude variations of the magnetic environmental noise compared to biomagnetic signals (72) (b) MSR reduces the environmental noise in orders of nanoTesla (10^{-9} T). The MSR is the Ak3b MSR–Vacuumschmelze, Hanau, Germany, at Physikalisch- Technische Bundesanstalt (PTB), Berlin

Despite the magnetic noise isolation, some residual noise is still present within the MSE which degrades the measurement. The ambient noise, or background noise, arises from various sources, such as power lines or traffic. In order to accurately measure and separate this type of noise from the biological signal one can use ref-

erence sensors or sensors in a gradiometer configuration (56). Reference sensors are usually placed $\sim$ 10 cm next to the measurement sensors and record the magnetic noise fluctuations without recording the actual neuronal response. The reference sensor operates better when the background noise is both spatially and temporally homogeneous.

The gradiometer sensor configuration significantly aids noise suppression in measurements, as it invariant to any inhomogeneous background noise. In the axial gradiometer configuration, two magnetometers are placed in series radially to the surface, separated by few centimeters. The magnetometer nearer the source measures a stronger magnetic field from the neuronal activation coupled with background noise interference, whereas the magnetometer further from the source records a weaker magnetic field from the same source activation coupled to the same background noise interference. Therefore the difference between the two magnetometers determines the spatial gradient of the magnetic field.

Apart from the ambient noise artifacts, biomagnetic measurements are also affected by spontaneous physiological responses, such as sudden movements, blinking or swallowing (73; 74). This sudden motion causes artifacts in the measurements due to the inhomogeneity of the background field, which causes the sensors to measure different fields when translated spatially. Although in most experiments the participants are asked to maintain their position and limit their movement, muscle contractions or movement in response are impossible to completely avoid. Data analysis algorithms help to identify and remove the majority of these artifacts (74).

2.3 SQUID

The superconducting quantum interference devices or SQUID sensors are used as part of integrated systems to measure weak biomagnetic fields. Due to the high sensitivity and low-noise level of this sensor (64), SQUIDs are widely use for cortical measurements. A SQUID sensor consists of a superconductive loop (usually made from niobium nitride-NbN) with one or more Josephson junctions (JJ) in parallel (64; 75). Radio frequency SQUIDs (rf SQUID) have one JJ, while direct current SQUIDs (dcSQUIDs) have at least two JJs. Due to the close proximity of the

superconductive loop and the JJ, a current flows constantly between the two JJs without applying any voltage. This effect is known as the Josephson effect (76). The SQUID's sensitivity depends on the pick-up coil which acts as a magnetic flux-voltage converter and is coupled to the SQUID. The flux-voltage converter can be either a magnetometer, a planar gradiometer (two pick up coils placed next to each other, providing maximum spatial sensitivity) or an axial gradiometer (two pick up coils placed in series, providing high sensitivity to radial sources) (77). Hence, in a dcSQUID-MEG system that uses the axial gradiometer configuration as flux-voltage converter, any biomagnetic signals perpendicular to the pick-up coil are detectable. The measured magnetic flux generates a periodic voltage across the JJs. This new voltage is characterised by amplitude changes correlated to the measured biomagnetic signal, producing the final MEG signal (75).

However, this type of superconductor can only operate in cryogenic environments with temperatures close to absolute zero. In order to achieve such low temperatures, the SQUID sensors are placed in a liquid helium bath (64; 78). Recent MEG systems consist of 100 to 300 sensors, with SQUID magnetometers and axial or planar gradiometers distributed along the scalp. Similarly, a recent MSG SQUID system used a 120-channel biomagnetometer system (79), covering the area of interest across the spinal cord.

Over the past 50 years, SQUID systems have become widely used to study healthy and clinical populations. However, their performance is still limited by the need for cryogenic cooling.

In a SQUID-MEG system, the sensors are fixed in a rigid helmet inside the helium dewar (see figure 2.6) with the SQUID locations arranged to fit an average adult head, however they don't fully accommodate for a variety of head sizes and shapes (80). The sensor-to-scalp offset differs accordingly, and can lead to substandard spatial coverage. The typical sensor-to-head distance is ∼30 mm-50 mm. Hence, the SQUIDs have a significant distance from the cortical source, which leads to reduced signal strength (see chapter 2.1.2). Coupled with small movements of the participant during the experimental run, the fixed position of the sensors and the offset distance can have a major impact on the data quality or even in the detection of the cortical activations (81).

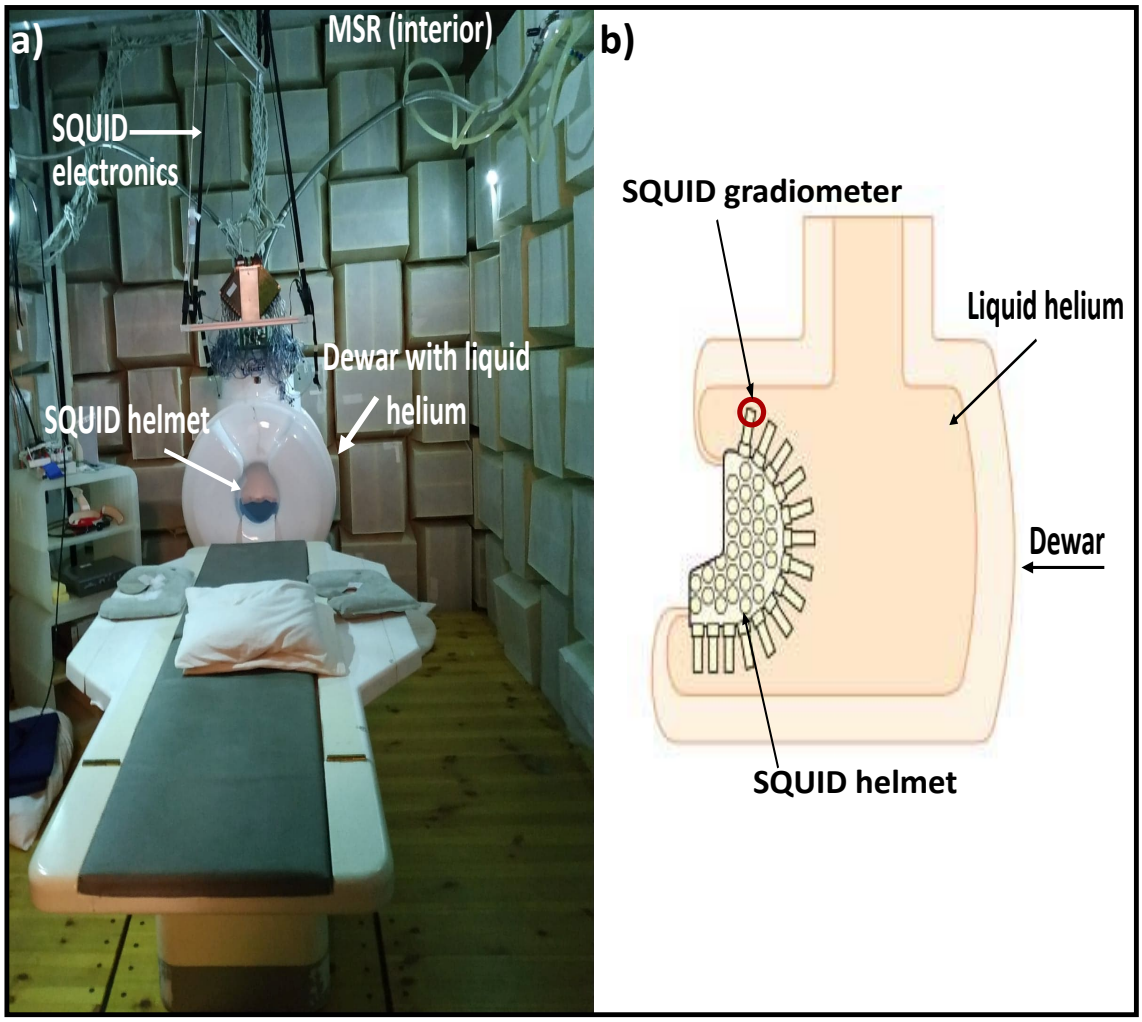

Figure 2.6: Configuration of SQUID-MEG system. (a) SQUID-MEG system, with white arrows pointing to the main components (MEG Vision in Ak3b MSR at Physikalisch-Technische Bundesanstalt (PTB), Berlin). (b) Diagram of the MEG Vision dewar, with black arrows showing the SQUID helmet configuration, the SQUID gradiometers and the liquid helium bath. Diagram adopted from (82).

A similar argument can be made for the SQUID-MSG system. Although the MSG system has reduced significantly the offset of the sensors-to-skin distance (up to ∼7 mm) (31), the rigid positioning of the SQUIDs prevents the sensors from being placed independently in multiple spinal cord regions. Spinal cord activations are usually measured in response to peripheral nerve stimulation, which induces constant movements correlated to the stimulation. These movements interfere with the biomagnetic signals, potentially reducing the data quality.

2.4 OPM

Advances in the field of medical physics provide novel tools and improved sensors to further aid the understanding of the human physiology. Since 1972 (4), SQUIDs monopolised the suitability for biomagnetic measurements. However, recent technological developments have led to extremely sensitive, optically-pumped magnetometers (OPMs) (43; 44). The small sized sensors coupled with improved spatiotemporal resolution and lack of cryogenic cooling give OPM's significant advantages in biomagnetic measurements.

As the name indicates, OPMs rely on the optical pumping of alkali atoms to detect magnetic field changes by monitoring atomic spin precession. Spin Exchange Relaxation Free (SERF) OPMs require high density vapours in close to zero field environments (83).

A typical OPM design includes a laser source (used in optical pumping), a high density vapour cell (includes the buffer gas and a sensing atoms) and a photodiode which measures the changes of the transmitted light (see figure 2.4). Most OPMs use alkali atoms in the vapour cells due to their simple orbital structure. All the alkali atoms, such as rubidium (Rb), caesium (CS) and potassium (K), are characterised by their single valance electron. The laser light only interacts with the valance electron, and depending on the beam frequency, could result in energy changes of the atom i.e. changes of the angular momentum (84).

In the presence of an external magnetic field $\vec{B}$, the atomic magnetic moment ($\vec{\mu}$) tries to align with the direction of the external magnetic field. However, the angular momentum of the atom causes the magnetic moment to be misaligned from the external magnetic field. This causes a torque (72) proportional to:

$$\vec{\tau} = \vec{\mu} \times \vec{B} = \gamma \vec{J} \times \vec{B} \tag{2.6}$$

where $\vec{\tau}$ is the torque, $\vec{B}$ is the applied magnetic field. The magnetic moment $\vec{\mu}$ is proportional to the gyromagnetic ratio of the atom γ and to the total angular momentum of the atom $\vec{J}$.

The rate at which the atom precesses, known as the Larmor frequency (72), is proportional to :

$$\omega = -\gamma \vec{B} \tag{2.7}$$

where ω is the Larmor frequency, γ is the gyromagnetic ratio of the atom and $\vec{B}$ is the magnetic field. An electron's angular momentum is the sum of its orbital angular momentum and spin angular momentum, denoted here as orbit and spin respectively (84). As shown by the equations 2.7 and 2.6, changes of the angular momentum result in changes of the magnetic moment and the atomic state (84). By exciting the valence electron into different states, one can select the atomic angular momentum. Based on these characteristics, through optical pumping one can align the spin of the atoms into the direction of the laser beam.

Optical pumping uses a resonant circular polarized light to pump the alkali atoms into the same initial atomic state (85; 84). The wavelength of the laser along with the polarization of the light can selectively determine the energy level of the pumped atoms. Depending on the atoms in the vapour cell, the wavelength varies. Once the atoms are pumped into the same state, the atoms are in the "dark state" (can not observe or emit any photons), thus the laser beam does not transfer the angular momentum and the atoms in the vapour cell become transparent to the light.

The polarized vapour cell is highly sensitive to magnetic field fluctuations perpendicular to the laser beam. An applied magnetic field perpendicular to the laser beam is scanned across the atoms of the vapour cell, where the photodiode (PD) measures the changes of the polarized atoms in response to applied field, with least change – hence maximum transparency – in close-to-zero magnetic fields. The PD output is a Lorenzian line and is known as zero-field resonance (47; 41). To achieve similar sensitivity levels to a wider area around the zero field, modulation coils apply oscillating magnetic fields which modulates the resonance, while it simultaneously demodulates the resonance.

Relaxation effects, such as spin exchange collisions, spin destruction collision or collision at the cell's wall, tend to depolarize the system and, thus, reduce the sensitivity to external magnetic fields (86). The spin exchange relaxation free (SERF) regime reflects the suppression of the relaxation due to spin exchange collisions and thus exchange of energy states. In near to zero-magnetic field, high density alkali atoms rapidly collide and exchange spin faster than their precession frequency. The

rate of the spin collisions in SERF regime depends on the close-to-zero background magnetic field and the atomic density in the vapour cell (83).

In this thesis, all the biomagnetic signals were measured by zero-field rubidium ^{87}Rb OPMs. In order to achieve increased spin collisions, thus improved SERF regime function, the measurements are obtained within MSE, with noise levels on the order of nT. The rubidium vapour cell is heated to $\sim$ 150 °C (87) to achieve the optimal vapour density (47). Besides ^{87}Rb atoms, the vapour cell contains a mixture of buffer gas, which significantly reduces the collisions at the cell's wall. For the optical pumping, a 795 nm laser polarizes the atoms into the beams direction until the atoms are in the highly transparent state, where the incoming light passes through and is measured by the photodiode. An applied magnetic field perpendicular to the laser beam direction, creates spin precession and allows atoms to evolve and absorb circularly polarised light. The PD measures the transverse magnetic field the transmitted light as a voltage and reflects the measured magnetic flux. OPMs can measure the radial, axial and tangential magnetic field components. The modulation coils have selected frequencies above the ^{87}Rb relaxation rates i.e. for the commercially available OPMs is 923 Hz, and determine the sensitive axis of the magnetometer.

Studies have shown that the improved performance of OPMs in biomagnetic measurements surpasses the limitations of SQUID imaging systems. Without the need of cryogenic cooling, OPMs can to be placed independently and directly on the targeted region – similar to the EEG electrodes – reducing the skin-to-surface distance to $\sim$ 3 -5 mm. Hence, in an OPM neuroimaging system the sensor positioning can be tailored to each participant's needs i.e. different head size and shape. With an offset $\sim$ 10 times smaller than the SQUIDs', coupled with their ability to simultaneously measure two or three magnetic field components, OPMs allow a more detailed characterisation of neurophysiological signals compared to single axis observations. Moreover, with the ability to temporarily fix the sensors on the participant's head or spinal cord, the technology becomes more resilient to involuntary movement (88).

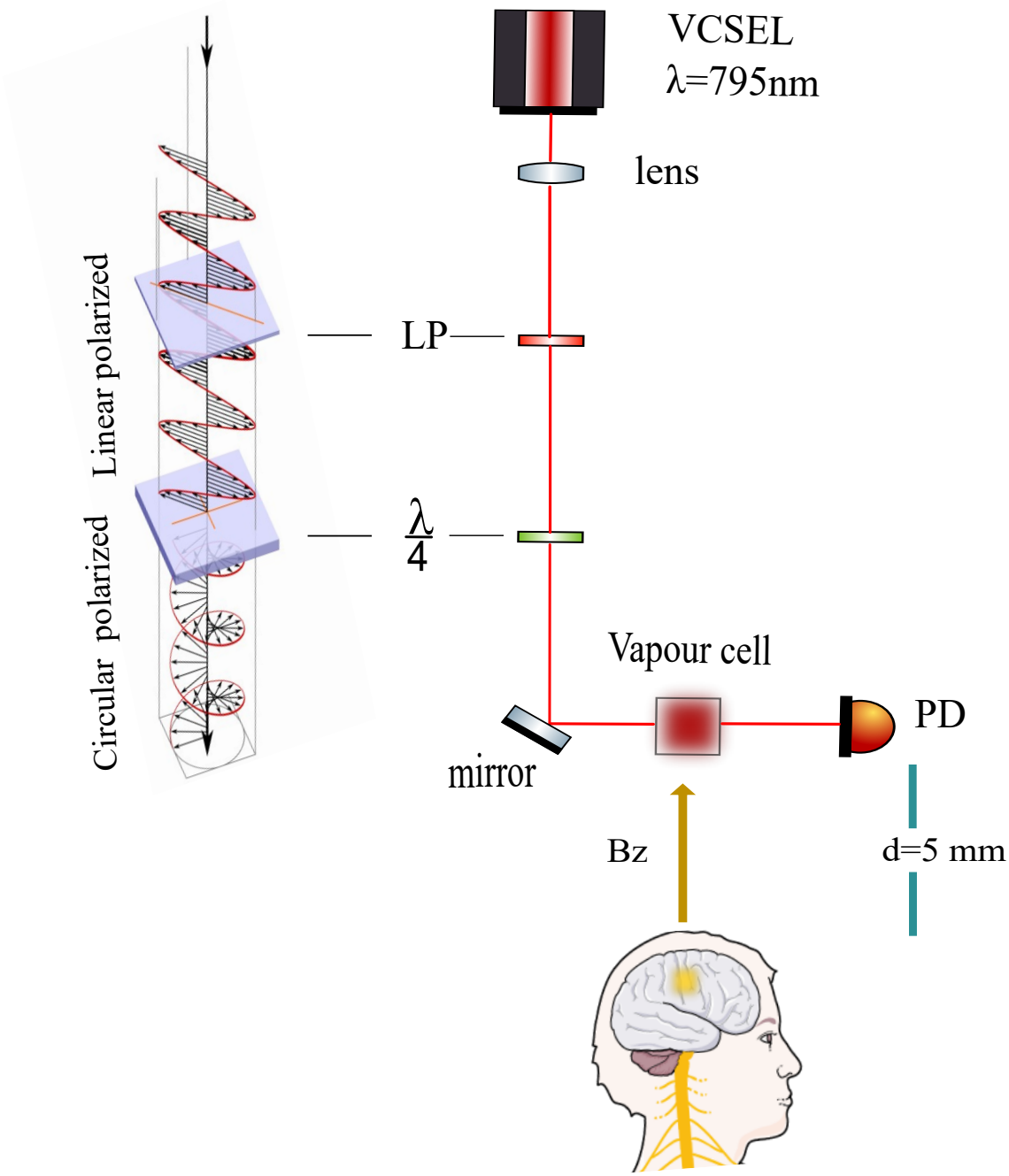

Figure 2.7: A 795 nm single mode surface emitting laser (VCSEL) emits a beam into the lens and through the linear polariser (LP). The polarized beam is driven into the quarter-waveplate ($\lambda/4$) and becomes circularly polarized. The mirror directs the probe light into the vapour cell. Opposite to the cell is the photodiode (PD). On the left, the output the VCSEL is shown in the three different stages: as a raw output of the laser, after the linear polarization and after the circular polarization. A magnetic field perpendicular to the vapour cell (Bz, yellow arrow), such as the radial magnetic field component of a brain activation, can be measured by the OPM sensor. The scalp-to-sensor distance is $\sim$5 mm.

These improvements enabled applications in clinical research, where involuntary movement could be caused by the condition, and on pediatric research, where the small head size and the movement could have resulted to limited spatial coverage and reduced data quality.

Most OPM biomagnetic research utilize the commercially available zero field QuSpin sensors (QuSpin Inc., Louisville, CO, USA). Although OPM sensors were only recently utilized for biomagnetic imaging and have shown great potential in neurophysiological measurements, OPM based systems have not yet reached their full potential. The individual sensor placement is efficient for studying targeted cortical circuits or spinal cord regions but better understanding of the functional brain or spinal cord requires multiple, closely placed sensors. QuSpin OPMs suffer from cross-talk artifacts and individual wiring interfering when multiple sensors are placed closer than 20 mm (89), reducing possible spatial pitch. The limited bandwidth of the QuSpin sensors (135 Hz) (47) coupled with a 500 Hz bandstop filter might be sufficient for low frequency cortical activations (< 100 Hz), but makes the sensors unsuitable for studying high frequency signals (> 600 Hz), as those previously reported in cortical (90) and spinal cord studies (91; 92). Moreover, the function of the OPM requires heating of the vapour cell to a typical temperature ($\sim 150\,^{\circ}$C) (47), making it unsuitable for direct placement on the skin or scalp. Hence OPM based systems require further standoff distance to provide thermal insulation.

A proposed solution to surpass the limitation of the OPM based systems is the development of an OPM array, with broader bandwidth, using a common light source to further reduce the cross-talk and wiring interference as proposed in Chapter 4. As the high operating temperature of the OPM is required for its operations, the development of a sensor helmet or holding system with cooling mechanisms could ensure thermal insulation.

2.5 Summary

This chapter described the theoretical background of cortical and spinal biomagnetic signals and discussed two methods of measuring them, the SQUIDs and the OPMs. The suitability of each method for measuring these biomagnetic signals was assessed.

Neurons are the basic form of communication in the central nervous system,which is achieved by synaptic growth between neurons. Depending on the type of synapse, a propagating biomagnetic signal is produced, and when a large population of neurons fire simultaneously a measurable biomagnetic signal is created. The study of the pathways between the brain and the spinal cord provide valuable insights in research and clinical applications. The measurement of such signals depends on the sensitivity of the system. SQUID based imaging systems have sufficient sensitivity and low noise floor for functional brain and spinal cord measurements. However, the need of cryogenic cooling leads to increased skin-to-sensor distance and could induce significant limitations in clinical applications. OPM based imaging systems can surpass the limitations of SQUIDs', reducing the offset distance by a factor of 10. The improved skin-to-sensor distance has led to improved signal to noise ratio and spatiotemporal resolution, which have led to novel research applications. However, limitations of the commercial OPM design effects the performance of the system. The limited bandwidth of the sensor along with the cross-talk artifacts result in a neuroimaging system restricted to low frequency signals. Proposed changes to the initial design and structure of the sensor would lead to an improved neuroimaging system, with greater sensitivity and broader bandwidth suitable for measuring low and high frequency signals with improved spatial coverage.

Chapter 3

Improved spatio-temporal resolution of visually evoked fields using optically-pumped magnetometer

(Adapted from paper: Aikaterini Gialopsou, Christopher Abel, T M James, Thomas Coussens, Mark G Bason, Reuben Puddy, Francesco Di Lorenzo, Katharina Rolfs, Jens Voigt, Tilmann Sander, Mara Cercignani, and Peter Krüger. Improved spatio-temporal measurements of visually evoked fields using optically-pumped magnetometers. Scientific Reports, 11:22412, 123.)

Recent studies have shown significant advantages of optically-pumped magnetometer magnetoencephalography (OPM-MEG) over superconducting quantum interference device magnetoencephalography (SQUID-MEG) (88; 93). The lack of cryogenic cooling and the direct placement of the OPM at the scalp are predicted to provide improved signal-to-noise ratio (SnR) and spatial resolution. We hypothesize the smaller stand-off distance of the OPM sensors to the scalp can be further exploited to improve the spatio-temporal resolution of the OPM-MEG system. This chapter describes a series of experiments to test this hypothesis.

Through the highly reproducible participants' responses, we demonstrate the

improved spatio-temporal resolution which were simultaneously measured at the primary and associative visual cortex and highlighted the consistent 10-20 ms time lag between these regions.

The experimental protocol and methodology of the measurements in this chapter were conceived and designed solely by the author. The optically pumped magnetometers and the data acquisition hardware and software were set-up and calibrated by Christopher Abel, Thomas Coussens and the author. The SQUID-MEG system and its DAQ were set-up and calibrated by Katharina Rolfs, Jens Voigt, Tilmann Sanders and the author. The spatio-temporal resolution metric was conceived by Tim M. James. All the data were taken mainly by the author, with assistance of Christopher Abel. All the analysis was performed by the author with assistance by Tim M. James. The results were interpreted by the author with the assistance of Francesco Di Lorenzo, Mara Cercignani and Peter Kruger.

3.1 Introduction

This study demonstrates the improved spatio-temporal resolution of an OPM based MEG system (OPM-MEG) by comparing spatio-temporal characteristics of neurophysiological signals to conventional SQUID-MEG. As a pilot study, the research was focused on the primary visual pathway to assess and highlight the abilities of OPM based biomagnetic systems using commercially available OPMs and two visual stimuli: the Flash Stimulus (FS) and Pattern Reversal (PR) stimulus. Visually evoked fields were recorded over the occipital lobe using OPM-MEG and SQUID-MEG for comparison. The visually evoked responses produce well-known signals with well-defined components, indicating the neuronal activity between different visual areas (primary and associative).

The understanding of the human visual pathway and early visual processing is extremely important in understanding the fundamentals of vision. Numerous studies have used electroencephalography (EEG) (94) and magnetoencephalography (MEG) (95) to investigate the stimulated cortical regions as response to a visual stimulation. The evoked responses are clear, well-shaped waveforms with positive and negative peaks (components) with well-defined onset after the stimulation. There are three

distinguished components: the early (P1), the main(P2/P100), and the late component (P3). These responses are well-characterised and any observed latencies might be correlated with pathological brain function (96; 97).

Visually evoked fields (VEF) are well characterized in humans (98), however there is limited information regarding the spatio-temporal localization of the propagating signal. Previous studies (99) tried to evaluate the interactions within the visual systems and further define the correlated function of the primary and associative visual areas with the component activation patterns. Weifeng Xu and Per Ronald have described interconnection of the primary visual cortex with associative visual areas using an invasive cortical feedback system in animal models (100; 99). Although the hierarchical activation and spatio-temporal processing of the evoked response is not determined in humans, some studies have shown that the early componment (P1) originates from the primary visual cortex (19; 101), while others indicate it originates from the extrastriate cortex (102; 103). Di Russo described these activation patterns and showed the main VEF component (P2/P100) could result from neuronal activation in extrastriate cortex without providing a specific region (104).

Coincident evoked responses from close neighboring cortical region can be recorded by neuroimaging systems with sufficient spatio-temporal resolution and close sensor positioning. In the following sections, the experimental results show the improved spatio-temporal resolution of the the OPM-MEG system compared to other neuroimaging methods i.e. SQUID-MEG or EEG. Hence, OPM-MEG has the potential to describe and analyse further the functional and structural connectivity among neighbouring cortical areas.

3.2 Background theory

Tracking the cortical propagating signal in response to a stimulation is challenging and requires the accurate determining of the activated cortical region as well as the time onset of the corresponding magnetic source. Spatio-temporal resolution is defined as the ability to simultaneously localize distinguished location and timing of neuronal activation. In the following sections, I provide a detailed description of the theoretical reasons that predict advantages in spatial and temporal resolution for

OPM-MEG over SQUID-MEG. With a focus on the spatial and temporal resolution of two systems, we need to evaluate the spatial and temporal resolution of the OPM-MEG system separately. The description below defines these terms and gives further explanation of the improved features of the OPM-MEG method.

3.2.1 Spatial resolution

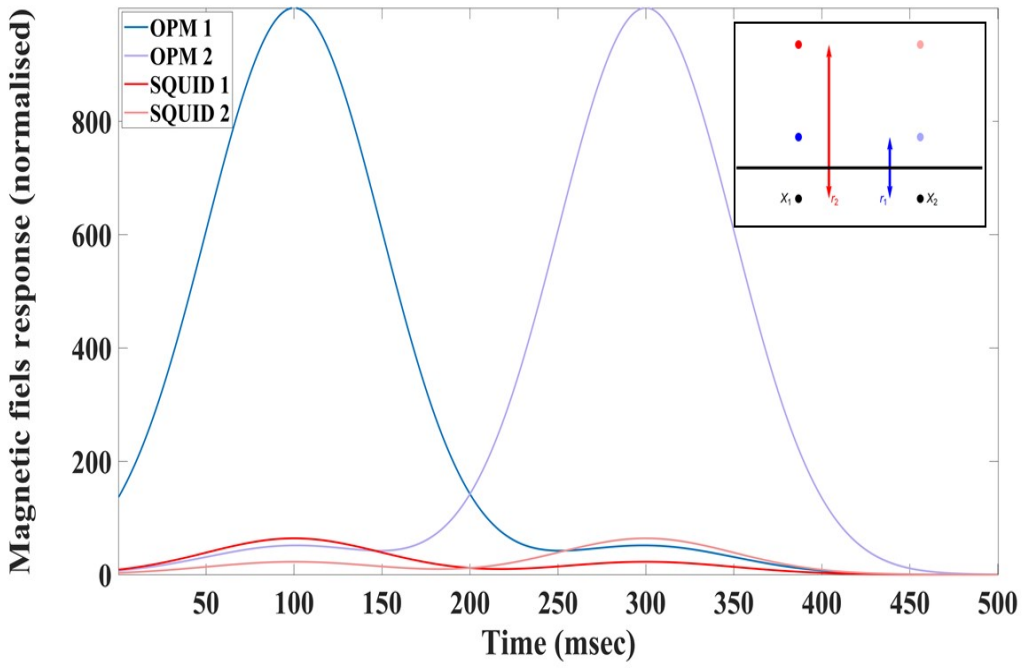

Figure 3.1: OPM and SQUID magnetic field measurements induced by two different sources (x_1,x_2), when the OPM and SQUID sensors have different source-to-sensor distance. The blue and the purple lines show the magnetic field recorded by the OPM 1 and OPM 2 respectively while the red and pink lines represent the magnetic field recorded by SQUID 1 and SQUID 2, respectively. *Inset*: Diagram of the SQUID sensor position (red and pink dot) and the OPM position (blue and purple dot) with respect to the sources x_1, x_2. The distance of the OPM sensor to the source is r_1 (blue arrow), and the distance of the SQUID sensor to the source is r_2 (red arrow). The sources x_1, x_2 have the same distance to the sensors.

OPM sensors can be placed independently and directly on the scalp, having a reduced offset distance up to $\sim 5\,\text{mm}$ compared to SQUIDs' offset distance ($\sim$ 30-

50 mm. Theoretical consideration (105) and brain simulations (88) predict the OPM-MEG system to have improved SnR, spatial resolution, and thus, improved source localization, when compared to the SQUID-MEG system.

Here, we define the spatial resolution as the minimum separation between two cortical sources in order to be distinguished from each other.

The magnetic field strength decays with the distance from the cortical source according to the power law, hence the signal detection is improved for sensors placed closer to the source, i.e to the scalp. The quantification of the improvement requires the distances between the two cortical sources and the magnetic field characteristics, which can not be estimated accurately within the brain. However, according to the Rayleigh criterion, the maximum distance two sources can be resolved is equivalent to the distance between the two sources (105) (figure 3.1). Consequently, as the OPM sensors are placed closer to the scalp than the SQUID sensors, the former can manifest higher spatial resolution.

3.2.2 Temporal resolution

The OPM-MEG temporal resolution is defined as the minimum required detection time among two distinctive neuronal activations in response to a stimulation. Limitation at the sensor level i.e. limited bandwidth, contribute to the systemic temporal resolution. The magnetic field pulse is a characteristic waveform with an amplitude, temporal width and uncertainty, which combined will define the temporal resolution of the system.

A typical MEG response consists of a sequence of magnetic pulses with characteristic wave patterns, which are averaged over many trials in order to be able to distinguish the cortical response. Through the averaging, we can quantify the uncertainty as a statistical standard error of the final averaged evoked response at each point in time. Thus, the quantitative temporal resolution is calculated as the time after a typical peak occurs before the signal value differs significantly with the one at the characteristic peak. As an example of this definition, we consider a Gaussian shape pulse $g(t)$:

$$g(t) = Ae^{\frac{-(t-t_0)^2}{2\sigma^2}}, \tag{3.1}$$

where A is the pulse amplitude, t_0 is the time onset of the pulse maximum occurs

and 2σ is the pulse width.

We define the temporal resolution of this signal shape as t_{res}, which can be quantified as the time between the maximum peak t_0 and the time after or before t_0 when the pulse is significantly lower than A, i.e. by an amount ϵ. The uncertainty ϵ is measured as the standard error and is considered as a time-independent variable in this example. Hence $g(t_0)$:

$$g(t_0) = g(t_0 \pm t_{\text{res}}) + \epsilon \tag{3.2}$$

Solving for t_{res} :

$$\pm\, t_{\text{res}} = \sigma\sqrt{-2\ln\left(1 - \frac{\epsilon}{A}\right)}. \tag{3.3}$$

Note this applies only if the ratio of the uncertainty to the maximum peak (ϵ/A) is less than one. Then, the signal-to-noise ration (SnR) can be quantified by the inverse ratio as: $\text{SnR} = A/\epsilon$, if $\text{SnR} > 1$.

The equation (3.3) can be simplified in the the 1st order Taylor expansion as:

$$t_{\text{res}} = \sigma\sqrt{\frac{2\epsilon}{A}} \tag{3.4}$$

Although MEG signals consist of multiple non-Gaussian pulses, the temporal resolution (t_{res}) is still equivalent to the ratio of the width w over the square rooted SnR ($t_{\text{res}} \propto w/\sqrt{\text{SnR}}$), and therefore the equation can also be applied to more general pulse signals, not only Gaussian pulses.

Determining the temporal resolution of our measurements requires the precise definition of the width w and the amplitude A.

We quantify the width w as the time difference between the two local minima among the pulse's maximum magnetic field, where the amplitude A is defined as the difference between the maximum pulse and the average of those two local minima (figure 3.3).

As an extension to the scaling, any recording method that enhances the amplitude A of a pulse while the width w and the standard error ϵ are maintained at similar values, results in an improved temporal resolution. Recent studies have shown OPM sensors approaching similar noise floor of SQUIDs (106; 44), hence we consider similar values of the standard error ϵ for both systems.

Hence, the improved time resolution of the system can be measured as the ratio $\eta = \sqrt{A}/w$. The increased η correspond to improved temporal resolution, i.e. shorter

t_{res}. The closer placement of the OPMs to the cortical sources enable recordings of higher amplitude pulses, which result in higher η. The metric η is developed for this work, and quantifies the temporal resolution of cortical measurements described in the section Methods 3.3. The ratio η might not represent the temporal resolution in other experimental protocols.

3.2.3 Vectorial Measurement

The magnetic field can be described as a vector. Most SQUID-MEG systems can measure one magnetic field component, radial to the brain. The fixed SQUID sensors inside the helium bath have a stand-off distance from the scalp of $\sim 50\,\text{mm}$ (93). As the orthogonal components tend to be weaker by the distance, the measured radial field tends to approach the field gradient values. In contrast, OPM sensors can be positioned with closer proximity to the scalp and record simultaneously multiple magnetic field gradients, resulting in enhanced spatial resolution (107).

The simultaneous recorded radial and tangential magnetic fields enhance the resolution of the system. At the sensor level, any magnetic field is characterized by the direction and magnitude. A single-axis sensor sensitive only to radial fields measures the projected field onto the same direction, and struggles to identify any rotational or magnitude change of the field vector. These limitations are extended when both direction and magnitude of the magnetic field change simultaneously; then the measured onset time of the peak magnitude can be misleading. By measuring an additional magnetic field component, the vector measurement helps to differentiate the altered magnitude and direction. As an example, we consider the sensors located close to the scalp are in a source-free region, where the current density J is zero ($J = 0$), Ampère's Law $\nabla \times B = \mu_0 J = 0$.

If the dual-axis OPMs measures the radial and tangential magnetic field components, then we can measure the missing component (axial), and hence measure the gradient of the magnetic field. However, the full magnetic field characterizations requires either a large number of sensors to achieve a full head coverage, or all three components recorded.

3.3 Methods

3.3.1 Participants

Visually evoked responses were measured in three healthy participants (one woman aged 47 years, 2 men aged 26 and 30). The participants had normal or corrected to normal vision. Prior to the experimental run, the participants were informed of the experimental procedure and purpose of the study and gave written informed consent to participate. The participants received a 3 T MRI scan (Siemens Magnetom Prisma, Siemens Healthineers, Erlangen, Germany) and a high-resolution T1-weighted anatomical scan at the Clinical Imaging Science Centre of the University of Sussex. For illustration purposes, a diffusion-weighted scan was acquired for one participant with two diffusion-weighting shells (b values = 1000 and 3000 s/mm^2). The data were used to reconstruct the optic radiation. The final reconstruction of the optic radiation in native space was obtained by the XTRACT (108) (figure 3.2 (d)(f)).

3.3.2 Experimental design

The study was approved by the Brighton and Sussex Medical School Research Governance and Ethics Committee (ER/BSMS3100/1). The OPM-MEG and SQUID-MEG, were taken in the same magnetically shielded room (Ak3b MSR, Vacuumschmelze, Hanau, Germany) at Physikalisch- Technische Bundesanstalt (PTB), Berlin, which was equipped with an external active shielding system. The MSR noise floor was sufficiently low and allowed the operation of the OPM sensors (52; 109).

Two standard full-field visual stimulation protocols were employed during MEG recording: a flash stimulus (FS), and a pattern reversal stimulus (PR). The stimulation parameters were optimised according to the standard guidelines for visually evoked potentials (110). The flash stimulus consisted of rapid white flashes with duration of 0.08 s (5 frames), followed by dark frames with presentation duration varying between 0.92 s and 1.00 s (55 to 60 frames). A single FS run was 300 s long (figure 3.2 (*a*)).

The pattern-reversal stimulus consisted of a standard black and white checkerboard (dimensions: 10 squares wide x 8 squares high) with the colours inverting

every 0.5 s (30 frame). Each PR measurement run had a duration of 280 s (figure 3.2 (*b*)). During the FS and PR stimulations, the participants were instructed to maintain their focus at the red dot, which was continuously projected onto the screen. Before the experimental run, each participant was positioned for the run in the centre of the MSR and were exposed to a three-minute dark adaptation period. During the participants' adaptation periods, the placed OPM or SQUID sensors were measuring the baseline brain activity in absence of stimulation. This helps the identification of the cortical response between the constant brain noise.

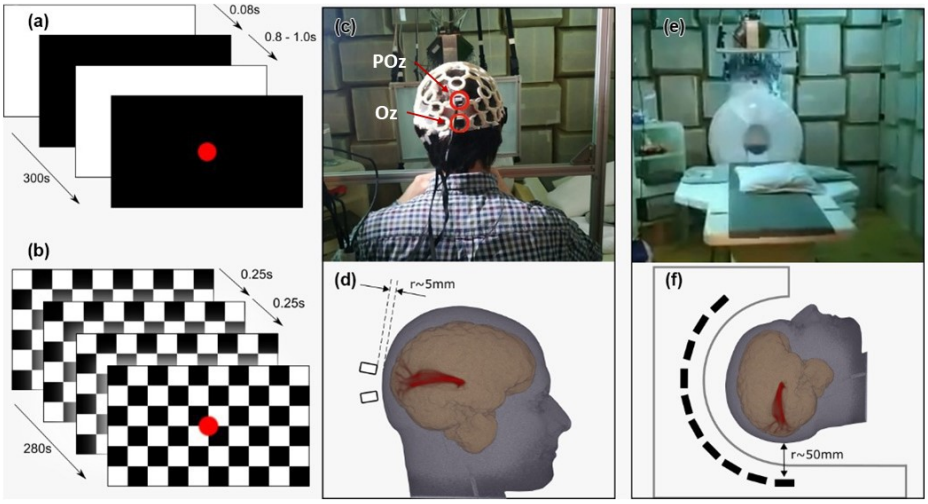

Figure 3.2: Experimental set-up of the OPM-MEG and SQUID-MEG systems along with the presented stimulation paradigms. (a) Flash Stimulation protocol (FS). Short white flashes (0.08 s) followed black frames (0.8-1 s) (b) Pattern Reversal (PR) stimulation protocol. The checkerboard colours are inverting every 0.25 s. The fixation point (red dot) was in the middle of each frame in both protocols. (c) A participant in position with the QuSpin sensors mounted in the 3D printed helmet. The sensors were placed over the visual cortex, at Oz and POz (red circle). (d) 3D MRI scan of Participant 1, illustrating the approximate locations of the OPM sensors 1 & 2, and scalp-to-sensor separation $\sim$ 5 mm. The optic radiation is shown in red. (e) MEGvision SQUID-MEG system. (f) Diagram of the MEG vision system showing the 50 mm standoff sensor-to-scalp distance.

In addition to "brain noise", we measured the empty MSR (background meas-

urements) to further evaluate the environmental noise floor. During these measurements, all the equipment were placed in the room as during the experimental runs, with the projector turned on and the OPM sensors placed in the same position, height, and orientation as if the participant was in. During the experiment run, participants were instructed to stay as still as possible and to sit upright in the plastic chain placed in the middle of the MSR. The sensors were mounted in a 3D-printed helmet and strapped carefully around the participant's head. Medical tape was used to protect the cortex from the sensor heating. A non-magnetic chin rest was used as the participants support aid to help reducing head movement when looking at the vertically orientated 50 cm × 34 cm screen. The stimulation was projected on a screen, placed in front of the participant, with a screen to eye distance of 53 cm. A 60 Hz LCD projector, placed outside the magnetically shielded room, was used for the stimulation paradigm and via a mirror system it projected the stimuli onto the screen in the MSR (figure 3.2 $(c)(d)$). The SQUID-MEG system required participants in a horizontal position, where the screen was placed horizontally above the subject. The eye-to-screen distance was 45 cm.

A detailed description of the OPM-MEG and SQUID-MEG systems is given below. The main differences between the number of sensors used and the parameters of the data acquisition system used are highlighted here.

3.3.3 OPM-MEG

The OPM-MEG system utilized two 2*nd* generation zero-field QuSpin magnetometers (QuSpin Inc., Louisville, CO, USA). The QuSpins sensitivity level is $<15\,\mathrm{fT/Hz^{1/2}}$ with bandwidth of 135 Hz. The dimensions of the head sensor is 12.4 x 16.6 x 24.4 mm.

The OPMs were mounted in a 3D printed helmet, design was altered to fit the QuSpin sensors (open-source design; OpenBCI Mark IV helmet). The OPMs were placed over the visual cortex at Oz and POz, according to the 10-10 system (111). The senors were placed over the Oz and POz position, which correspond to the primary visual cortex (V1) and the associative visual cortex (V2), respectively. Studies have shown a feed-forward and feedback activation pattern between the V1 and V2/V3 areas in response to visual stimuli (99). More specifically, (100) showed

an early activation of the V1, also known as P1 component, which is then repressed as it propagates to V2. From there, a reflected response travels back to the primary visual cortex (100).

The scalp to sensor distance was fixed by helmet design and sensor head, to approximately 5 mm. A customised python script was developed for the design and presentation of the stimuli in the stimulus PC. The stimulus PC was synchronized with the data acquisition system (DAQ). The OPM-MEG system utilized a Labjack T7 pro (Labjack Corporation, Co, USA) for the digital acquisition system (DAQ), with a sampling frequency of 1 kHz. All electronics, apart from OPM sensor-heads, were connected directly to the LabJack and the paradigm PC which were placed outside the magnetically shielded room.

3.3.4 SQUID-MEG

The SQUID-MEG system MEGvision (Yokogawa Electric Corporation, Japan) comprised of 125 axial gradiometers and 3 reference magnetometers (figure 3.2 $(c)(f)$)

To minimise any bias in the stimulus delivery, we used the same custom-written software and mirror set-up for the presentation. Although data from all sensors were recorded, only the SQUIDs nearest to the two OPM were used for the comparison and analysis.

The standoff distance from the participant's head to the SQUID sensor was ∼50 mm. The SQUID-MEG DAQ was the MEG Laboratory 2.004C (Eagle Technology Corporation), with a 2 kHz sampling frequency.

3.3.5 Data analysis

OPM and SQUID data, were analyzed using MATLAB and the FieldTrip toolbox (112). For the isolation of the frequencies of interest, a bandpass filter between 5 and 60 Hz was used in all the data. In addition to the bandpass filter, a bandstop filter between 49 and 51 Hz was used to suppress line noise. During the evaluation of the pre-processed data, any incomplete trials were removed. The epoched trials for flash stimulation (FS) were −45 ms to 350 ms, and for pattern reversal stimulation (PR) were 0 ms to 250 ms. Time-locked averaged responses include at least 380 trials for the FS stimulation, and more than 280 for PR. The evoked fields illustrated in

section 3.4 were the mean across all the trials for a single run. The uncertainty was defined as the standard error at each point in time of each of the averaged evoked response. To calculate our quoted signal amplitude values, we measured the value of the highest point for each peak and returned the standard error value at that location. The standard error of every time point reflects the signal amplitudes' uncertainties calculated with 0.5 ms time spacing for the SQUID system and 1 ms for the OPM system.

The η ratio was tested for both OPM-MEG and SQUID-MEG, aiming to compare their spatio-temporal resolutions.

For the comparison of the spatio-temporal resolution of the two systems, the η ratio was measured in the characteristic evoked magnetic field component as described in section 3.2.2.

The uncertainty of the η ratio was calculated as the propagating error of time and signal uncertainties. The magnetic field responses were initially measured at the Oz and POz cortical areas and then compared. The OPM-MEG method can concurrently obtain individual magnetic field component data (radial B_z and axial B_y) which were compared by measuring the planar projection B_{yz}, where $|B_{yz}| = \sqrt{B_y^2 + B_z^2}$. This approach effectively suppressed timing artefacts that could have affected the single-axis component measurements.

Pearson correlation coefficients measured the linear correlation between two signals and was used to determine coefficient correlations between runs and across participants. A coefficient correlation value ranged between $+1$ and -1 where $+1$ denotes a linearly correlated signal, and -1 being anti-correlated. A value of 0 shows no correlation between the signals.

Visually evoked responses are identified by three time components: the early (P1) component, the main component (P2 for FS and P100 for PR), and the late component (P3). For the component analysis we established the onset range for the main (P2/P100) and late components (P3) based on previous studies (19; 98; 102; 113; 114; 115). The FS and PR stimuli have a characteristic P1 component with onset between 35 and 60 ms, a main component (P2/P100) between 83 and 152 ms, and a late component (P3) between 160 and 230 ms.

The OPM-MEG experiment included a minimum of four FS runs and three PR

runs for every participant, while the SQUID-MEG included a single run for each stimuli. The averaged evoked fields for both systems were measured and analysed as detailed above.

3.4 Results

All the illustrated data were visually inspected and demonstrated good quality as described in the Data analysis (3.3.5).

FS and PR VEFs were in accordance with patterns expected from the literature (figure 3.3). High VEF consistency was observed between the PR and FS runs and across participants (figure 3.5). The within participant reproducibility was evaluated using the Pearson correlation coefficient for the Oz sensor. The Pearson correlation for the FS and PR stimuli are shown in table 3.1 and were measured as 0.83(4) and 0.85(2), for Participant 1, 0.70(7) and 0.24(8) for Participant 2 and 0.56(3) and 0.54(6) for Participant 3, respectively. The bracketed values are the standard error of the Pearson correlation. Previous studies have shown the higher SnR of the OPM-MEG system compared to SQUID-MEG (93; 88). Combining the already proven increased SnR with the η ratio, we showed the improved spatio-temporal resolution of the OPM-MEG system. The DAQ system did not achieve the optimal noise floor and a 10 Hz noise was constantly present in the measurements. As the visually evoked fields often exhibit an activation of the alpha band, between 8 Hz and 13 Hz, no bandpass filter was used to remove the DAQ system noise. However, to further verify our findings, when a bandpass filter is used, the same patterns are observed.

Figure 3.3 shows the recordings of the Oz OPM sensor and the corresponding SQUID for the FS. The left amplitude axis (y-axis) corresponds to the OPM-MEG measurement while the right amplitude axis corresponds to the SQUID-MEG amplitude. OPM VEF had approximately 4 times higher amplitude compared to the SQUID VEF, with the OPM signal maximum amplitude of 480(46) fT and the SQUIDs a maximum amplitude of 126(4) fT. The same activation patterns were observed in both methods, further verifying the OPM's measurements. Based on these VEF, we measured the ratio η for the OPM sensors as 0.5(6) $\sqrt{\text{fT/ms}}$, in

comparison to the SQUID η of 0.25(2) $\sqrt{\text{fT}/\text{ms}}$. Although the OPM MEG noise floor was non-optimal, the η ratio still showed the improved temporal resolution of the system compared to the SQUID MEG temporal resolution. The OPM evoked responses had more pronounced and well defined local maxima and minima leading to a significantly reduced temporal uncertainty.

Well-defined components helped distinguish the VEF from the cortical baseline, the brain's constant noise.

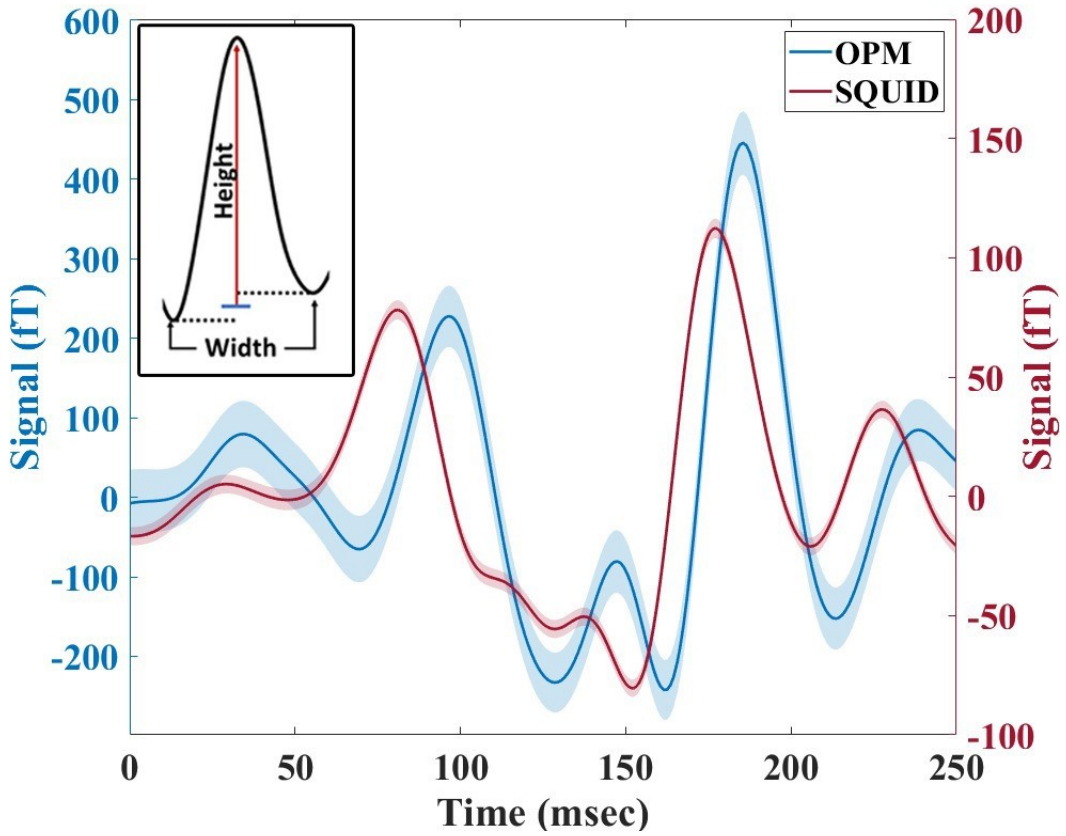

Figure 3.3: Averaged visually evoked field measured by the OPM-MEG and SQUID-MEG system for Participant 1 in response to flash stimulus (FS). Visually evoked fields recorded at the Oz cortical position using an OPM sensor (blue line) and the corresponding SQUID sensor (red line). The shaded area around the signal indicated the range of the standard error. Inset: The signal height (red line) corresponds to the amplitude difference between the peak maximum and the average of the two local minima (blue line). The width is the difference between the two time onsets of the local minima (dashed lines). The η is the ratio $\sqrt{A}/w$ of these two values.

Figure 3.4 shows the baseline measurement and the VEF for Oz in Participant 1. Although the baseline response reflects the constant activity of the human brain, the delivery of the visual stimulus alters the cortical baseline to a well-known and characterized evoked response. The differences between the baseline and the VEF helped identify the visually evoked responses. The baseline averaged response has a maximum amplitude of 94.8(55) fT compared to the 483(48) fT of the VEF response, while the activation patterns showed little to no similarities to the VEF activation patterns.

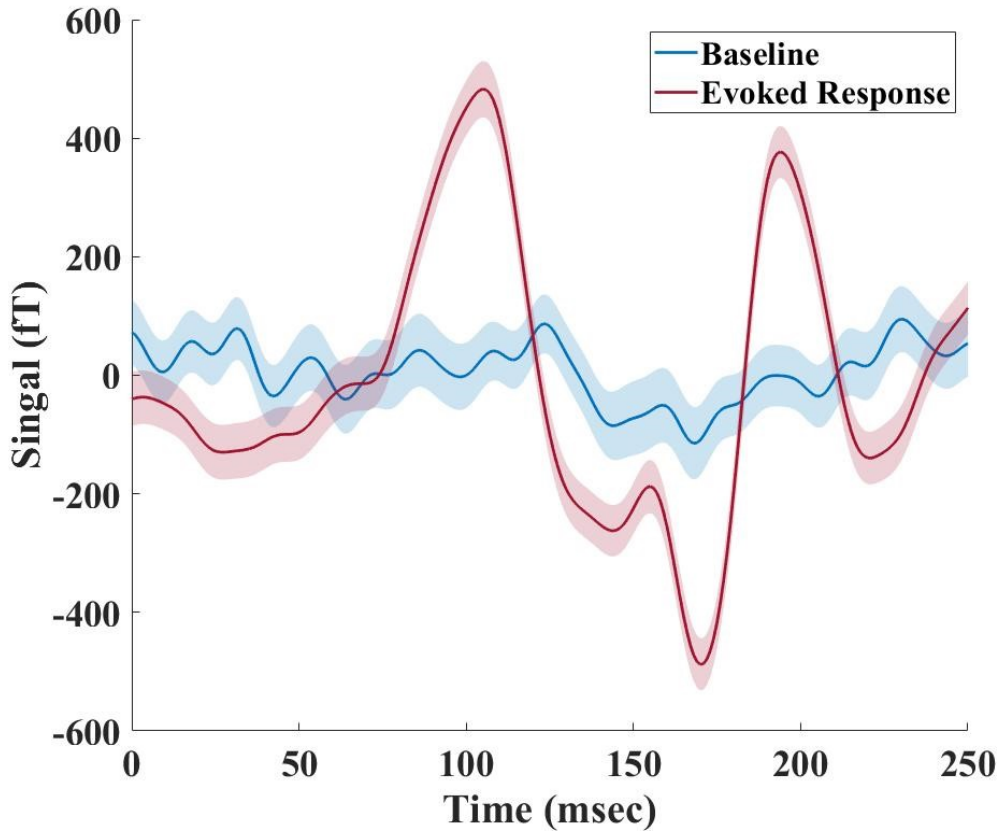

Figure 3.4: Averaged baseline cortical activity is compared to an averaged visually evoked field response. Both cortical activation were recorded by a single OPM placed over the primary visual cortex for Participant 1. The cortical baseline was recorded in absence of any stimuli (blue line), while the visually evoked fields were measured in presence of the flash stimulus (red line). The shaded area around the trace shows the standard error.

All the FS (a) and PR (b) averaged evoked responses for Participant 1 are shown in figure 3.5. The different runs were recorded at the Oz cortical position by OPM-

MEG. The mean of all the runs for both FS and PR traces is noted as a bold red colour and follows the same activation pattern with each individual run. Through both plots, the reproducibility of the evoked responses is shown with little variations, where the components have activation times comparable to the already known values from the literature. For the FS, the main component (P2) has a time onset between 100 and 135 ms, while the onset of the late component is between 180 ms and 190 ms. Similar accurate component onsets are manifested in the PR traces, with the main component (P100) activation from 128 ms to133 ms, and the late component (P3) onset from 210 ms and 214 ms.

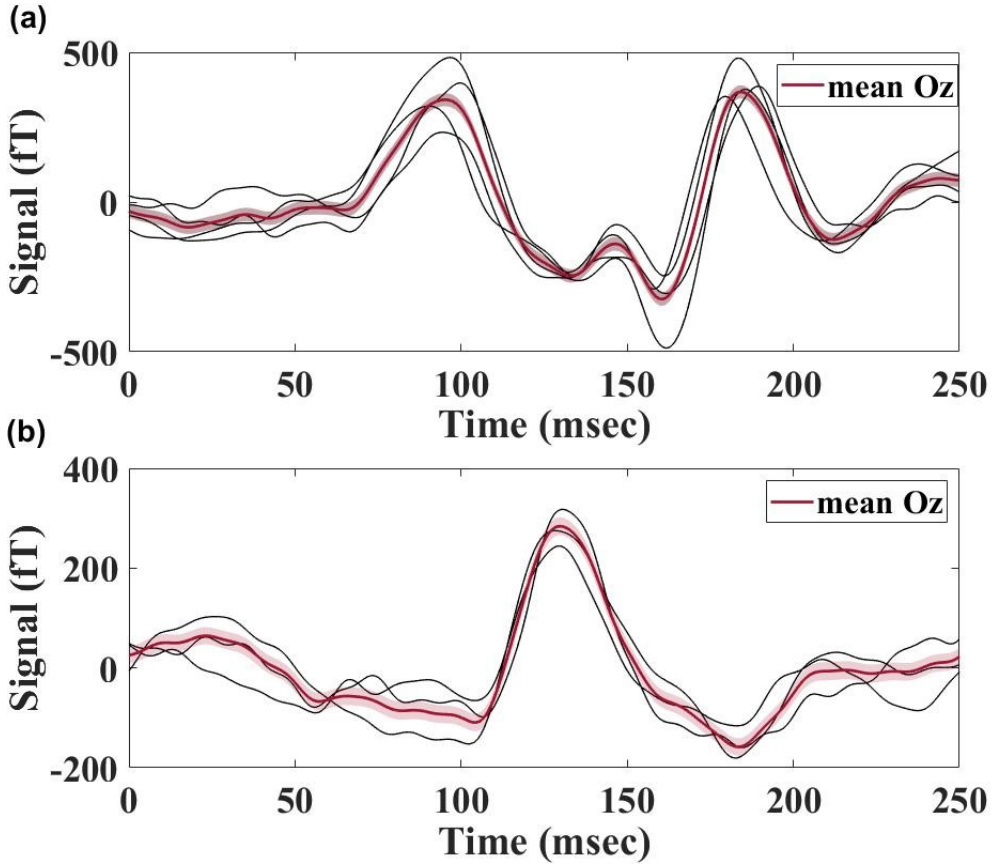

Figure 3.5: Visually evoked fields of Participant 1 measured by OPM-MEG system for (a) four flash stimulation (FS) runs and the mean of these evoked responses. (b) Three pattern reversal (PR) runs along with the mean. FS and PR individual run (black trace) illustrate the same activation patterns as the corresponding mean (red trace). The shaded area shows the standard error of the corresponding mean.

The reproducibility of the components onset and patterns are similar across the different runs and participants. Table 3.1 shows the Pearson correlation coefficient

across the FS and PR for each Participant. Participant 1 has similar activation onset, delays and patterns for both stimuli, FS and PR. Participant 2 displays similar onset and patterns for the FS, while the PR responses were slightly more variant. Participant 3 showed also similar activation pattern and delays for both FS and PR.

Stimulation	Flash Stimulus	Pattern Reversal
Participant 1	0.83 (4)	0.85(2)
Participant 2	0.70 (7)	0.24(8)
Participant 3	0.56 (3)	0.54(6)

Table 3.1: Pearson correlation coefficient across 4 FS and 3 PR experimental runs. All the compared measurements were recorded at the primary visual cortex. The bracketed values are standard error.

For the quantification of the reproducibility between the participants' VEF, the Pearson correlation coefficients were calculated for one run per stimulus between two participants. Runs with greater coefficient correlation values were selected. Table 3.2 displays an anti-correlation of Participants 1 VEF for both stimuli while Participant 2 and 3 show a moderate correlation for FS and PR stimuli. Differences of the anatomy of the cortical surface could lead to small variations of the evoked response. Hence, the observed anti-correlation of Participant's 1 VEF could originate from different cortical folding compared to the other two participants. Studies have showed the variability of the cortical folding effect the measured extracranial magnetic field and asymmetric results are often observed (116; 117).

Participants / Stimuli	Flash stimulation	Pattern Reversal
Participant 1-Participant 2	-0.53 (7)	-0.45(9)
Participant 1-Participant 3	-0.54 (7)	0.49 (9)
Participant 2-Participant 3	0.38 (8)	-0.35 (11)

Table 3.2: FS and PR Pearson correlation coefficient within participants, with the 95% confidence interval as bracketed values.

Further comparison between the two systems, OPM-MEG and SQUID-MEG, is displayed in figure 3.6, where a single run recorded by OPM-MEG (a) and SQUID-

MEG (b) for FS stimulus, shows the significant similarities and differences between the two systems and the two cortical positions Oz and POz. The OPM-MEG recording has an early activation (P1) at the primary visual cortex (Oz). Following the P1 activation, a time difference between the activation of the arriving signals at POz and Oz is observed. This time delay of the POz and Oz arriving signal is observed for the main component (P2) and the late component (P3). The time range for the expected onset of the P2 and P3 components is illustrated by purple bands as described in previous studies for the Oz EEG sensor (18; 19; 102; 113; 114; 98; 115). The bold dashed lines indicate the dominant peaks within these ranges and represent the peak onset of the main (P2) and late (P3) component. Furthermore, we denote $\Delta\tau_1$ and $\Delta\tau_2$ the time delay between the arriving signals at POz and Oz for both components; P2 and P3 and were calculated as 10(7) ms and 20(4) ms, respectively. The time delay between the two cortical regions was also reproducible. Figure 3.8 plotted the four FS run of Participant 1. The time delay between the arriving signals was observed in all four runs.

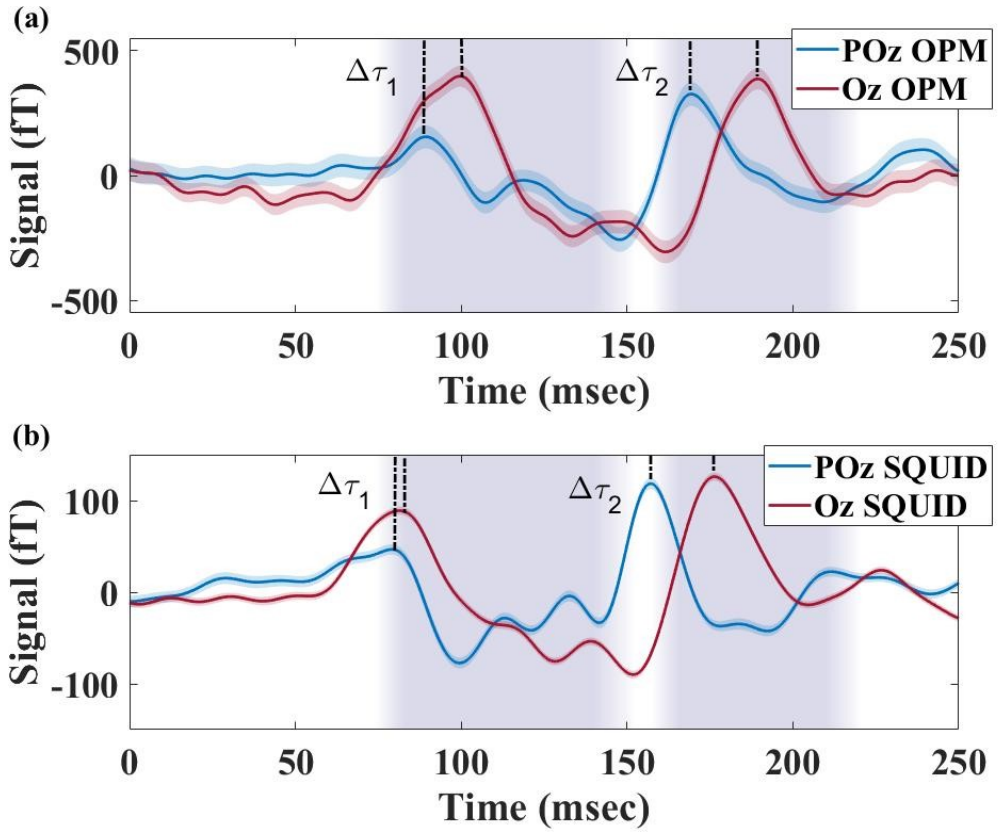

Figure 3.6: Visually evoked fields during flash stimulus measured by: a) OPM-MEG and b) SQUID-MEG for Participant 1. The highlighted areas show the limits where the Oz component onset is anticipated for each stimulus (19; 102; 113; 114; 98; 115). The dashed lines mark the peaks for Oz (red) and POz (blue) for both components P2 and P3.

The averaged time delay of all the four runs for Participant 1 was calculated for the main (P2) and the late (P3) component as $\overline{\Delta\tau_1} = 8(1)\,\text{ms}$ and $\overline{\Delta\tau_2} = 18(1)\,\text{ms}$. The SQUID-MEG measurements also showed the timing difference for the arriving signals in the corresponding SQUID sensors at POz and Oz. The SQUID recorded time delays differ from the ones measured by OPMs and were calculated as $\Delta\tau_1 = 2(5)\,\text{ms}$ and $\Delta\tau_2 = 18(3)\,\text{ms}$ (figure 3.6 (b)). The difference in $\Delta\tau 1$ and $\Delta\tau_2$ between the OPM and SQUID sensors might originate from the different sensors precise positioning and the distance from the scalp. In addition, the radial component recorded by OPM sensors is not fully aligned with SQUID sensors' sensitive axis. The higher SnR of the SQUID-MEG system compared to the OPM-MEG did not effect the uncertainties of the measured $\Delta\tau_1$ and $\Delta\tau_2$, as they have similar values in both systems, due to the improved η of the OPM-MEG.

Figure 3.7 shows the time delay for the arriving signal at the associative and primary visual cortex for the pattern reversal stimulation. The observed delays between the arriving signals are longer than the ones observed for flash stimulus, with $\Delta\tau_{1PR}$ =28(16) ms and $\Delta\tau_{2PR}$ =45(8) ms. The time delays for pattern reversal were also recorded by SQUID-MEG as; $\Delta\tau_{1PR}$=30(6) and $\Delta\tau_{2PR}$=57(5) The time difference for the arriving signals at the POz and Oz sensors for both, main and late component, is observed in all VEF, in both PR and FS stimuli, across runs and participants.

The OPM-MEG system measured components along two axis, here the y and z components, which were used to verify the neurophysiological origin of the observed time delay between the two neighboring cortical signals. Although recent SQUID-MEG systems include similar features, the system used here measured a single component.

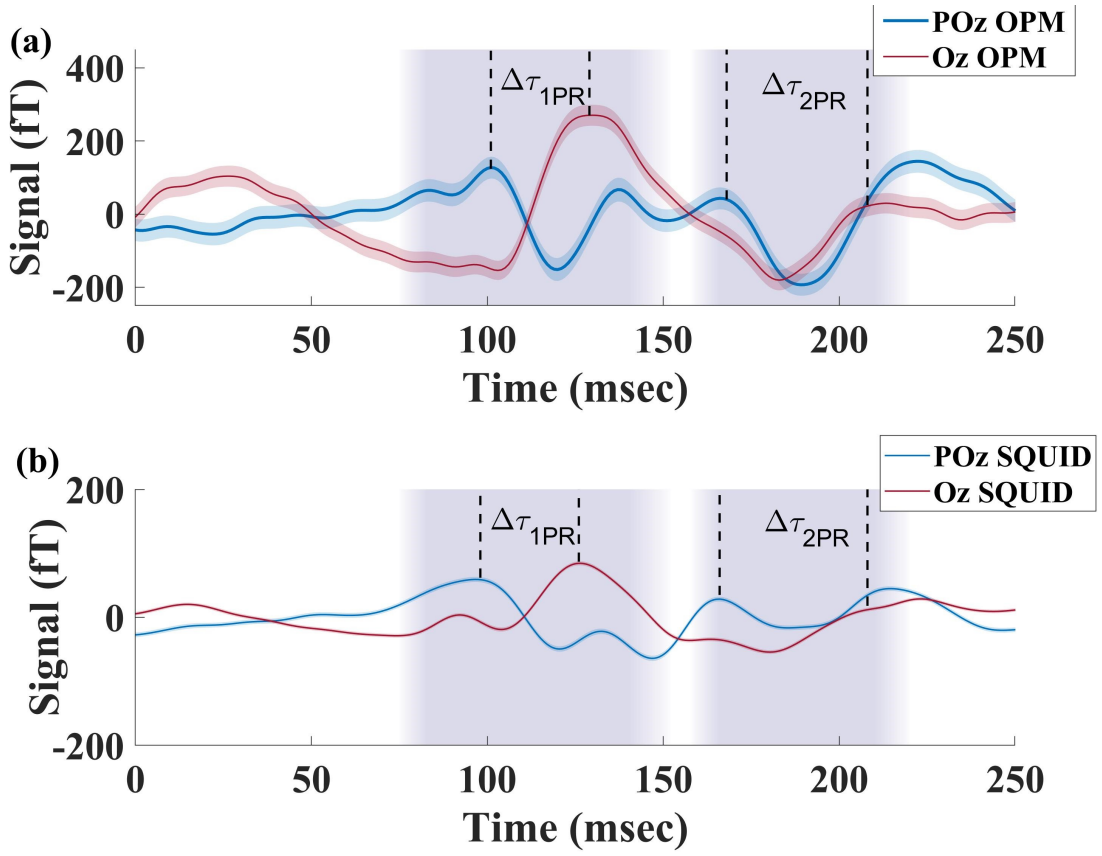

Figure 3.7: Pattern reversal visually evoked fields (VEFs) measured by: a) OPM-MEG and b)SQUID-MEG for Participant 1. The highlighted regions show the limits where the peak onset for Oz is expected for each stimulus (19; 102; 113; 114; 98; 115). The dashed lines mark the peaks for Oz (red) and POz (blue) for both components P2 and P3.

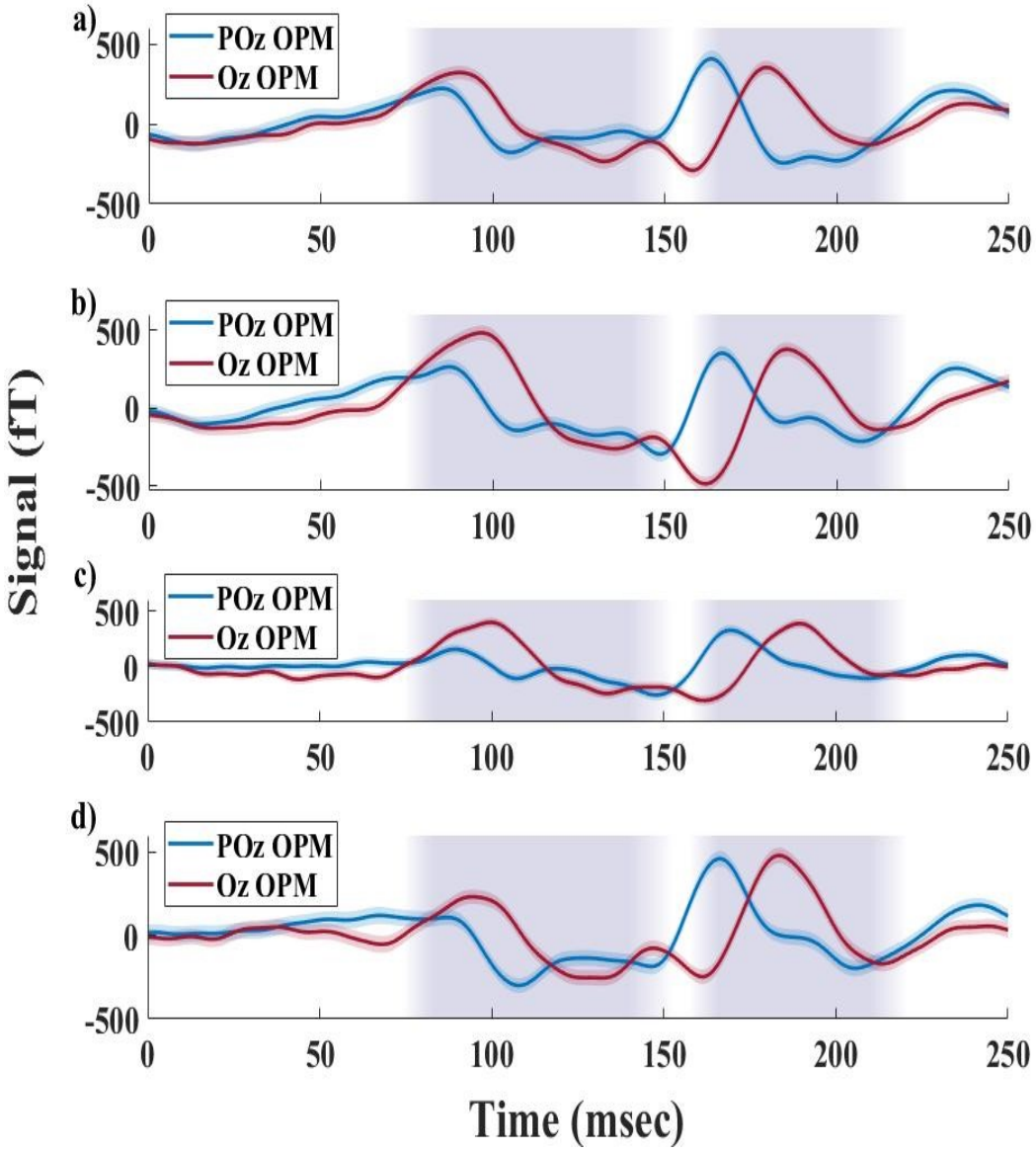

Figure 3.8: Flash stimulation VEF measured at POz and Oz by OPM-MEG system for Participant 1. The four different runs show similar activation patterns with consistent peak onset and amplitude. The time delay between the POz (blue) and the Oz (red) OPM sensors is observed for the two components across the runs.

The two magnetic field components B_y and B_z were simultaneously recorded by the Oz and POz OPM sensor. Figure 3.9 (a) illustrated a single FS run for the Oz and POz OPM sensors, where both B_y and Bz components for each sensors is plotted. The evoked response recorded at the z component B_z shows higher amplitudes and clearer activation patterns compared to the B_y signal. Figure 3.9 (b) shows the projected magnitude in yz plane, $|B_{yz}|$. The main characteristics of the VEF, like the different component onset and the time delays between the two sensors, can be easily observed in the vector component $|B_{yz}|$.

The time delay of the arrival signal between two close cortical regions, the associative visual cortex and the primary visual cortex, was constantly observed across participants and modalities (figure 3.9)and runs (figure 3.8).

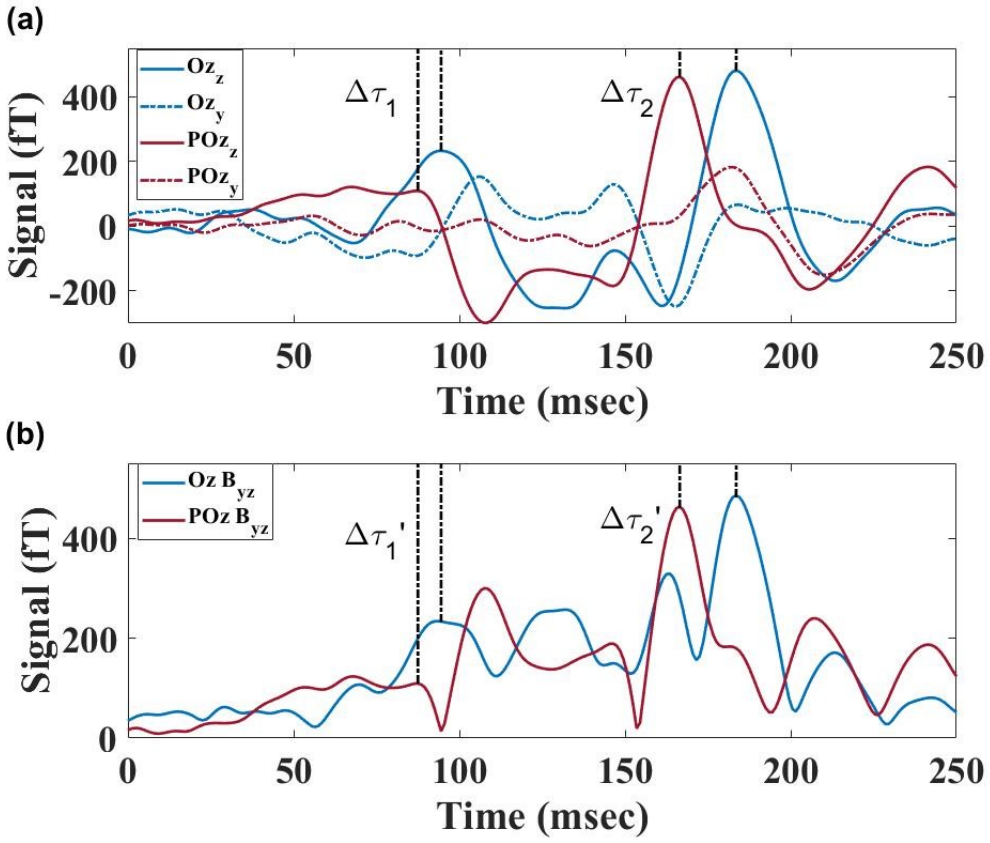

Figure 3.9: Visually evoked fields measured at Oz (blue) and POz (red) using OPM-MEG for FS stimulus. a) The Oz and POz averaged evoked responses along the z (bold) and y (dashed) directions. b) Projecting the magnitude of Oz and POz into the y-z plane. The dashed lines point to the time lag ($\Delta\tau$) between the Oz and POz OPMs.

3.5 Discussion

This pilot study showed the improved features of the optically pumped magnetometers in neurophysiological measurements through two different experimental modalities and configurations. Although SQUID-MEG is widely used in biomagnetic studies (29; 27), the method has shown some limitations due to the need of cryogenic cooling, such as the reduced signal-to-noise ratio and, thus the limited spatial resolution (88; 93). The use of OPM sensors can surpass the limitations of the SQUID based system. Combined with the known advantages of the OPM-MEG, the results indicated a significant improvement of the spatio-temporal resolution of the system. Along with the manifested spatio-temporal improvement, new insights into the cortical hierarchy in the occipital lobe of a human brain are found.

Two different visual stimulation were used; the flash stimulus (FS) and the pattern reversal (PR) in three healthy participants. Both systems were able to measure and reproduce characteristic brain patterns with different onset times.

To quantify the spatial and temporal resolution of the OPM system, the time onset of the evoked signal should be taken into consideration. Here, we introduce η as the ratio of the peak amplitude over the temporal width for the OPM-MEG and SQUID-MEG systems, and show a 2 times higher η for OPM-MEG compared to SQUID-MEG. The higher η of the OPM MEG system further confirms the additional benefits of the closer proximity of the OPM sensors to the visual cortex.

The presented results were reproducible, with similar characteristics across different runs, stimulations and participants. The continuous observation of the same patterns manifest the robustness of the new OPM-MEG method, further verifying the neurophysiological origin of the observed characteristics. Although variations of the cortical folding may show anti-correlation between the evoked responses between the participants, similar activation patterns and time delays were observed in all of them.

The measurements showed the OPM-MEG system can record evoked responses originating from a common source whilst propagating through different, neighboring pathways with high spatial and temporal resolution. Determining the arrival time of the signal between two distinct visual areas showed that the OPM-MEG system had significantly improved temporal resolution, hence could record the onset difference

between the two cortical activations. The enhanced η of the OPM-MEG provided similar or even lower time delay uncertainties compared to the SQUID-MEG system even though the SnR of the former was not ideal.

Consequently, the OPM-MEG method can provide important additional insights for clinical and experimental research. Having higher spatio-temporal resolution of a neuroimaging system could help in the better understanding of the neuronal connectivity of the brain in response to a stimulus, the order activation of superficial or deep cortical regions along with the observed frequency changes of the brain. Furthermore, neurodegenerative diseases, like Alzheimer's, Parkinson's or mild cognition impairment, can show alterations in the frequency domain as they progress, which could be monitored in detail in order to evaluate a therapy strategy using the OPM-MEG system. In addition to monitoring the progression of the disorder, OPM-MEG could potentially provide significant insights in the preclinical stage by searching for biomarkers; small abnormalities of the brain activity could indicate a potential onset of Alzheimer's disease (118).

Although the presented study was well-defined and characterised, there were some limitations in the experimental protocol and set-up to be improved in the next experiments. First of all, the number of participants was limited and even though the results were highly reproducible among them, having a greater sample size could provide additional information and higher verification of the final results. Future research should focus on a larger population and on using different type of stimuli to further explore the full potential of the spatio-temporal resolution of the OPM-MEG system. Finally, an improvement of the DAQ system noise floor could further enhance the SnR of the OPM-MEG and spatio-temporal resolution.

Chapter 4

Modular optically pumped magnetometer for neuroimaging

(Adapted from archived paper: Thomas Coussens, Christopher Abel, Aikaterini Gialopsou, Mark G. Bason, Tim M. James, Fedja Orucevic, and Peter Kruger. Modular optically-pumped magnetometer system. 5-6 2021. Atomic Physics (physics.atom-ph))

Current OPM technologies provide significant advantages in neurophysiological measurements compared to other sensors (such as EEG (119) or SQUID sensors (50)) but the designed configuration limits the performance of the OPMs without utilizing their full potential. In order to fully exploit the capabilities of OPMs, a new configuration of OPM sensor, the rubidium (^{87}Rb) modular OPM, was developed by our team, and tested in biomagnetic measurements. This sensor has improved bandwidth compared to commercially available sensors, and has the potential for the development of an integrated gradiometer OPM array, with reduced noise level and same sensitivity.

This chapter describes the configuration and operation of the modular OPM focusing in particular on the design features that make it more ideal for neurophysiological measurements. Alpha brain rhythms were recorded for two participants using the single-axis configuration of the modular sensor. Due to the outbreak of COVID-19 pandemic and lack of the magnetically shielded room in our facility, we tested

the modular OPM for biomagnetic measurements in a large magnetically shielded cylinder (MSC), big enough to fit a human participant. The ^{87}Rb modular OPM was designed, developed and operated by Thomas Coussens. I tested the suitability of the sensor for cortical measurements, by designing the experimental protocol and analysing the data.

The experimental protocol and methodology of the cortical measurements in this chapter were conceived and designed solely by the author. The modular optically pumped magnetometer was designed and developed by Thomas Coussens. The magnetic sensor and the data acquisition hardware and software were set-up and calibrated by Thomas Coussens with assistance from the author. The methodology and protocol for the sensitivity measurement of the modular magnetic sensor were designed solely by Thomas Coussens. All the cortical measurements were taken mainly by the author, with assistance of Thomas Coussens. All the analysis was performed by the author with assistance by Tim M. James. The results of the cortical measurements were interpreted by the author, while the sensitivity results were interpreted bu Thomas Coussens.

4.1 Introduction

Magnetoencephalography uses quantum sensors to measure neuronal magnetic fields and, until recently, SQUIDs were the sensors of preference. (120; 75). New technological developments (44) improved the sensitivity of the already existing optically pumped magnetometers and enabled the use of OPMs as an alternative sensor for MEG with enhanced spatial and temporal resolution (50).

Before the commercially available product, T. H. Sanders and colleagues developed a ^{87}Rb chip-scale atomic magnetometer for MEG. The sensitivity of the ^{87}Rb sensor was 200 fT/Hz$^{1/2}$ with a bandwidth up to 150 Hz. This sensor aimed to address the manufacturing and operating cost of the SQUIDs and the scalability issue of the existing OPM sensors, achieving a potential low-cost sensor with head footprint comparable to EEG and SQUID. Having a sensor head volume of $\sim$ 1 cm^3 could allow the development of a multi-channel system or combination with other neuroimaging methods, i.e. EEG. Measurements of a healthy brain were ob-

tained for two different experimental paradigms. The design and operation of the magnetometer is described here: (121).

A 20 channel ^{87}Rb OPM array was developed in 2018, enabling a prototyping OPM-MEG system (71). The 20 channel OPM array was embedded inside a human-sized magnetically shielded cylinder and spatially separated in five different modules, using a gradiometer configuration. Each module consisted of the four different channels, separated by 18 mm distance, having gradiometer sensitivity of $<5\,\mathrm{fT/Hz^{1/2}}$ and bandwidth $\sim$ 90 Hz (122). Cortical neurological measurements were recorded in response to two different stimuli and further validated the system. The high quality somatosensory and auditory evoked fields coupled with the high sensitivity of the ^{87}Rb OPM array, shows the potential of this OPM-MEG system. However, the fixed positioning of the sensors in the human-sized cylinder could be limited for studies where whole-head or bilateral coverage is required.

In addition to the ^{87}Rb OPMs, W. Fourcault and colleagues developed a ^{4}He OPM. The ^{4}He OPM was shown to have a sufficient sensitivity for neurophysiological measurements of $\sim 50\,\mathrm{fT/Hz^{1/2}}$, and an increased bandwidth of 2 kHz while no heating was required for the operation (54). Even though studies have used prior designs of the ^{4}He OPM for neuroimaging (122), the newly altered ^{4}He OPM has not yet been tested for cortical measurements.

Although OPMs have shown great potential for neuroimaging applications, a series of limitations have so far prevented the production of a fully integrated system. The measurement quality of closely positioned OPMs suffers from cross-talk artifacts, with minimum space separation distance of 2 cm (47), and the individual wiring interfering with the recorded signal (89). A solution could be the development of an OPM array system with a common light source that could significantly reduce noise (122).

The limited bandwidth of the sensors might be sufficient for low frequency cortical responses (<100 Hz), but is unsuitable for high frequency biomagnetic signals (> 600 Hz) which have been previously reported in spinal cord measurements (91; 92) or somatosensory studies (90). Finally, the operation of the OPMs requires heating the ^{87}Rb cell to elevated temperature, which might feel uncomfortable to the participant, highlighting the need for further standoff distance to cope with thermal

insulation.

The configuration and operation of the newly developed ^{87}Rb modular OPM is briefly described here (53). Only a brief summary is provided here. The new sensor is designed with modularity and scalability in mind, further exploiting the broader bandwidth without limiting the sensitivity of the system. Through a variety of magnetometry schemes and sensing regimes, we showed the modular ^{87}Rb OPM could provide novel neuroimaging applications, leading the way to the development of a dense OPM array. Due to the common light source and beam distribution of the modular OPM array, laser noise artifacts can be minimised. As a pilot study, we used the modular OPM to measure the alpha brain rhythm of two participants, further proving the suitability for neuroimaging recordings.

4.2 Method and Analysis

4.2.1 Modular OPM

The modular ^{87}Rb OPM consists of multiple 3D printed parts which can be connected to achieve different systemic layouts. The dimensions of each module are 45 x 45 x 40 mm.

Poly-carbonate material was used for the construction of durable and flexible modules, having a glass transition temperature of 139 °C (123). The configuration of the sensor included the light source module, the main sensor and the beam distribution (figure 4.1). The light can be generated and delivered internally by a vertical-cavity surface-emitting laser (VCSEL) or delivered externally via optical fibres. The main sensor consisted of: the vapour cell, the optical components, the magnetic field coils and the photodiodes. These parts were designed for flexible re-arrangement or replacement according to the desired measurement. The beam distribution modules distribute the light, providing flexible and independent sensor positioning.

To test the sensitivity of the modular OPM, we used the single-axis gradiometer configuration, which consisted of the light module and two senors modules (figure 4.1 (*b*)) . The additional beam distribution part was not used. Based on this configuration, a multi-axis gradiometer system can be easily extended to a system

array (figure 4.1 (*a*)). For the cortical measurements, we used the single module configuration, which consisted of the light module and a single senor module.

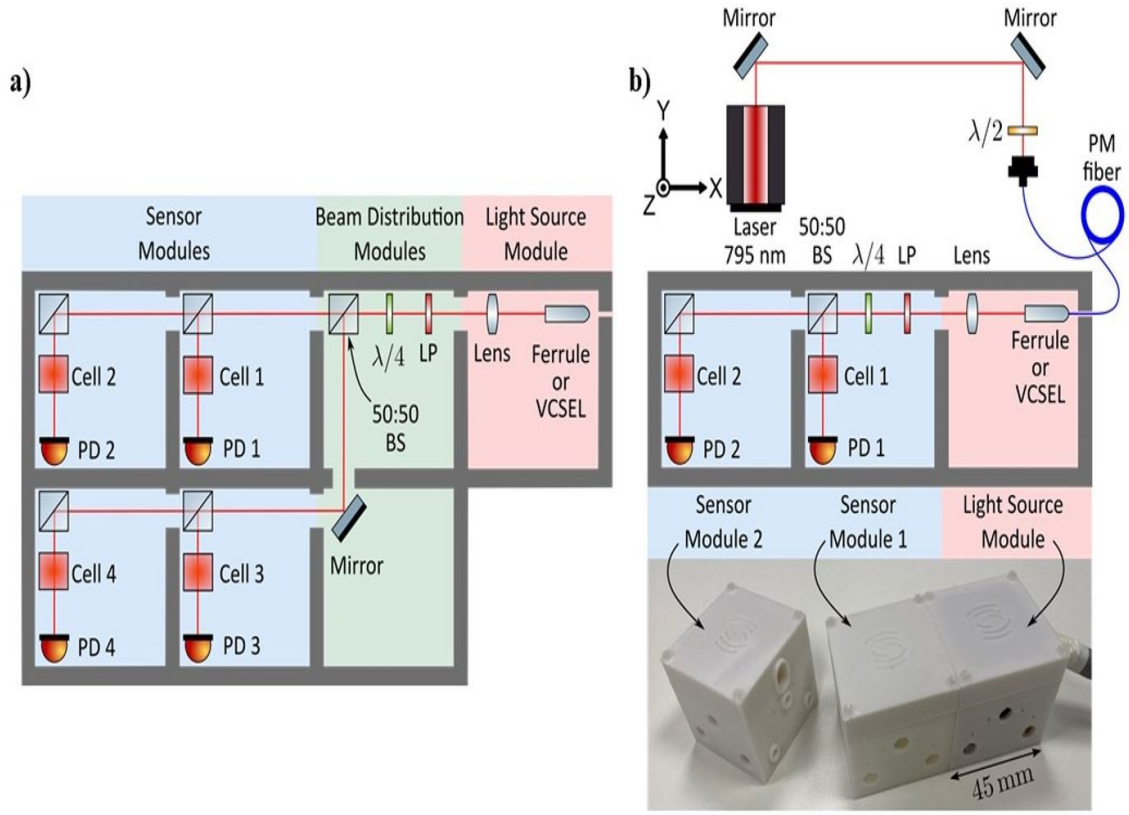

Figure 4.1: (a) Multi-axis gradiometer configuration using four sensors in a 2×2 array (blue), a light source (pink) and beam distribution (green). In the laser beam are placed lens, linear polariser (LP) and quarter-waveplate ($\lambda/4$). Opposite of the cells are the photodiodes (PD). The 50 : 50 beam splitter (50 : 50 BS) and the mirror direct the probe light to all four sensors. (b) Single axis gradiometer used in the sensitivity measurements, consists of the light source (pink) and two sensors (blue). The dimensions of each module for both multi-axis and single-axis are 45 x 45 x 40 mm. The single-axis magnetometer configuration, which was used in cortical measurements, can be achieved by removing one sensor module (i.e. sensor module 2)

The sensor operated in the spin exchange relaxation free (SERF) regime (see Chapter 2.4), where high density ^{87}Rb atoms in a close-to-zero magnetic field improve the sensitivity of the OPM system (124). The principles of the modular OPM operation are similar to other OPM systems and described in Chapter 2.4.

The main sensor module monitored the power changes of the polarized laser beam probing the vapour cell. A magnetic field perpendicular to the laser beam results in pumped ^{87}Rb atoms and Lorentzian transmitted light, where the final signal is produced. The required atomic density of the SERF regime is achieved by heating twisted wires, wrapped around the vapour cell. The alternating current frequencies were higher than the rubidium atomic response bandwidth at 81 and 200 kHz. In the single-axis gradiometer set-up, the external light source was used instead of the VCSEL.

The polarisation maintaining optical fibre delivered into the light source module the tuned light to the ^{87}Rb D1 transition (795 nm). Then, the polarised beam was collimated, circularly polarised and split by a 50:50 beam splitter cube. The glass ^{87}Rb cell with dimensions of 5 mm×5 mm×5 mm receives the reflected beam in the sensor module, while the other identical reflected beam was directed at the ^{87}Rb cell of the next sensor module. In order to monitor the alternating beam power, the photodiodes were placed opposite to the cells and then fed to a pair of lock in amplifiers before being connected to the DAQ.

4.2.2 Participants

Visually evoked fields were recorded in 2 healthy participants (1 woman), aged 29 and 30 years, with normal or corrected to normal vision. The 2 participants had 3 T MRI scans at University of Sussex. The study was conducted in accordance with the Declaration of Helsinki Ethical Principles, and was approved by the Brighton and Sussex Medical School Research Governance and Ethics Committee (ER/BSMS3100/1); all participants gave written informed consent to take part, after explanation of the procedure and purpose of the experiment.

4.2.3 Set-up

Cortical measurements

All MEG measurements were taken in a three layer μ-metal MSC. The cylinder had sufficient space for a participant laying in, with the head next to the modular sensor, placed on the back end of the MSC (see figure 4.2). The cylinder's internal diameter

and length were 50 cm and 100 cm, respectively. A wooden table was placed at the end of the MSC to support the the lower body of the participant (see figure 4.2 *c*). The single-axis magnetometer modular OPM was mounted on a wooden block and placed at the centre of cylinder's back end (see figure 4.2 *b*). Poly-carbonate material was also used for the 3D-printed OPM mount (see figure 4.2 *a*) The overall distance from the bottom surface of the mount to the OPM cell centre was 13.5 mm, while the sensor extended 17.5 mm outwards over the mount.

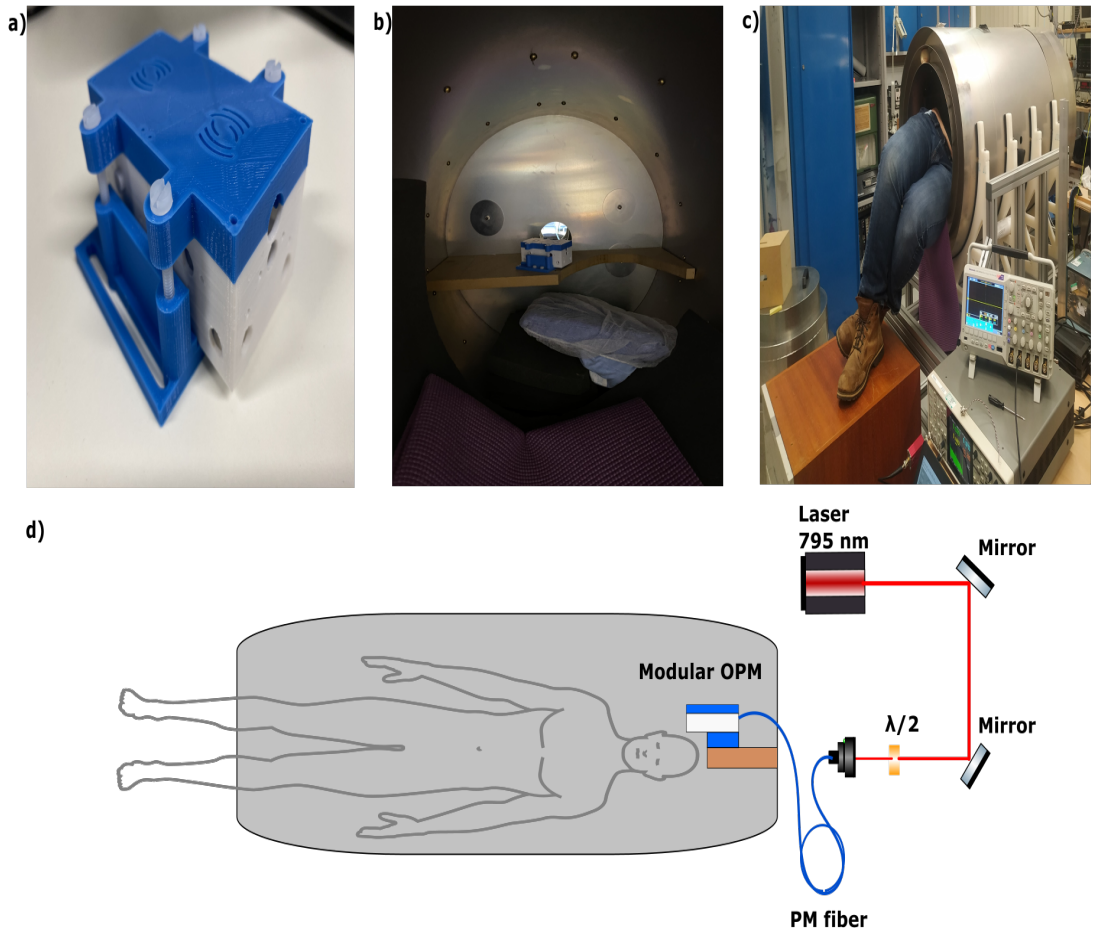

Figure 4.2: Experimental set-up of the modular OPM during neuroimaging measurements. (*a*) ^{87}Rb modular OPM and the 3D printed mount. (*b*) The mounted modular OPM on the wooden block and placed in the middle of the MSC prior to the participant's entry. (*c*) Participant laying inside the MSC with the occipital cortex (back of the head) attached to the sensor. (*d*) Schematic representation of the set-up. The external light source is connecting into the light source module placed in the MSC via optical fibres.

The cortical responses were measured by the single-axis magnetometer modular

OPM, which consists of the light module and one sensor module (see figure 4.1). A 795 nm laser delivered externally the light into the light sensor module of the modular OPM, placed inside the MSC. The system was sampled by a Labjack T7 pro, with a sampling frequency of 200 Hz. All electronics, except the modular OPM head, were located outside the MSC, directly connected to the DAQ and synchronised with the stimulus PC.

Before the placement of the participant into the MSC, the optimum placement of the sensor was marked over the occipital cortex according to the 10-10 system (111). The primary visual cortex (Oz) generates the stronger spontaneous brain responses, placed at the central posterior brain. A 5 cm x 5 cm medical tape was placed on the marked area to protect the head from overheating. The participants were instructed to lay in the cylinder facing on their right side, and place the marked area over the modular OPM. Following this step, the researcher evaluated the positioning and instructed the participant with any changes.

We confirmed the noise level of the MSC was sufficiently low for the modular OPM operation, with magnetic noise lower than 17 fT/Hz. The participants were asked to minimize their movement during the experimental run ($\sim$ 150 s) while between runs, there were short breaks of $60-120$ s.

Sensitivity measurements

The modular OPM sensitivity was measured in a small four layer μ-metal cylinder (MS-2, Twinleaf LLC), with magnetic field fluctuations lower than 10 nT and noise level below $10\,\mathrm{fT}/\sqrt{\mathrm{Hz}}$. The applied modulation fields were generated by the cylinder's internal coils, while the offset fields were generated by the coils placed inside the sensor module. Two sensor modules were used in a single axis gradiometer configuration, with the ^{87}Rb vapour cells heated at 129 °C and 124 °C. Although the optimal sensitivity of ^{87}Rb cells appears at 150 °C (87), we showed that the sufficient sensitivity for particular MEG measurements can be achieved in slightly lower temperatures.

4.2.4 Experimental protocol & Analysis

As a case study, spontaneous alpha brain responses were recorded for two participants using the modular OPM. In humans, the alpha waves have a frequency onset of 8-13 Hz (125) and are more prompted over the parieto-occipital lobe (126). Alpha waves are enhanced upon light blocking i.e. eye closing, and highly suppressed upon eye opening. Here, a simple paradigm showed the excitement and suppression of the alpha brain waves.

The suitability of the modular OPM sensor as a neuroimaging system was tested in three runs. In the first run (Run_1), the two participants were instructed by a prerecorded voice to open and close their eyes every 10 s for 150 s. Participant 1 was asked to participate in two additional runs. In Run_2, the participant was asked to keep their eyes open for 60 s and in Run_3 to do the opposite for the same duration. Run_1 consisted of 15 trials (opening/closing state). Further validation of the results derive from highlighting the absence and the presence of the alpha rhythm for the two conditions (Run_2, Run_3).

The modular system was synchronised with the presentation software. The data were analyzed using MATLAB. Evaluation of the pre-processed data removed any trials with interrupted recordings. As the main focus was observing the alpha rhythm, a frequency domain analysis was required, with frequencies of interest (FOI) ; 8 Hz - 13 Hz. For each run, the raw data was analysed in Fourier space as a spectogram and periodogram. There was no need for additional filtering nor averaging through the trials. The alpha brain rhythm can be observed for Run_1 and Run_3.

4.3 Results

Participants' induced responses are consistent with patterns known from the literature (4). A consistent alpha activation during Run_3 and the periodical appearance of the alpha rhythm during Run_1 further validates the suitability of the modular OPM sensor for neuroimaging studies.

Figure 4.3 shows the cortical activations for Participant 1 and Participant 2 during Run_1. Spectograms in figure 4.3 $(a), (b)$ plot the cortical activation between the FOI. The intensity of the alpha activation ranges between $0.7\,\mathrm{pT/Hz^{1/2}}$ and $1\,\mathrm{pT/Hz^{1/2}}$ for Participant 1, and $0.5\,\mathrm{pT/Hz^{1/2}}$ -$0.8\,\mathrm{pT/Hz^{1/2}}$ for Participant 2. The white trace indicates the audio cue (similar to a TTL pulse), instructing opening/closing eyes every 10 s, with high periods signaling the eyes-open condition, and low periods the eyes-closed. The spectral density of each run reveals the enhanced frequencies (alpha rhythm) for the run. FOI are highlighted with a red coloured bar between 8 Hz and 13 Hz. The correlation between alpha rhythms for eyes open/closed to the stimulus are clearly observed for both participants.

Differences between the induced responses of the two participants are observed (117; 116). Participant 1 has enhanced alpha activation during light-blocking and significantly suppressed alpha rhythm upon eyes opening. The induced response in the FOI extend from $0.6\,\mathrm{pT/Hz^{1/2}}$ to $1\,\mathrm{pT/Hz^{1/2}}$ (figure 4.3 (a)). The linear density shows the alpha activation of the FOI compared to the other frequencies, with a maximum peak at 10 Hz of $0.6\,\mathrm{pT/Hz^{1/2}}$ (figure 4.3 (c)). The 50 Hz electronic noise and the corresponding harmonic are also observed. Although Participant 2 has similar activation patterns to Participant 1, the intensity of the alpha rhythm differed (see figure 4.3 $(b)(c)$). The observed alpha activation ranged from $0.4\,\mathrm{pT/Hz^{1/2}}$ to $0.8\,\mathrm{pT/Hz^{1/2}}$. However, the linear density had a significant activation in the FOI, with a maximum peak at 10 Hz of $0.56\,\mathrm{pT/Hz^{1/2}}$.

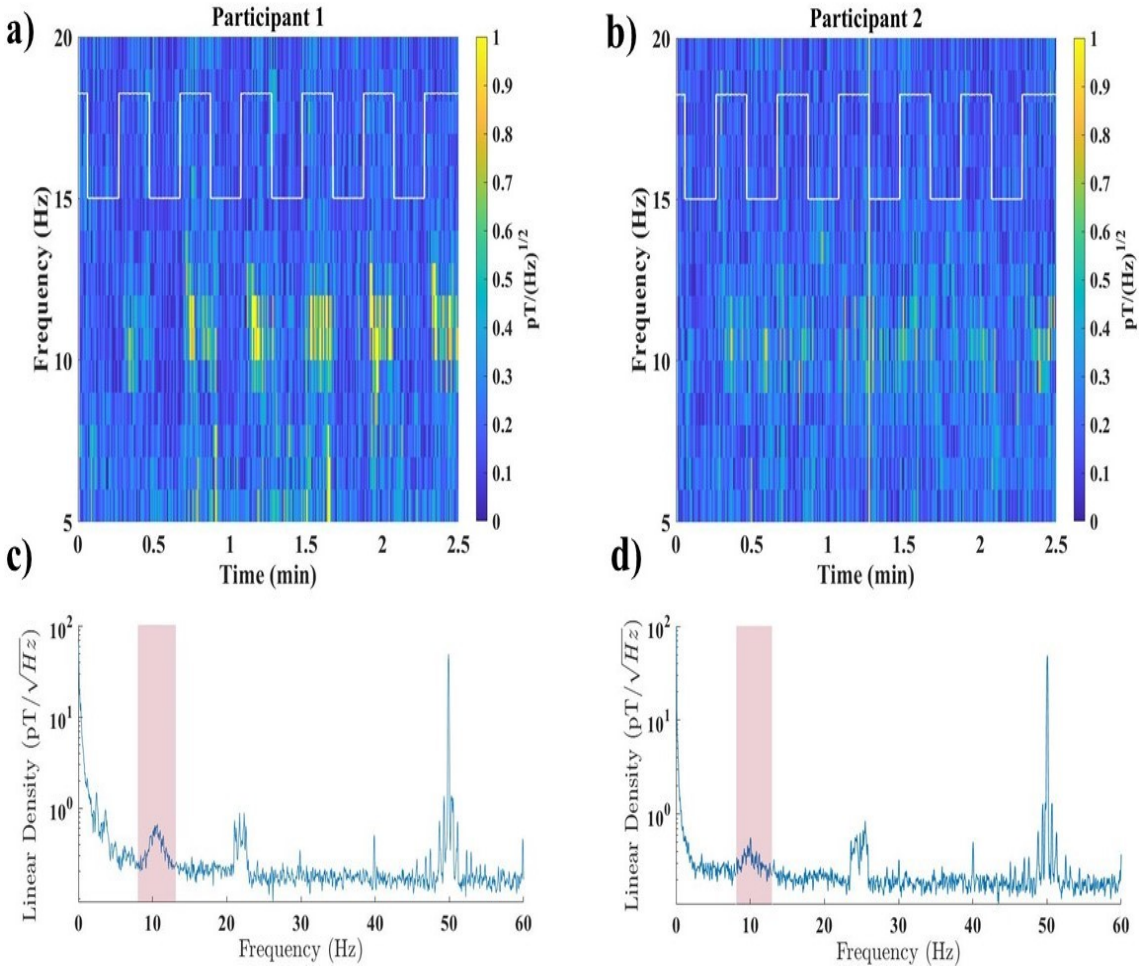

Figure 4.3: Alpha rhythms for Participant 1 $(a)(c)$ and Participant 2 $(b)(d)$ during Run_1. $(a)(b)$ Spectral density of cortical activation in Run_1. The colour bar indicates the intensity of the neuronal activation in the FOI. The white trace shows the audio trigger, with closing eyes for the upper trace. $(c)(d)$ Linear density of cortical activations. The FOI are highlighted by the red coloured bar between the frequencies; 8 Hz and 13 Hz.

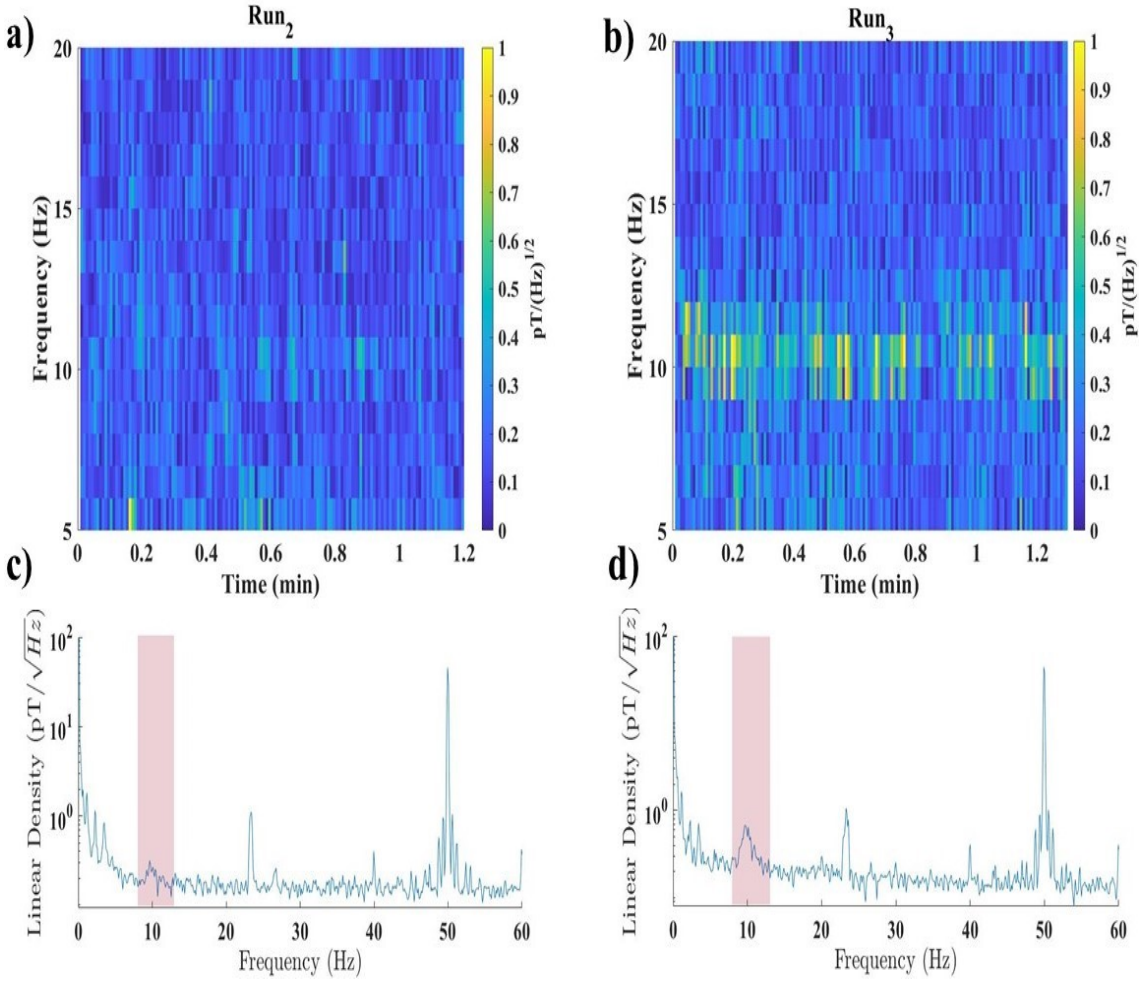

Figure 4.4: Induced responses for Run_2 and Run_3 recorded by the modular OPM for Participant 1. (a)(c) Spectral and linear density of the cortical response for Run_2, (eyes open) 1.2 s. Spectrogram's colour bar shows the intensity range. The red bar covers the FOI in the periodogram between 8 Hz and 13 Hz. (b)(d) Spectrogram and periodogram of the brain responses during Run_3, where the participant was asked to keep their eyes closed. Spectrogram's colour bar indicates the intensity range. FOI are highlighted by a red couloured bar in the periodogram.

The enhanced and suppressed alpha rhythm can be clearly observed in Figure 4.4. Participant 1 was asked to keep their eyes either open (Run_2) or closed (Run_3) for $\sim 1.2\,\text{min}$. In Run_2, the alpha activation was highly suppressed (figure 4.4$(a),(c)$). The spectral density did not reveal any enhanced cortical activation within the FOI, with the intensity ranging from $\sim 0.01\,\text{pT/Hz}^{1/2}$ and $0.4\,\text{pT/Hz}^{1/2}$. The linear density further confirmed the alpha suppression, with maximum onset intensity of $0.3\,\text{pT/Hz}$ at $9.6\,\text{Hz}$ (figure 4.4 (c)).

Figure 4.4 $(b)(d)$ plots the cortical responses during Run_3, where the continuous alpha activation is observed for the run duration. In the spectrogram, the alpha activation is enhanced with an intensity range of $0.7\,\text{pT/Hz}^{1/2}$ to$1\,\text{pT/Hz}^{1/2}$. Similar activation patterns are prompt in the linear density, with a maximum peak of $\sim 0.7\,\text{pT/Hz}$ at $9.7\,\text{Hz}$.

Figure 4.5 demonstrates the sensitivity of the modular OPM during a $60\,\text{s}$ measurement. Two sensor modules separately measured the noise floor inside the four-layer MSC. The recordings were individually analysed as sensor modules and then as a gradiometer by taking the difference between the module traces (yellow trace). The noise floor for module 1 was measured as $65\,\text{fT}/\sqrt{\text{Hz}}$ and for module 2 was $83\,\text{fT}/\sqrt{\text{Hz}}$ for the frequency range of $5\,\text{Hz}$ to $45\,\text{Hz}$. The bandwidths of the two modules were $213\,\text{Hz}$ and $219\,\text{Hz}$, respectively.

The sensitivity of the gradiometer configuration was significantly increased compared to the two separate modules, with a noise-floor of $47\,\text{fT}/\sqrt{\text{Hz}}$. The sensitivity improvement was a product of the common light intensity noise used in both module sensors.

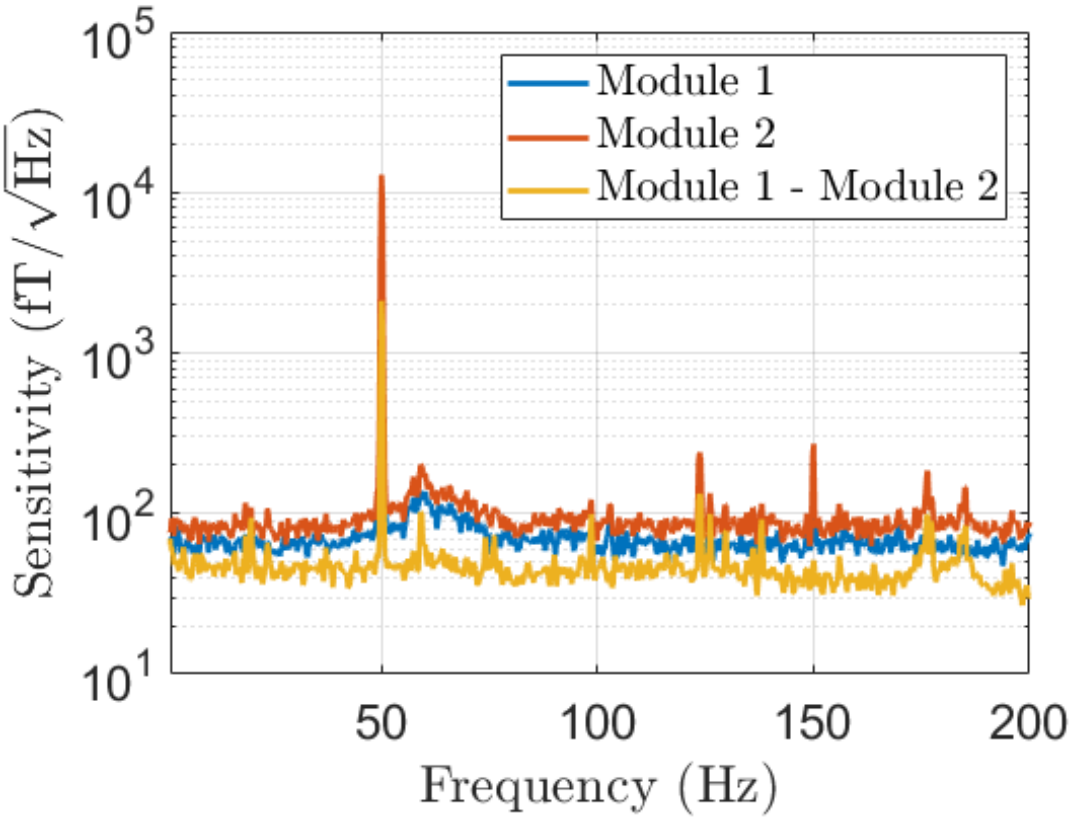

Figure 4.5: Sensitivity measurement of the single-axis modular ^{87}Rb OPM between 0 Hz to 200 Hz. Sensor Module 1 (blue) and Module 2 (red) have a noise floor of 65 fT/$\sqrt{\text{Hz}}$ and 83 fT/$\sqrt{\text{Hz}}$, respectively. As a gradiometer (Module 1 - Module 2), the noise floor is reduced to 47 fT/$\sqrt{\text{Hz}}$. Noise reduction at 50 Hz is shown for the gradiometer configuration.

4.4 Discussion

This chapter briefly introduced the newly developed ^{87}Rb modular OPM and showed the suitability for neurophysiological measurements. The enhanced performance of the sensor combined with the malleable configuration could lead to a novel integrated OPM gradiometer array, with reduced noise and improve sensitivity.

The recent emergence of OPM technology has led to the development of various OPM sensors with various configuration, sizes or vapour cells, which aim to surpass the limitations of the currently available systems. Similarly, the ^{87}Rb modular OPM emphasises the modularity and scalability of the system. Having individual OPM sensors is efficient when targeting one particular cortical area, but there are limitations for simultaneous use of multiple OPM sensors. Cross-talk between the closely

placed OPMs affect the already sensitive measurements, with additional noise introduced into the individual channels. The increased temperatures of sensor heads are inconvenient in a low density OPM-MEG system, hence an increased number of sensors could be uncomfortable or damaging for the cortical area.

The modular OPM consists of three different parts; the light source, the sensor and the beam distribution. A multi-axis modular OPM system is easy to construct, just by adding the desirable number of sensor modules one needs in the system. The light source and beam configuration modules remain common for all the sensor modules. All the optical elements inside the sensor module can be replaced or re-configured for different measurements. The modular OPM vapour cell is heated at a lower temperature ($\sim$130 °C) than the one used for other ^{87}Rb OPMs ($\sim$150 °C). This allows the placement of the sensor directly on the scalp or skin, with significantly reduced – or none – standoff distance, as thermal insulation is not required. The enhanced adaptability of the sensor is also presented in the results section, where two different configurations were used; the single-axis magnetometer was used in the alpha rhythm study and the single-axis gradiometer was used in the sensitivity measurement. For the neurophysiological measurements the single-axis modular sensor was adequate for alpha wave measurements while by using the dual-axis configuration in sensitivity measurements, the reduced noise of the gradiometer system reflects the potential reduced noise of a multi-axis modular OPM system.

As a proof of principle, alpha brain rhythms were measured in two participants using the single sensor configuration of the modular OPM. Clear responses were recorded in both participants during the open-close eyes paradigm (Run_1). Additional measurements of only opened (Run_2) or closed (Run_3) eyes were obtained for Participant 1, further validating the alpha brain wave recording using the modular OPM.

The potential of a multi-axis modular OPM with increased bandwidth and significantly reduced noise could lead to new neurophysiological measurements not possible with previous neuroimaging sensors. Modulating the configuration of a sensor array according to the experimental needs could lead to measuring targeted neuronal regions otherwise challenging to measuring using other neuroimaging methods. In addition to the modularity emphasis, the broader bandwidth of the sensor

makes it ideal for neuronal activation tracking across the peripheral nervous system. Importantly, a high density modular OPM array, with limited noise and improved sensitivity, would improve the source localization, i.e. inverse problem. Moreover, placing the same sensors across different neuronal areas with different configuration and broader bandwidth is a unique feature of the multi-axis modular OPM.

Chapter 5

Spinal cord measurements

The reduced noise and the high bandwidth of the modular optically pumped magnetometer (OPM) described in Chapter 4 makes it ideal candidate for a sensitive neuroimaging system, suitable for high frequency signal recordings. Following the proof-of principle alpha rhythm study, we created a synthetic signal to test the suitability of the modular OPM and the QuSpin OPM for spinal cord imaging.

We hypothesized the modular OPM and QuSpin OPM could measure spinal evoked responses due to the suppressed noise-floor and improved spatiotemporal resolution. First, this hypothesis was addressed using physical simulations, which confirmed that both the QuSPin and the modular OPM should be able to detect the high frequency signal typically observed in the spinal cord. These results verify the suitability of modular OPM and QuSpin for spinal cord measurements. Next, we performed in-vivo measurements, using the QuSpin sensors only. Two different paradigms were used, measuring cervical and tibial spinal cord evoked responses in 6 different participants. The in-vivo results indicated that spinal cord imaging using QuSpin sensors is possible. We note the measurements were limited by the stimulation artifacts, and were compared to phantom measurements to determine the validity of our hypothesis.

This is the first time, to date, a non-invasive neuroimaging method records simultaneously cortical and spine evoked responses using the OPM systems.

The experimental protocol and methodology of the synthetic spine signal measurements and the in-vivo measurements cortical measurements in this chapter were conceived and designed by the author with assistance from Christopher Abel for

the former. In the simulation study, the modular OPM and and the data acquisition hardware and software were set-up and calibrated by Thomas Coussens with assistance from the author. The commercially available OPM was calibrated and set-up by the author. The modular OPM data were taken by Thomas Coussens with assistance from the author and the QuSpin OPM data were taken by the author. All the analysis was performed mainly by the author, with assistance from Thomas Coussens and Tim M. James. The metric of the required noise floor for high frequency signals R was conceived by the author with assistance from Thomas Coussens. In the in-vivo study, the OPM sensors and the DAQ hardware and software were set-up and calibrated by the author with assistance from Thomas Coussens. The participant's motor threshold was identified solely by the author. The sensors over the spinal cord and the cortex were placed by the author. All the measurements were taken mainly by the author, with assistance of Tim M. James. All analysis and results interpretation were performed solely by the author.

5.1 Introduction

The spinal cord is a part of the central nervous system (CNS) connecting the peripheral neurons to the brain (55). Understanding this network is essential to fully grasp the functional and structural connectivity of the CNS. The characterisation and evaluation of the healthy and pathological spinal cord could be crucial for the identification of neurodegenerative disorders (127; 128). Recent technological advances in neuroimaging allowed for a better understanding of the functional brain (49) and spine (34). Measuring the spinal response is challenging and requires a imaging system with high SnR and spatio-temporal resolution. Different from the cortical biomagnetic signals, spinal cord activations might induce high frequency signals ($\sim 1200\,\mathrm{Hz}$) (91; 92), arising from deeper neuronal sources with average skin-to-subarachnoid distance of $\sim 5.5\,\mathrm{cm}$ (129). The characterisation and evaluation of the functional spinal cord is measured by invasive and non-invasive neuroimagnig methods, with the former method being preferred (69).

For the anatomical evaluation of the spinal cord, non-invasive structural imaging methods can be used, such as MRI (67). These methods can provide detailed

images of the spinal structure, and any injuries, lesions or any other impairments of the spine can be identified. Measuring the spinal cord function is more challenging: the methods that provide high signal-to-noise ratio (SnR) and spatio-temporal resolution are typically invasive (130; 131), although non-invasive methods such as EEG electrodes can be placed along the targeted spinal cord segment and the brain and used to record the evoked responses (132). In recent studies, modified SQUID sensors were used to successfully measure the evoked magnetic fields of the spine in response to peripheral electric stimulation (133; 134). FMRI spinal cord imaging was utilised to further explore the synchronization and connectivity of the cortical and spinal responses, where task-based (135) and resting-state were both examined (136).

Since the 1970s, researchers were puzzled about the benefits of the epidural electrodes over non-invasive EEG electrodes. The main differences between the two methods were confirmed by a study in 1980 (137). The researchers used both surface and epidural electrodes to test the suitability of the methods in functional spinal imaging. Spinal activations in response to a peripheral neuronal stimulation showed the epidural electrode measured a more detailed evoked response compare to the surface electrode. Since then, a plethora of studies used epidural electrodes in various spinal cord segments aiming to fully characterise the spinal response (138; 69; 139; 140).

Functional spinal imaging is essential for understanding the healthy and clinical spinal response. Intraoperative spinal monitoring is a neuroimaging method using catheter epidural electrodes to evaluate the spinal cord evoked responses during spine surgery and to warn the surgeon of any impairment, such as spine ischemia or compression (132).Understanding healthy spinal cord responses could lead to quicker evaluation of the clinical populations. Spinal cord studies tried to evaluate the evoked responses in people diagnosed with multiple sclerosis (MS) (141), spinal cord injury (SCI) (137) and other spinal impairments aiming to evaluate the differences between clinical and healthy control populations (138). The full description and characterization of the healthy and clinical evoked responses in human spinal cord could lead to early identification of functional deficiencies and distinguish novel biomarkers for clinical applications.

Limitations of the current spinal cord neuroimaging methods make spinal cord research challenging (142; 143). The non-invasive EEG electrodes have low SnR and spatial resolution (137), while the catheter epidural electrodes requires a surgical operation for the correct placement. The SQUID sensors revealed promising results but the designed system is not commercially available. Similar restrictions are found using fMRI spinal imaging, with limited temporal resolution and motion artifacts (144).

Here, I introduce a possible novel method for spinal cord imaging using OPM sensors. Simultaneous recordings of the human brain and spine biomagnetic measurements showed the suitability of the system for spinal measurements. First, a simulation study showed the suitability of two different types of OPM sensors for spinal recordings: the newly built modular OPM sensor and the commercially available OPM. Due to the increased bandwidth, the former measured more accurately the spinal reference signal compared to the latter. Both sensors were shown to be suitable for spinal cord measurements. The in-vivo spinal cord measurements of six healthy participants further validate the OPM system as a spinal imaging method using commercial OPMs.

5.2 Synthetic spine signal measurement

Although cortical measurements using OPMs have shown the enhanced performance of the sensors and offered novel experimental set-ups and studies, OPMs have not yet been used for spinal cord measurements.

This simulation study tests the suitability of the modular OPM and QuSpin OPM for spinal cord imaging using a synthetic spinal signal measurement as a reference signal. The results suggest both OPM sensors can be used for spinal cord imaging, even though the QuSpin is limited by its bandwidth.

5.2.1 Methods and Analysis

A first-generation QuSpin zero-field magnetometers (QuSpin Inc., Louisville, CO, USA) and the newly developed modular OPM were used to measure a reference spinal cord signal (see Chapter 4). The reference signal was extracted from the

study "Visualization of electrical activity in the cervical spinal cord and nerve roots after ulnar nerve stimulation using magnetospinography", from *figure* 3 in (34). Webplotdigitizer [1], an open-source tool, was used to extract the selected signal. The reference signal is an averaged spinal evoked field recorded by a SQUID part forming part of a 44 SQUID array. The dimensions of the SQUID array were 180 mm×130 mm. The array was placed over the cervical spine, covering the area between the C4 and T2 spine. As the synthetic signal was extracted from a printed source, the sampling frequency was lower than the original (40 kHz). We used a linear interpolation method to convert the reconstructed signal to the original form.

The formula for linear interpolation of a data signal is:

$$y(n) = \sum_{n=1}^{\infty} y_n \prod_{n=1}^{\infty} \frac{y_{n+1} - y_n}{x_{n+1} - x_n} * (x(n) - x_n) \tag{5.1}$$

where x, y describe the interpolated signal, x_n and y_n are the data points of the extracted signal, and n is the range of the data set.

Simulation

Two independent measurements were taken in the small four layer μ-metal cylinder (MS-2 mu-metal shield, Twinleaf LLC), using the QuSpin and the modular OPM. The OPM sensor heads were placed in the centre of the magnetically shielded cylinder (MSC) and the OPM electronics were located outside the MSC. Each sensor head was mounted in a 3D printed holder in the centre of the MSC, designed to constrain the sensors, avoiding any movements during the measurements. Prior to each measurement, the correct operation of the sensors and the noise floor were tested.

To generate the reference signal , a python-based software was developed and directly connected to a Labjack T7 Pro device (Labjack Corporation, Co, USA), denoted here as $stream - out$ Labjack. The signal was delivered into the MSC through the z-axis coils of the MS-2u Twinleaf (CSBA, Twinleaf) current supply. The same delivery system was used for both OPM measurements.

The data acquisition system (DAQ) system utilized an additional LabJack T7 Pro (*Save Data*), with sampling frequency 40 kHz, which was connected to the

[1] www.automeris.io/WebPlotDigitizer/

stream − out LabJack and directly recorded the TTL pulse,which indicated the stimulation onset. The python software was directly connected and synchronized with the DAQ system. The QuSpin DAQ system used the digital output of the QuSpin which was connected to the *SaveData* LabJack and then fed to a separate computer. The modular OPM system used the *DAQ* LabJack to record the analog output of the lock-in amplifier (LIA) (SR865A, Stanford Research Systems) (figure 5.1).

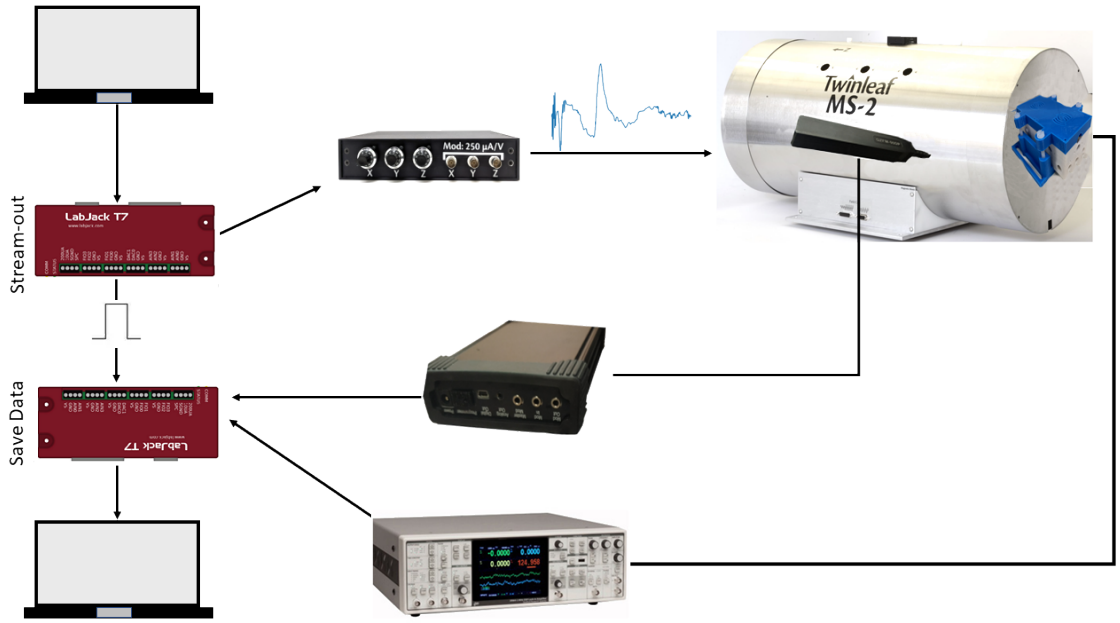

Figure 5.1: Experimental set-up of simulation study. The PC is connected to *Stream − out* LabJack, which delivers the reference signal (blue trace) into the MSC via the MS current supply. The TTL pulse (black square trace) is fed into *DAQ* Labjack, which records the digital output of the QuSpin, during the QuSpin measurements and the analogue output of the LIA during the modular OPM measurements. *Save data* stored all the data to a PC.

The duration of the QuSpin and modular OPM measurements were 120 s. To reduce the electronic noise interference and the reference modulation, two bandstop filters were applied prior to the averaging, between 40 Hz and 60 Hz and between 900 Hz and 950 Hz, respectively. A TTL pulse indicated the onset of the reference signal during the measurement. The trials were from 0 ms to 25 ms. The time-locked averaged recording included at least 66 trials. The averaged recorded signals were compared to the reference signal. The same filters and averaging method were used

for both OPM measurements.

Frequency response

In addition to the synthetic signal, the frequency response of the QuSpin sensor was recorded. A signal generator was connected to the MSC, where either the modular OPM or the QuSpin OPM recorded the signal. The signal generator ranged between 1 Hz and 1 kHz with a 60 s duration each.

In addition to the QuSpin frequency response, the QuSpin calibrated and uncalibrated response was measured. First, the frequency response was reconstructed using the extrapolation method to the length of the recorded signal. As a recorded signal we used the background measurement of the MSR used in the in-vivo study, recorded by a 2nd generation QuSpin.

Based on the QuSpin frequency response, we determined the ratio (R) of a recorded signal over the frequency response. The ratio (R) indicates the required noise floor for the in-vivo spinal cord measurements and is described as:

$$R = \frac{BG}{F} \tag{5.2}$$

where R is the ratio, BG is the spectral density of the background measurement, and F is the extrapolated frequency response.

5.2.2 Results & conclusion

The simulation results showed the reference signal was recorded by both sensors, modular OPM and QuSpin. The recorded signals had similar patterns to the reference signal with different time onsets.

Figure 5.2 showed the reference signal (orange) and the ^{87}Rb modular OPM signal (blue). The traces had similar patterns in amplitude and time. The inset focused at the signal between 240 ms and 280 ms, where a delay (τ_{mod}) of 0.8 ms was observed. The time delays were measured as the difference between the peak onset of the local maxima in the given period. QuSpin results were plotted in figure 5.3. The averaged reference signal (orange) and the QuSpin averaged recording (blue trace) followed the same activation pattern. The inset showed the traces onset between 240 ms and 280 ms, with a longer delayed onset (τ_{QS}) of $\sim$ 4 ms compared to τ_{mod}.

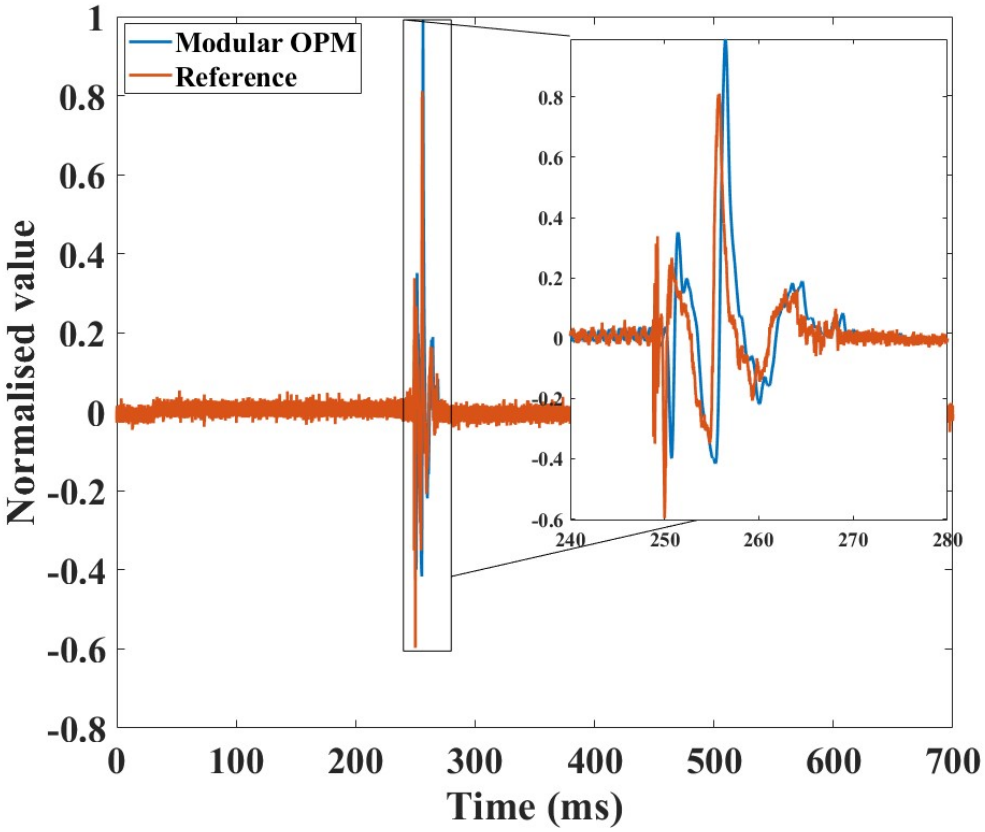

Figure 5.2: ^{87}Rb Modular OPM measurement of the reference signal. The averaged modular OPM recording (blue) compared to the averaged reference signal (orange). *Inset*: The reference and modular OPM trace between 24 ms and 28 ms.

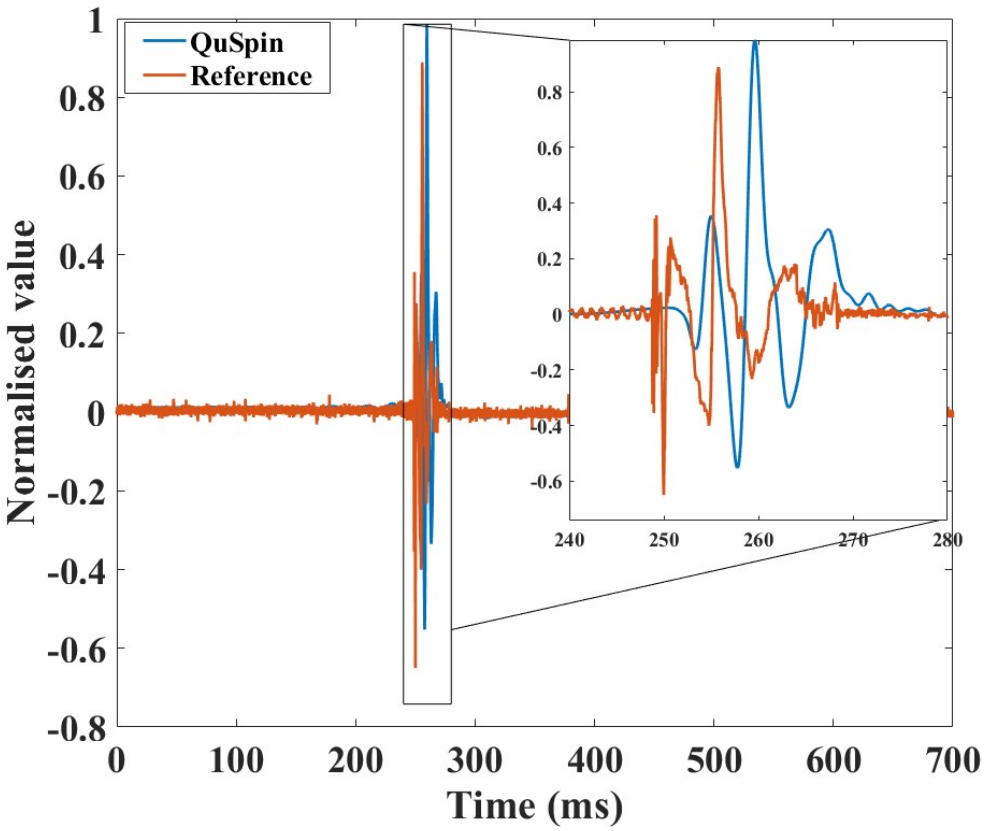

Figure 5.3: QuSpin measurement of the reference signal. QuSpin averaged recording (blue) compared to the averaged reference signal (orange). *Inset*: The reference and QuSpin trace between 24 ms and 28 ms.

The measurements indicated modular OPM and QuSpin OPM were suitable for high frequency signal recordings. The onset delay between the reference signal and the recorded signal was observed for both sensors (see figure 5.2, 5.3), but the delay τ_{mod} was $\sim$ 5 times shorter compared to τ_{SQ}. The increased τ_{SQ} could arise from the harsh cut-off filter and the limited bandwidth of the sensor. The 500 Hz filter was observed in the frequency response measurements (figure 5.4).

Since QuSpin sensors were chosen to be used in the in-vivo study, the frequency response was measured to test the performance of the sensor for signals with frequency components greater than the sensor bandwidth. The signal attenuation for frequencies beyond the sensor's bandwidth led to noise floor estimation of the calibrated response over the recorded signal. The noise floor scales with the signal frequency (see table 5.1 and figure 5.6).

Figure 5.4 shows the normalised frequency response of a QuSpin OPM from

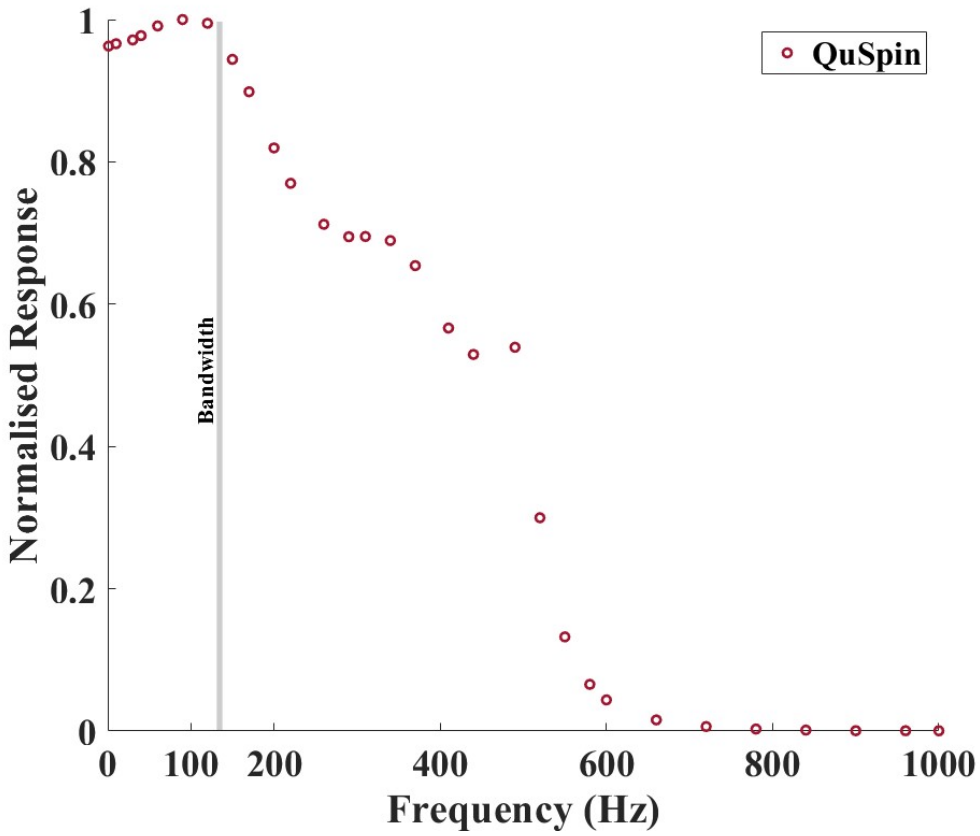

Figure 5.4: Frequency response of the 1st generation QuSpin between 1 Hz and 1 kHz. The response for signals higher than 600 hertz is close to zero. The gray ribbon indicates the bandwidth of the sensor at 135 Hz (47)

1 Hz to 1 kHz. Up to the bandwidth frequency (135 Hz) the amplitude of the input signal is largely unchanged, with a 4 % attenuation at 1 Hz. Beyond the bandwidth frequency, the signal is attenuated approximately linearly until a cutoff frequency of 500 Hz beyond which there is an attenuation > 70 %.

For direct bandwidth comparison, figure 5.5 plots the frequency response of the gradiometer configuration of the modular OPM between 1 Hz and 320 Hz. The blue x markings and the red *star* markings correspond to the sensor module 1 and the sensor module 2 frequency response, respectively. The bandwidth of the modular OPM sensor is defined as the frequency where there is a $1/\sqrt{2}$ reduction in the measured amplitude. Hence, the bandwidth is measured as 213 Hz and 219 Hz, for the sensor module 1 and the sensor module 2, respectively (53). Thus, the grey ribbon in the plot illustrates the bandwidth of both modules at $\sim$ 217 Hz. Although the frequency responses measured by sensor module 1 and sensor module 2 are not

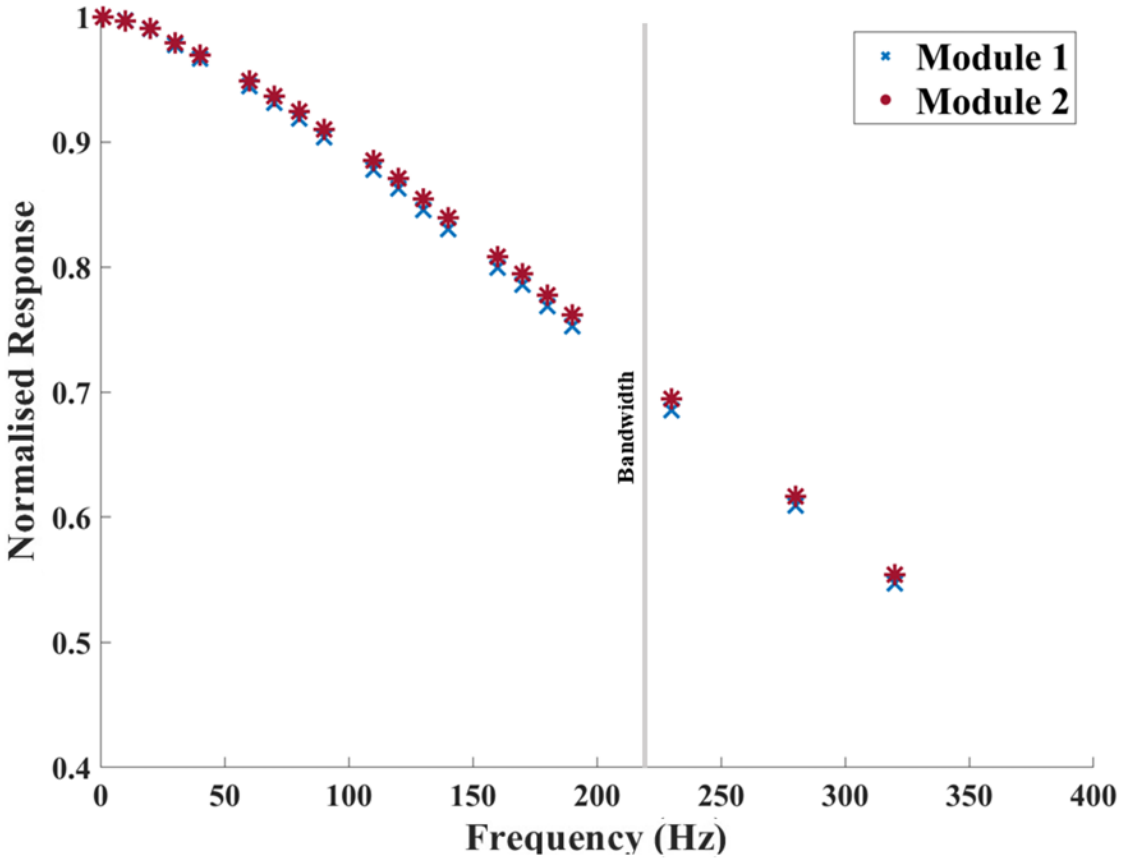

Figure 5.5: Frequency response of the gradiometer modular OPM between 1 Hz and 320 Hz. The blue and red markers correspond to the frequency respond recorded by the sensor module 1 and the sensor module 2 respectively.The gray ribbon indicates the bandwidth of the modules at $\sim$ 217 Hz (53).

identical, the difference between the measurements is less than 1.4 %.

Although the bandwidth of the QuSpin sensor at 135 Hz is a value provided by the QuSpin company (47), this value does not correspond to the standard bandwidth definition of $1/\sqrt{2}$ signal reduction, which was used to define the modular OPM bandwidth. Following the same bandwidth definition as the modular OPM, QuSpin's bandwidth can be measured from the figure 5.4 as $\sim$250 Hz.

Figure 5.6 plots the calibrated R and the uncalibrated response BG of the QuSpin sensor. Up to the bandwidth frequency of the sensor (135 Hz), the noise floor for R and BG is similar 26.5(8) fT/Hz$^{1/2}$, with the bracketed value the standard deviation. A linearly increasing noise floor is observed in R from 140 Hz to 500 Hz, while BG response remains steady. Beyond the 500 Hz cut-off frequency, the noise floor of R

rapidly expands to 42(28) $\mathrm{fT/Hz^{1/2}}$) but the BG noise floor drops to 11(9) $\mathrm{fT/Hz^{1/2}}$) and beyond 600 Hz had no response. Noise floor measurements were taken for signals with frequency below the sensor's bandwidth , between the bandwidth and the 500 Hz cut-off frequency and frequencies over the cut-off. The noise-floor requirements for different frequencies of BG and R are shown in table 5.1.

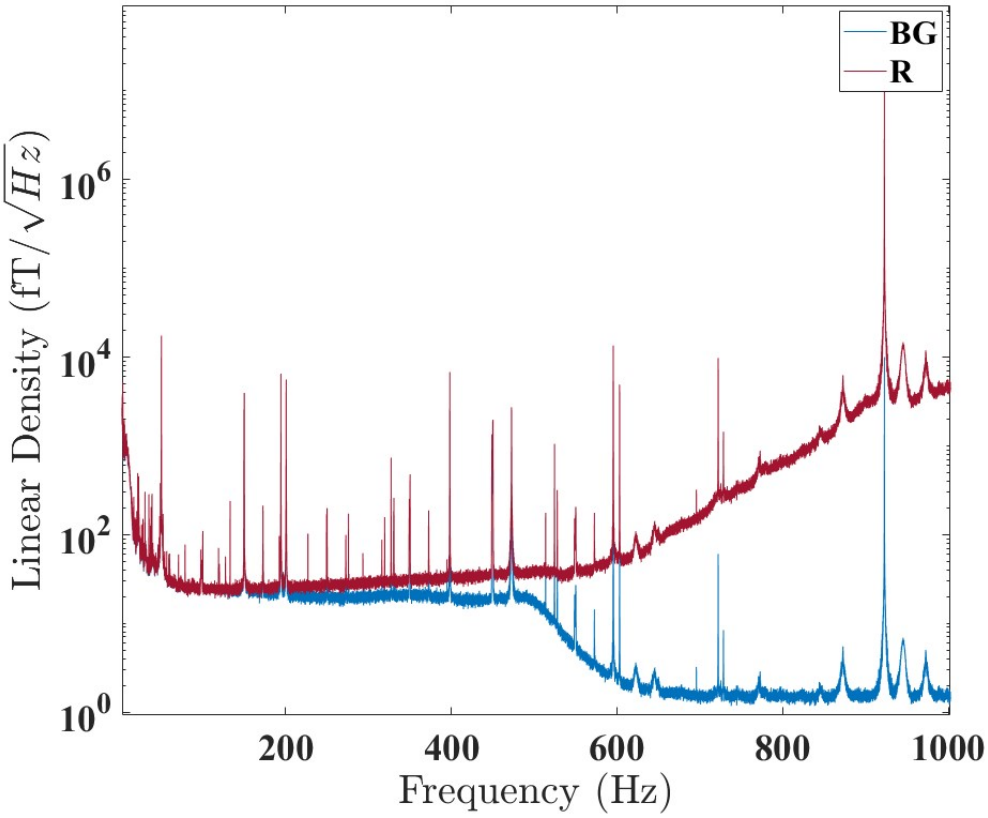

Figure 5.6: Spectral density of the empty MSR measurement BG (blue trace) and the ratio R of the measurement to the frequency response (red trace) from 1 Hz to 1 kHz. The BG response is the uncalibrated response of the QuSpin sensor for signals at higher frequencies. The R response indicates the required noise-floor for higher frequency signals.

For the in-vivo experiment and result analysis the findings of the simulation were taken into consideration, with the τ_{SQ} and the R noise floor measurements providing more accurate estimation of the spinal evoked fields.

Noise floor (Hz)	BG (fT/Hz$^{1/2}$)	R (fT/Hz$^{1/2}$))
Frequency $\leq$135 Hz	26.5(8)	26.5 (8)
135 Hz$\leq$Frequency$>$500 Hz	18.6(1)	33.6(2)
Frequency$\geq$500 kHz	11(9)	42(28)

Table 5.1: Noise floor measurement for the BG signal and the R calibrated signal. The bracketed values are the standard deviation.

5.3 In-vivo spinal cord measurement

Based on the simulation results, we designed an in-vivo study using OPM sensors to simultaneously record spinal cord evoked fields and somatosensory evoked fields. Two peripheral nerve stimuli were used to evaluate the OPM spinal imaging method.

5.3.1 Participants

Spinal cord evoked fields (SCEF) and somatosensory evoked fields (SEF) were measured in six healthy participants (2 women, 4 men, mean age 35). Participants gave written informed consent to take part, after explanation of the procedure and purpose of the experiment. Participant 5 was left handed, stimulus and cortical sensors were placed on the right side. Each participant took part in one median nerve stimulation (MN) run and one tibial nerve stimulation (TN) run.

5.3.2 Experimental design

The study was approved by the Cardiff University Ethics Committee (1637535620-3375) and was conducted in accordance with the Declaration of Helsinki Ethical Principles. The OPM-MEG measurements were taken in the MSR at the Centre for Human Developmental Science (CUCHDS). The field fluctuations of the MSR were below 40 nT, within the operation of the QuSpin magnetometer (109; 52).

Two spinal cord electric stimulation paradigms were used; the median nerve stimulus (MN) and the tibial nerve stimulus (TN). These stimuli are widely used to evaluate conduction of the peripheral nerve, spinal and cortical regions (32). The electric stimulation parameters were based on general guidelines for somatosensory evoked potentials and on recent magnetospinography study (32; 34; 145). Both

stimuli consisted of 3-5 Hz electric pulses, with pulse duration of 300 µs. A pseudo-randomised 0.5 ms jitter was introduced between the pulses to all the runs. The pulse intensity was selected for each participant to match their motor threshold (see table 5.2). A single MN or TN run had a total duration of 30 min and consisted of $\sim$ 7800 trials. Each trial was 200 ms long. Electrodes were connected to a high voltage current stimulator (DS7A, Digitimer Ltd.) to generate and deliver the electric stimulation to the participants. For the MN, two disc electrodes were placed on the median nerve at the level of the right wrist. The anode electrode had at least 3 cm distance to the cathode electrode. The intensity of the electric pulses was tested prior to each run, by ensuring that they generated a constant thumb tremble. For the TN, two disc electrodes were placed over the posterior tibial nerve, at the level of the right ankle. The distance between the anode and the cathode electrode was $\sim$ 3 cm, with the cathode placed between the Achilles tendon and the posterior malleolus (145)(32). Similar to the MN run, prior to each measurement the electric pulse intensity was tested, aiming for a 2-3 cm constant toe flexion (145)(32).

The OPM system consisted of ten second generation QuSpin magnetometers (QuSpin Inc., Louisville, CO, USA). Six QuSpins were used for the spinal cord records, three for the cortical recordings and one was used as a reference for the TN runs. The spinal sensors were mounted in a 3D printed 2 x 3 array, (50 mm $\times$ 80 mm). The cortical sensors were mounted on a MEG Cap (QuSpin Inc., Louisville, CO, USA) and placed over the primary somatosensory cortex (C3) and parietal lobe (CP3 and P3) according to the 10-10 system (111) (figure 5.7 $(a)(d)$). During the MN run, the spinal sensors were placed over the cervical spine. Participants were asked to flex their neck to identify the C7 vertebra (67). The array was placed at C7 and covered the cervical spine up to the C3 vertebra 5.7 (a)) In the TN run, the sensor array was placed on the lower back over the lumbar spine, covering the L4 to T12 vertebrae (figure. 5.7 (d)). In some of the runs, an additional QuSpin sensor was placed at the cervical spine as reference. A QuSpin malfunction led to limited runs with the reference sensor. Only Participant 1, Participant 4, and Participant 5 had TN run with the additional sensor.

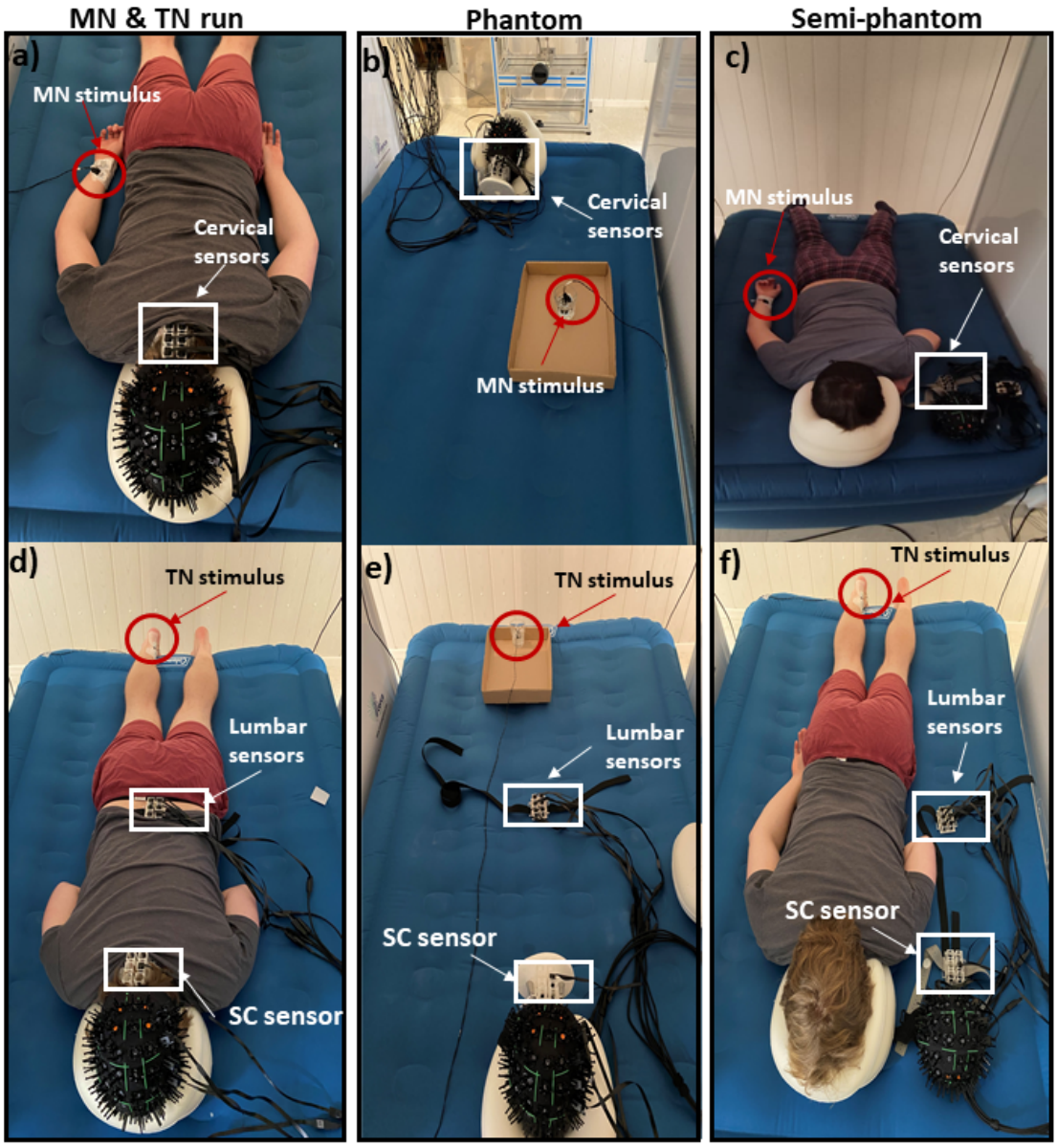

Figure 5.7: Experimental set-up for OPM spinal cord and cortical recordings. *Top row*: Median nerve (MN) stimulus in three different runs. (a) MN run: stimulation and sensors placed on the participant. (b) MN Phantom: stimulation and sensors were placed on the air-mattress and dummy head (c) MN semi-phantom: stimulation attached to the participant, senors placed on the air-mattress. *Bottom row*: Tibial nerve stimulation (TN) in three different runs. (d) TN run: stimulation and sensors placed on the participant. (e) TN phantom: stimulation and sensors were placed on the air-mattress and the dummy head: (f) TN semi-phantom: stimulation attached to the participant, sensors placed on the air-mattress.

Before the measurement, the participant was asked to test the MN or TN stimulation to define the required pulse intensity level above the motor threshold. The participant with the electrodes attached was instructed to lay prone on the air-mattress placed in the middle of the MSR. The head was supported by a neck pillow, placed in the middle of the air mattress (see figure5.7). The neck pillow allowed flexion of the cervical spine while comfortable positioning the participant for long duration runs. Before the experimental run, a test for the proper operation of the stimuli was done. Prior to each run, the QuSpin sensors measured a 120 s spinal and cortical baseline in absence of stimulation. For the MN run, the participants were instructed to extend the right hand to the right side to increase the distance of the stimulation from the sensors. Similarly, for the TN run the participants were asked to place their stimulated foot to the right. During MN and TN runs, the participants were instructed to maintain their position and stay as still as possible.

Phantom measurements and empty MSR measurements were obtained in order to evaluate the noise level and the artifacts from the electric stimulation. The phantom measurements consisted of three different set-ups;

- *MN* or *TN phantom* run: Stimulation and OPMs on the air-mattress 5.7(b)(d))
- *MN* or *TN Semi-phantom*: Stimulation on participant, OPMs on the air-mattress (c)(f)
- *Side-sensor phantom*: Stimulation on participant, sensors next to lumbar spine.

For the phantom runs, the electrodes were placed in a salted glass of water to achieve the required conductivity ($\sim 2\,\mathrm{k}\Omega$). The phantom measurements were taken in an empty MSR. The cortical sensors were placed at the MEG Cap on a dummy head. For the MN phantom, the spinal sensors were placed 12 cm below the dummy's head, wrapped around the dummy's neck. The glass of water was placed 30 cm to the right of the dummy and 60 cm away, achieving similar position and distance to the experimental runs (figure 5.7 (*b*)). For the TN phantom, similar sensor placement to the experimental runs was achieved by placing the spine sensors ~ 80 cm under the cortical sensors with a ~ 90 cm distance to the electrodes (figure5.7 (*e*)).

Two MN and TN phantom runs were recorded. For the first MN and TN phantom run, the electric stimuli had 18 mA intensity and the second had 99 mA intensity. The duration of the first MN and TN phantom runs were 300 s and the second 30 min.

Participant	Median nerve (MN) mA	Tibial nerve (TN) mA
Participant 1	5.5	17.0, 35.0
Participant 2	7.0	12.0
Participant 3	8.0	8.5
Participant 4	7.5	12.0
Participant 5	8.0	14.0
Participant 6	7.5	12.0
Phantom 1	5.5	7.5
Phantom 2	99.9	99.9
Semi-Phantom	7.0	18.0
Side-sensor Phantom	-	12

Table 5.2: Electric pulse intensity for the MN/TN, the phantom and semi-phantom runs.

All the semi-phantom runs were recorded with a participant positioned as in the MN and TN runs, measuring the movement and stimuli artifacts combined. The set-up of the semi-phantom runs were similar to the phantom runs. The electrodes were positioned according to the used paradigm, but the sensors were placed next to the laying participant. The cortical sensors were mounted on the MEG cap and placed 5 cm next to participants head. For the MN semi-phantom OPM, the spine sensors were placed 5 cm next to participant's cervical spine, while for the TN semi-phantom OPM the spine sensors were placed 5 cm next to participants lumbar spine. Based on the semi-phantom OPM measurements, the noise floor of the MSR room and the stimulation artifacts were better determined. The MN semi-phantom run was recorded for Participant 2 prior to the MN run, using the same stimulation intensity of 7 mA. The TN semi-phantom run was recorded for Participant 3 prior to the TN run, maintaining the stimulus intensity at 18 mA. The side-sensor phantom was a 300 s measurement of Participant 2 and the set-up was similar to the semi-phantom

OPM TN. The stimulation was over the participants tibial nerve, the cortical sensors were placed over the head and the spinal sensors were placed 6 cm at the left side of the lumbar spine. During all the phantom run, the QuSpin sensors had the same orientation as in MN and TN run.

5.3.3 Data analysis

A MATLAB based script was directly connected and synchronized with a main OPM data acquisition system (DAQ). QuSpin's analogue outputs and stimulator's TTL pulse were recorded at 7.8 kHz via a NI-9205 DAQ unit (National Instruments, Corp). All DAQ and QuSpin electronics and the stimulator were located outside the MSR and connected to the NI-9205 and control computer. The QuSpin sensor heads and the non-magnetic disc electrodes were connected to the main units but placed inside the MSR.

OPM data analyses were performed using the FieldTrip toolbox (112) and MATLAB. In order to isolate the frequencies of interest with relevance in somatosensory evoked fields and spinal cord fields, the cortical and the spinal measurements were separately analysed.

Cortical measurements

For the cortical measurements, the data were filtered with a bandpass filter between 5 Hz and 60 Hz and a first order bandstop filter was applied between 49 and 51 Hz to suppress 50 Hz line-noise. The trials for MN and TN stimulation were 0 to 200 ms. The somatosensory evoked fields (SEFs) were measured as the averaged of the $\sim$ 7000 trials. Any interrupted experimental runs were removed from the analysis.

The characteristics of the SEF differ for the MN and TN stimuli (32). MN SEF are characterised by an early positive or negative peak at 20 ms (P20) followed by a second component between 40 ms and 50 ms (P50) (146; 147). The P50 is not always observed and highly depends on the sensor placement and the stimulus intensity (148). SEF for right posterior TN are characterised by two components, a peak at 45 ms (P45) followed by a response at 110 ms (P110) (32; 149).

The cortical responses were measured in radial (SEF_z) and axial (SEF_y) directions. The SEF_y did not show any characteristic component or patterns and was not

included in the result section nor the analysis. For the SEF_z component analysis, the onset of the component is determined as the time of the pulse's local maxima between the two local minima adjacent to a pulse's maximum signal value.

The reproducibility for the cortical measurements was calculated as the mean coefficient correlation across participants for the C3 sensor. The uncertainty of the measurements was calculated as the 95% confidence interval for the spinal and cortical results.

Spinal cord measurements

A first order bandpass filter between 3 Hz and 3000 Hz was applied to the spinal cord measurements (32). The spinal trials were 0 to 30 ms. Any interrupted trials or recordings were removed from the analysis. The spinal averaged evoked fields (SCEF) were measured as the average across the $\sim$ 7800 trials.

The QuSpin simulation showed the recorded signal had a 4 ms time lag. In the analysis the time lag was removed to show the results with accurate temporal resolution. Hence, the averaged spinal cord evoked fields (SCEF) were -4 ms to 26 ms. OPMs can measure simultaneously the radial spinal cord evoked field ($SCEF_z$) and the axial spinal cord evoked field ($SCEF_y$). The same analysis methods was applied to both, radial (z) and axial (y) recordings.

In order to evaluate the spinal cord recordings, and distinguish the SCEF from the stimulation artifacts, we compared the MN and TN run to the corresponding phantom and semi-phantom runs. The grand averaged spinal cord evoked fields (GASCEF) are shown as the mean across all sensors' averaged evoked fields (figure 5.11). The standard error shows the uncertainty of the measurement at each time point, with a 0.13 ms time spacing. A sensor-to-sensor comparison is shown for signals in Fourier space between the MN or TN to the phantom or semi-phantom runs (figure 5.12, 5.14. The signals were unfiltered and compared for frequencies between 1 Hz and 50 Hz.

Spinal cord responses are not as well characterised as the cortical responses. A characteristic early peak followed by a wave pattern similar to the M letter was observed for MN and TN spinal responses. The onset times of the spinal components largely differ between studies. For the MN SCEF the component M onset is at

∼4 ms (37) or at ∼10 ms (34) and for the TN SCEF component M onset is at ∼6 ms (130; 69), ∼10 ms (36) or ∼15 ms (35). The great variability of the component onset might be the result of different imaging systems, stimulation parameters and analysis methods.

For the reproducibility between participants in spinal cord recordings, we measured the Pearson coefficient correlation of the GASCEF of each participant (+1 correlated signals, 0 no correlation, -1 anti-correlated signals).

For the component characterization and analysis, the component onset was determined as the the pulse's local maximum closest to the known component onset, i.e. the P20 onset is determined as the time of the well-defined local maximum closest to 20 ms after the stimulus. The mean onset and signal amplitude across the sensors and the standard error indicates the variability of the onset time for each measurement. The uncertainty of the measurements were calculated as the 95% confidence interval for the spinal and cortical results.

5.3.4 Results

The SCEF from all participants were consistent with pattern known from recent studies (37) or studies using catheter epidural electrodes (69; 138).

A characteristic peak at ∼4 ms followed by a polyphasic wave, similar to the letter M, were observed in MN and TN runs. The QuSpin simulation study showed a 4 ms time lag (τ_{SQ}) and the increased noise floor (R) for high-frequency signal measurement. Figure 5.8 showed Participant's 1 SCEF for (a)(b) the MN run, (c) a 17 mA TN and (d) 35 mA TN run. In the figure 5.8 (a), a peak onset was measured at 4 ms with amplitude of ∼ 16 pT, followed by a M wave pattern. This peak was observed in all the runs. In the phantom and semi-phantom runs, the time onset of the peak was the similar to the MN, TN runs at 4(1) ms. The exact onset in all the runs indicated the peak might be an artifact product, probably produced by the electric stimulation. Figure 5.8 (b) showed the SCEF with the time lag (τ_{SQ}) removed, and the M pattern onset at ∼3 ms.

For the evaluation of the reproducibility across the participants, we measured the pairwise Pearson correlation coefficient as described in the analysis. Table 5.3 showed the correlation coefficient within the participants, with signals from Parti-

cipant 1, Participant 2, Participant 5 and Participant 6 highly correlating while the signal from Participant 4 was anticorrelated with the other for the MN stimulation. Similar results were observed for the TN runs, with significant correlation for Participant 3, Participant 4 and and Participant 5 and anticorrelated to Participant 6. Cortical responses were also correlated with mean coefficient correlation of 0.6 (2) and 0.5 (6) for MN and TN respectively.

Participants/ Stimuli	Median nerve (MN)	Tibial nerve (TN)
Participant 1-Participant 2	0.62 (0.2)	0.50 (0.13)
Participant 1-Participant 3	0.83 (0.2)	0.75 (0.07)
Participant 1-Participant 4	0.58 (0.2)	0.74 (0.08)
Participant 1-Participant 5	0.76 (0.1)	0.71 (0.09)
Participant 1-Participant 6	0.46 (0.2)	-0.82 (0.06)
Participant 2-Participant 3	0.63 (0.2)	0.75 (0.08)
Participant 2-Participant 4	-0.94 (0.03)	0.75 (0.08)
Participant 2-Participant 5	0.96 (0.02)	0.65 (0.1)
Participant 2-Participant 6	0.98 (0.01)	0.69 (0.1)
Participant 3-Participant 4	-0.50 (0.2)	0.97 (0.01)
Participant 3-Participant 5	0.75 (0.1)	0.80 (0.06)
Participant 3-Participant 6	0.53 (0.2)	-0.80 (0.06)
Participant 4-Participant 5	0.92 (0.05)	0.87 (0.04)
Participant 4-Participant 6	0.93 (0.04)	-0.85 (0.04)
Participant 5-Participant 6	0.90 (0.05)	-0.76 (0.07)

Table 5.3: Pearson correlation coefficient between participants for MN and TN stimulation. The bracketed values give the 95% confidence interval.

Figure 5.8 $(c)(d)$ showed two TN runs for different stimulus intensity. The SCEF ranged between -4 ms to 20 ms, where the response from -4 ms to 0 ms was the stimulation artifact and had the same pattern to both TN runs and to the MN run (a). Furthermore, the SCEF amplitude was increased with the stimulus intensity. The 17 mA TN run had a peak-to-peak amplitude of 400 fT at 2.3 ms ∼while the 35 mA TN run measured at 2.7 ms a peak with 780 fT.

MN cortical and spinal evoked responses were shown in figure 5.9 for Participant

2. The configuration of the sensors was illustrated in figure 5.9 (a).

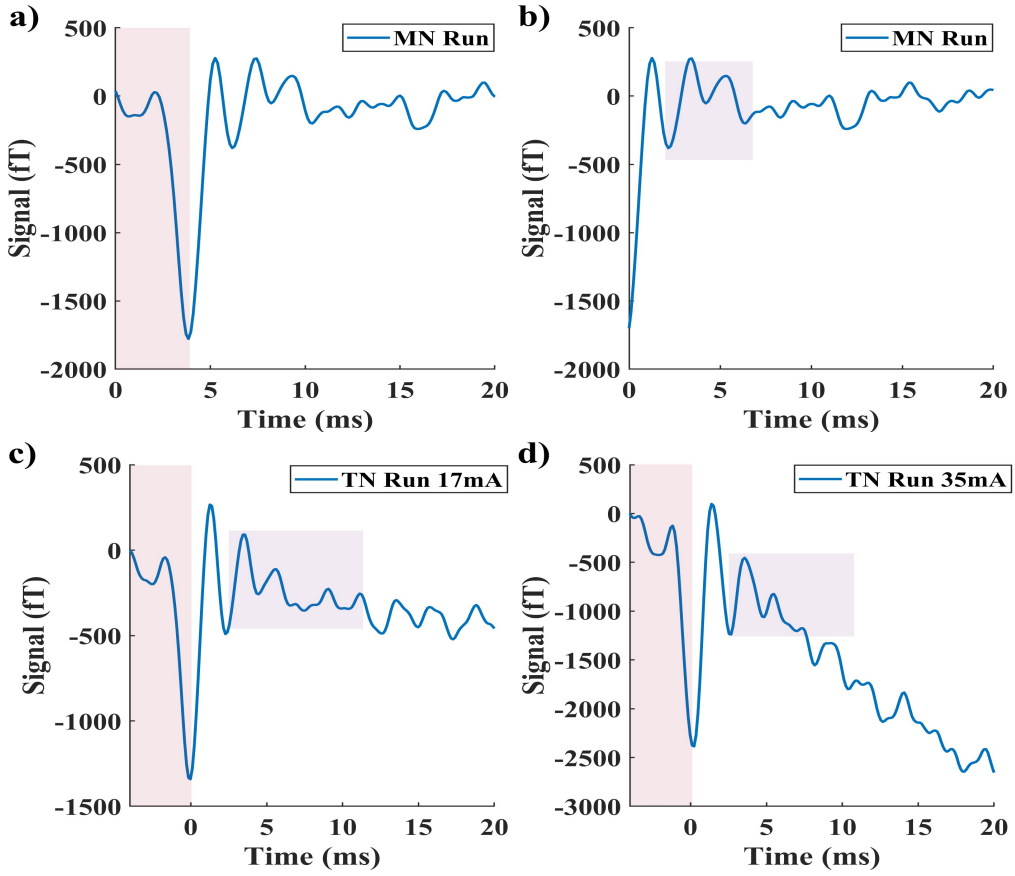

Figure 5.8: Spinal cord evoked field (SCEF) for MN and TN stimuli for Participant 1. $(a)(b)$ The MN SCEF (a) before the time-lag was removed and (b) after the time-lag removed. $(c)(d)$ TN SCEF in response (c) to 17 mA stimulus and (d) to 35 mA stimulus. The purple band indicates the characteristic SCEF pattern observed in all the runs.

The SEF had the characteristic P20 and P50 component for measurements in z-direction. The axial SEF did not record any characteristic components or patterns.

The mean component onset was measured at 21(2) ms for P20 and 48(2) ms for the P50. Figure 5.9 (c) plotted the SCEF in z ($SCEF_z$) and y direction ($SCEF_y$). Both field components recorded the characteristic M shape pattern, with the $SCEF_y$ response almost doubled in amplitude compared to the $SCEF_z$. The mean peak-to-peak amplitude was 152(20) fTand 294(38) fT for the $SCEF_z$ and $SCEF_y$. The mean time onset of the M component was at 3.6(1) ms and 4.1(4) ms for the z and y direction respectively. The SCEF recordings for Sensor 2 did not show any characteristic components and it was not include in the component onset analysis.

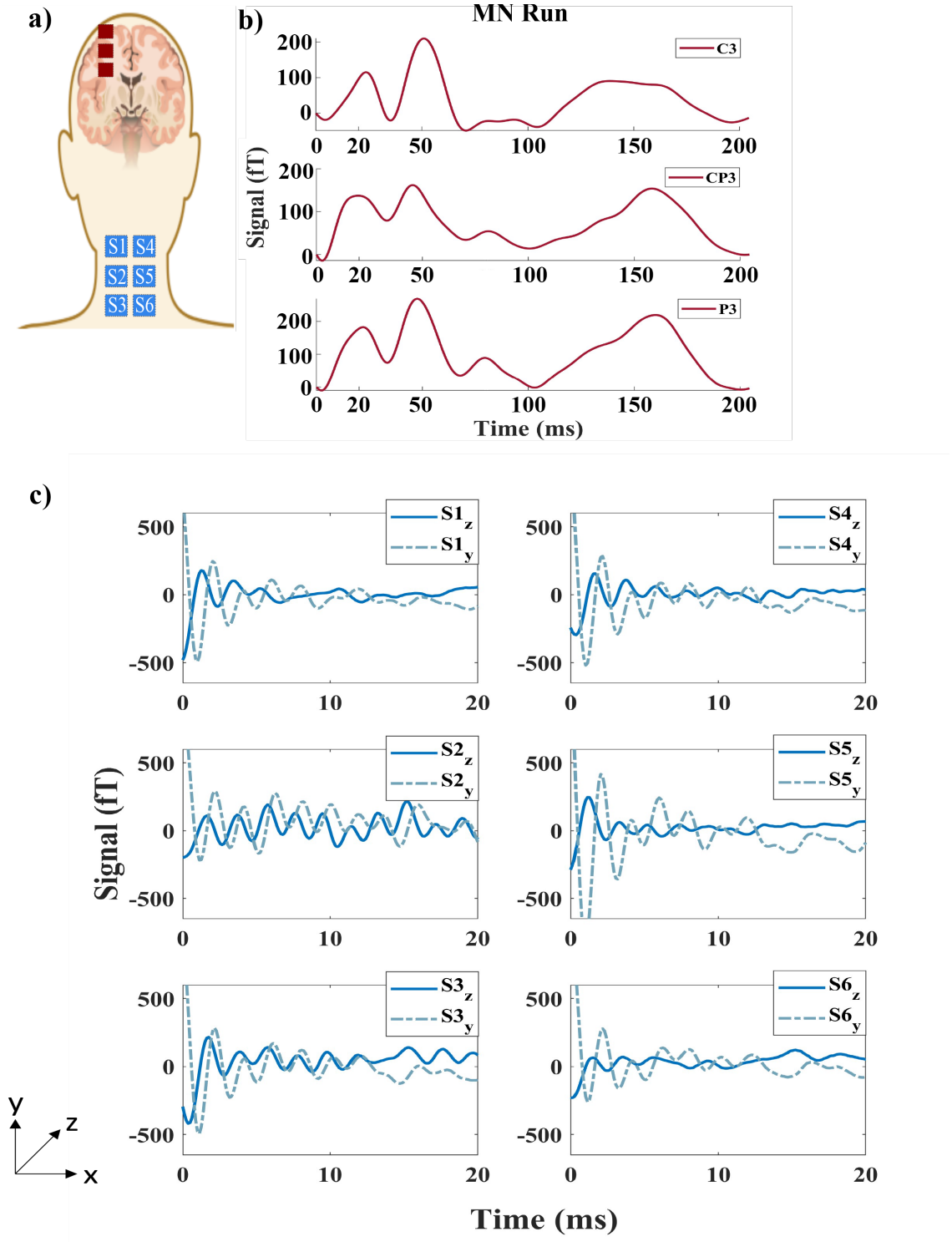

Figure 5.9: MN spinal cord evoked fields (SCEF) and somatosensory evoked fields (SEF) for Participant 2. (*a*) Sensor arrangement over the cortex (red) and the cervical spine (blue) for the MN run. (*b*) SEF (red trace) along the z direction for the three cortical sensors. (*c*) SCEF along the z (blue) and the y (dashed blue) direction for the six cervical sensors.

Figure 5.10 shows the TN SEF and SCEF for Participant 3. Figure 5.10 (a) illustrated the sensor placement for the cortex (red sensors), the cervical reference (green sensor) and the lumbar sensors (blue). SEF in z direction were plotted in figure 5.10 (b), where the characteristic component P45 and P100 appear in all the cortical sensors. The mean P45 onset was at 57(2) ms and the mean P110 onset was at 111(2) ms. The $SCEF_y$ and $SCEF_z$ were plotted for the cervical reference sensor (CSF) (c) and for the lumbar sensors (d). Both field components measured the M component, but the cervical spinal sensor amplitude was significantly reduced compared to the lumbar spinal sensors, with a local maximum at 50 fT and 105 fT for $SCEF_z$ and $SCEF_y$ respectively. The lumbar sensors recorded the M component with mean peak-to-peak amplitude of 351(31) fT and 317(45) fT for the z and y direction respectively. The mean onset was measured at 3.4(1) ms for $SCEF_z$ and 3.9(4) ms for $SCEF_y$.

The comparison of the spinal cord evoked fields to the phantom or semi-phantom fields was plotted in figure 5.11. The grand averaged spinal cord evoked fields (GASCEF) were compared to the corresponding grand averaged responses of the phantom and semi-phantom runs. GASCEF signal of Participant 3 was compared to the TN Phantom run (see figure 5.11(a)). The characteristic M component was observed for the Participant but was absent from the phantom GASCEF. In figure 5.11 (b), the differentiation between the semi-phantom and participant signal is not clear. The M component was present in the participant's signal but a similar signal pattern was recorded for the semi-phantom run. However, the participant's signal had $\sim$ 2 times higher peak-to-peak amplitude (144 fT) for the M component compared to the semi-phantom signal (84 fT). The MN run and MN semi-phantom run were recorded for Participant 2 and had the same stimulation intensity (7 mA). The difference between a TN run and a TN semi-run is more clear in figure 5.11 (c), where Participant's 4 TN response showed the M component, which was not observed in the TN semi-phantom. The semi-phantom run was recorded on Participant 3 but it was compared to Participant 4 TN run due to similar stimulus intensity levels (12 mA for the TN run and 18 mA for the TN semi-phantom run).

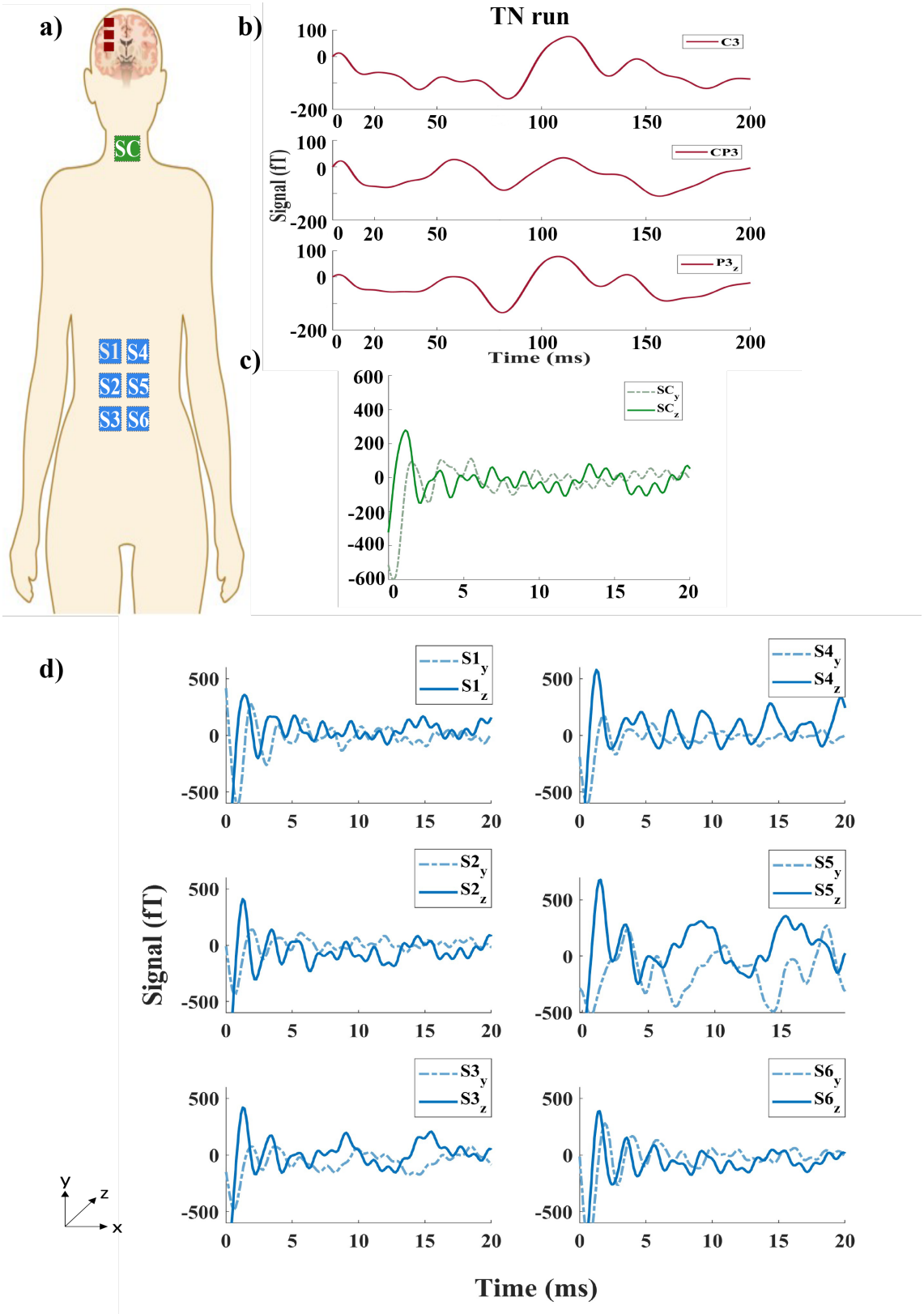

Figure 5.10: TN spinal cord evoked fields (SCEF) and somatosensory evoked fields (SEF) for Participant 3. (*a*) Sensor arrangement over the cortex (red), over the cervical spine reference *SC* (green) and the lumbar spine (blue) for the TN run. (*b*) SEF (red trace) along the z direction for the three cortical sensors. (*c*) SCEF for the cervical reference sensor along the z (green trace) and the y direction (dashed green trace). (*d*) SCEF along z (blue) and y (dashed blue) direction for the six lumbar sensors.

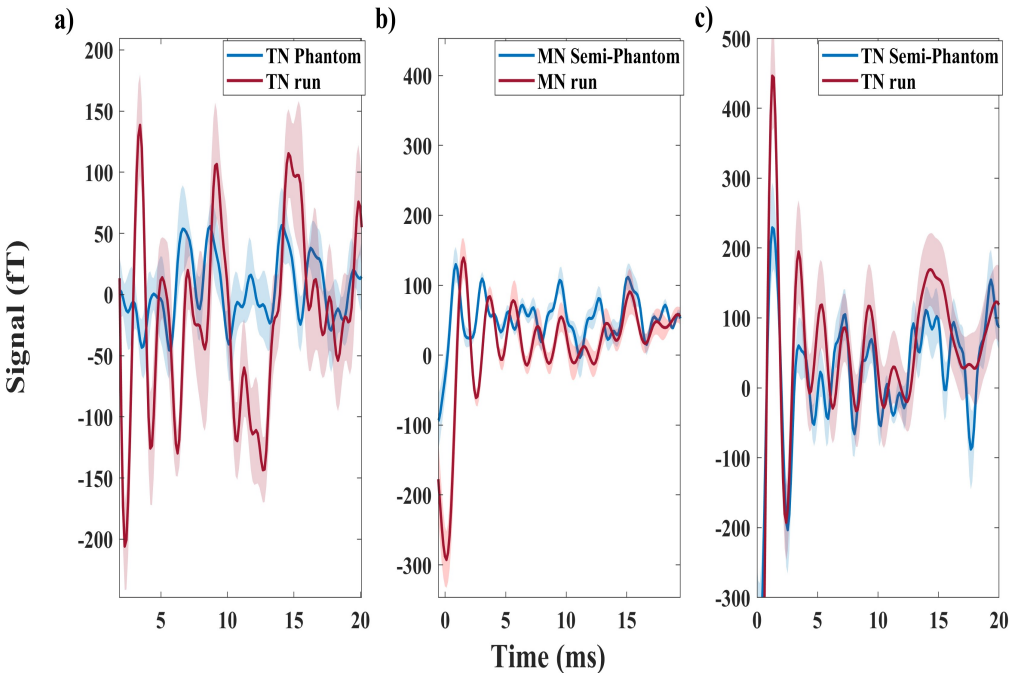

Figure 5.11: MN & TN grand averaged spinal cord evoked fields (GASCEF) compared to phantom & semi-phantom GASCEF. (*a*) TN GASCEF for Participant 3 (red) compared to TN $phantom_1$ GASCEF (blue). (*b*) MN GASCEF (red) compared to MN semi-phantom GASCEF (blue) for Participant 2. (*c*) TN GASCEF (red) for Participant 4 compared to semi-phantom GASCEF for Participant 3.

The spectral density of the MN run and semi-phantom MN run for Participant 2 is plotted in figure 5.12 for the z (a) and y (b) direction. The MN spectral density recorded an activation between 8 Hz and 15 Hz. The mean peak onset was measured as 11.7(5) ms and 11.9(5) mswith a mean spectral density of 811(28) $\mathrm{fT/Hz^{1/2}}$ and 495(35) $\mathrm{fT/Hz^{1/2}}$ for z and y direction respectively. The observed activation was above the calibrated noise-floor requirement measured in the simulation study (see table 5.1). The MN semi-phantom trace did not show any activation for the same frequency range. The 5 Hz stimulus appeared in both runs. Similar results were observed across all 6 participants.

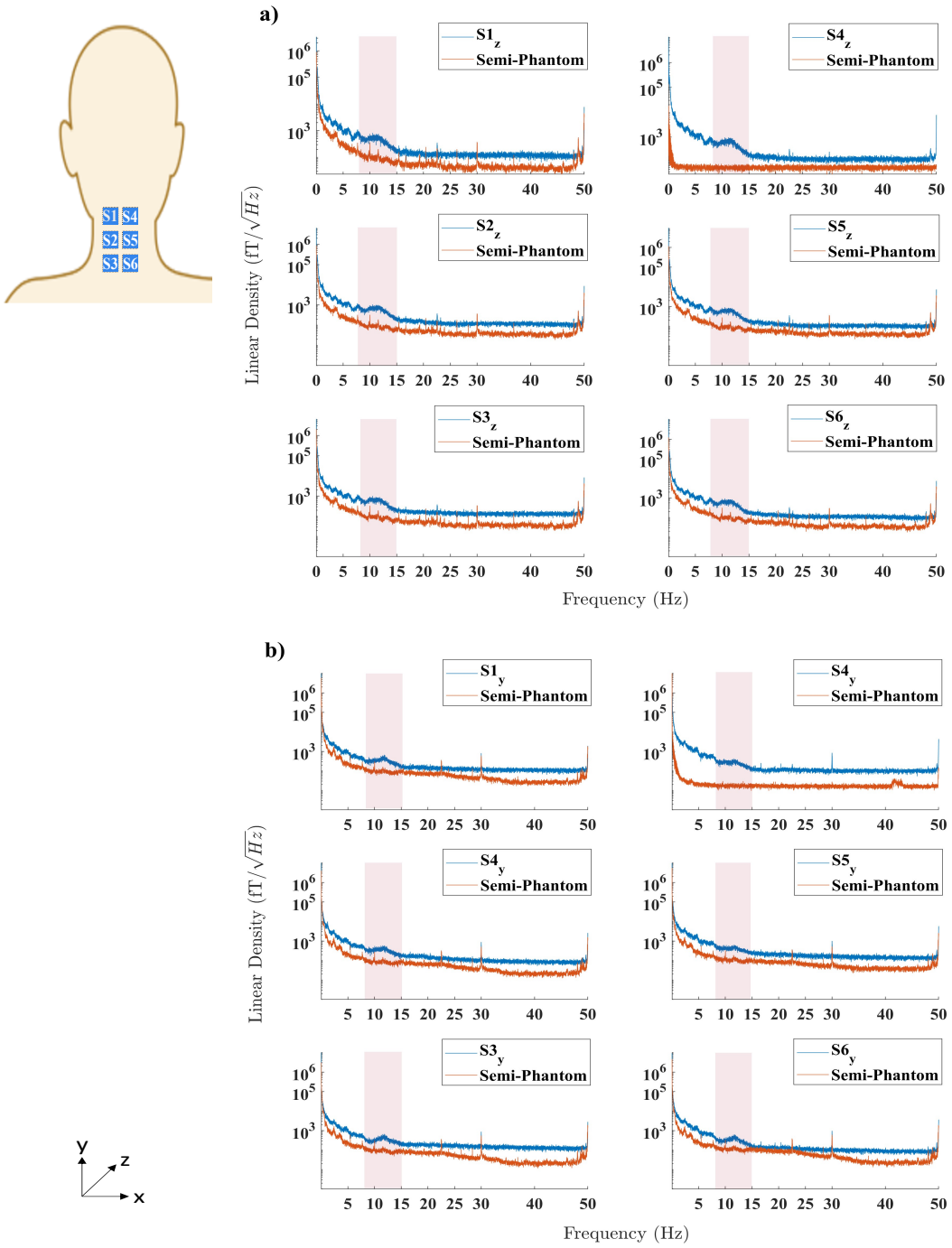

Figure 5.12: Spectral density of the MN run and MN semi-phantom for Participant 2 between 1 Hz to 50 Hz for (a) z direction and (b) y direction. The sensor placement is illustrated at the left corner. The coloured bar indicate the evoked response between 8 Hz and 15 Hz.

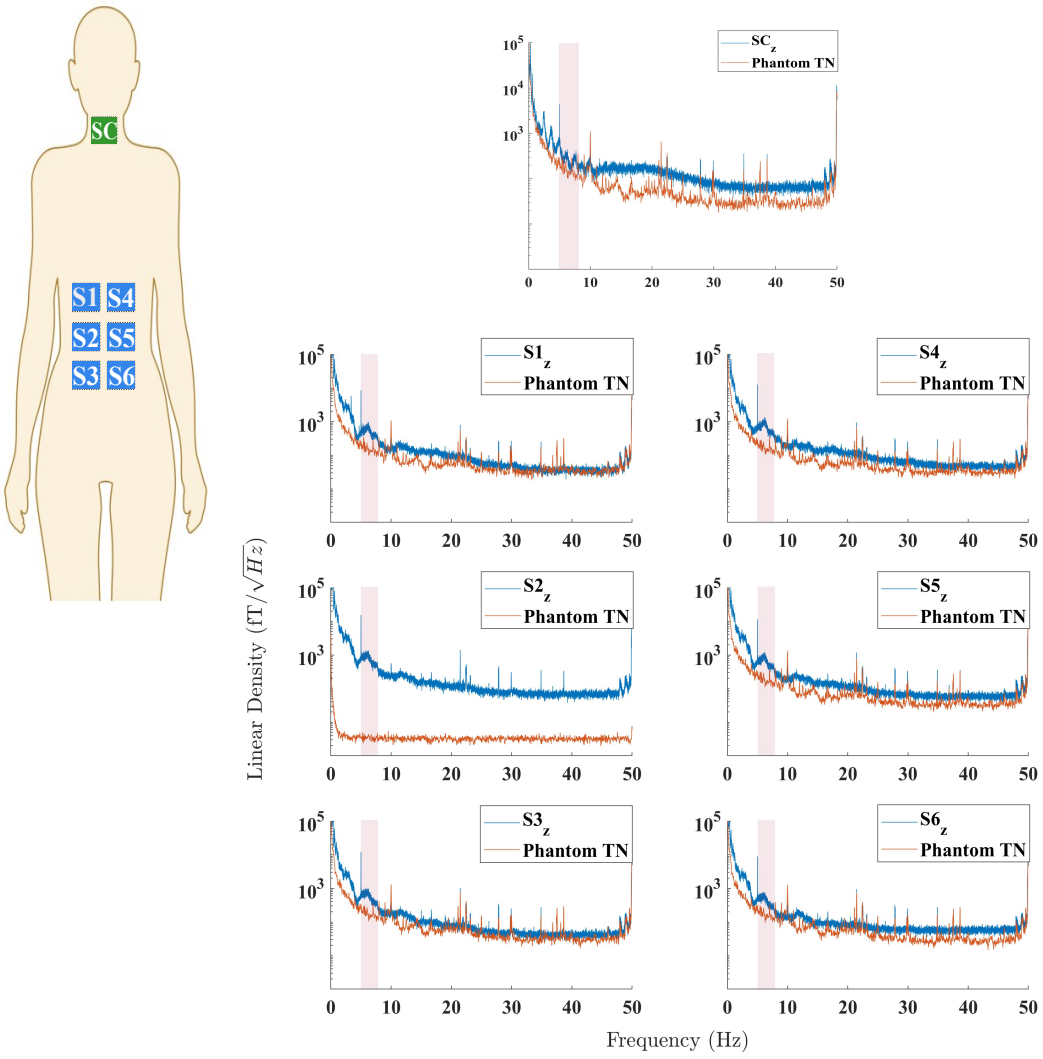

Figure 5.13: Spectral density of the TN run and TN *phantom*$_2$ for Participant 4 between 1 Hz to 50 Hz for the radial direction. The sensor placement is illustrated at the left corner. The coloured bar indicate the evoked response between 5 Hz and 8 Hz.

Figure 5.13 showed the spectral density of the TN run for Participant 1 and the TN *phantom*$_2$ run. Similar to the MN run, an activation was observed between 5 Hz and 8 Hz with mean onset at 6 Hz and mean spectral density of 1164(174) fT/Hz$^{1/2}$. The phantom trace did not show any activation for the same range. The 5 Hz stimulation can be observed in all the sensors. The cervical reference sensor (CS) did not measure similar activation patterns to the lumbar sensors, instead three individual activations were observed at 6 Hz, 7.5 Hz and 10 Hz. The signal in y direction did not record any activation as well. The S2 sensor was saturated during the phantom

run. Similar saturation of the same sensor was shown for the measurements in the TN semi-phantom result (figure 5.14). The saturation of the sensor might be due to the sensor location coupled with the high intensity of the stimulation (table 5.2).

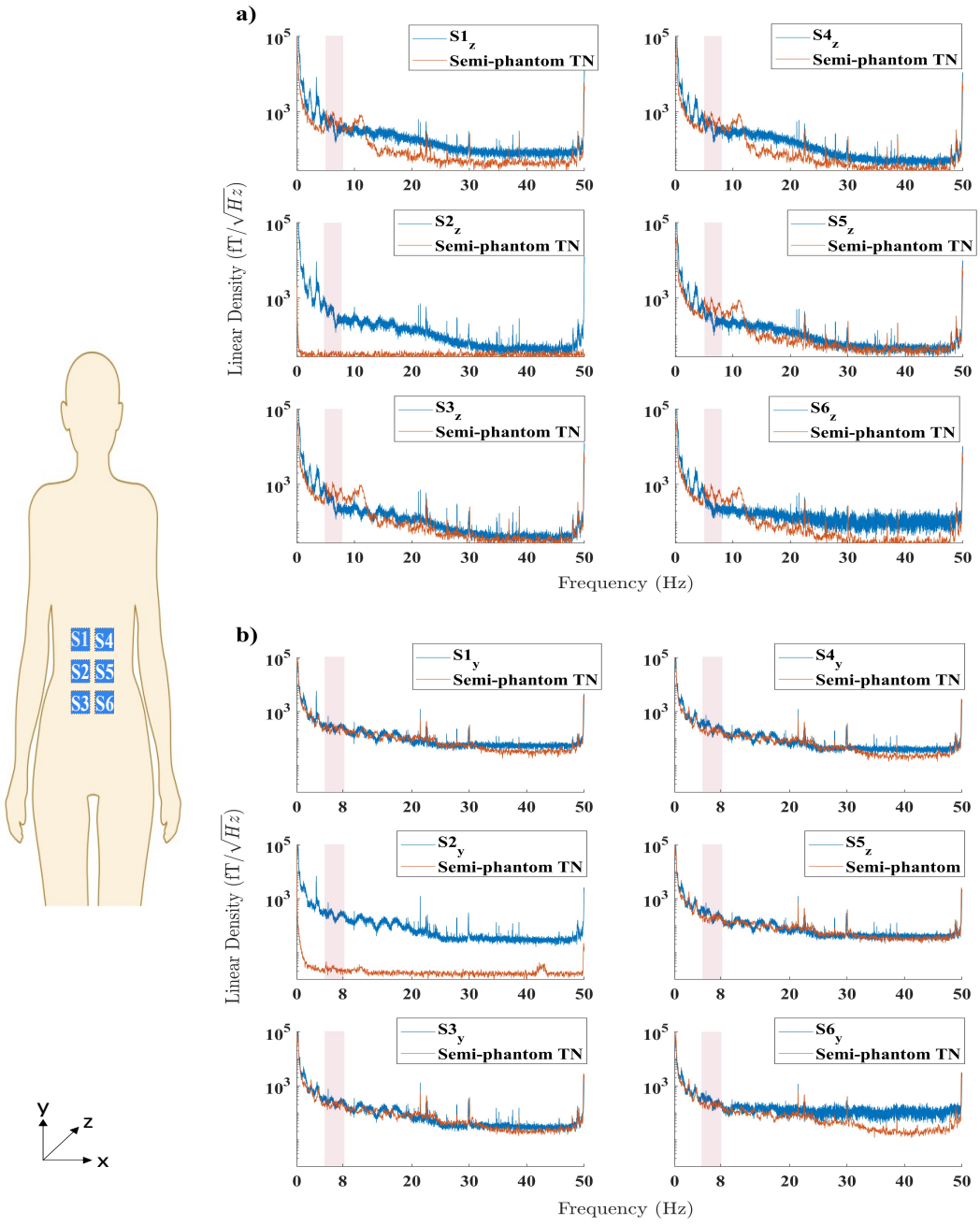

Figure 5.14: Spectral density of the TN run and TN semi-phantom for Participant 3 between 1 Hz to 50 Hz for (a) z direction and (b) y direction. The sensor placement is illustrated at the left corner. The coloured bar indicate the evoked response between 8 Hz and 15 Hz.

Similar activation between 5 Hz to 8 Hz was observed for Participant 3 TN run (figure 5.14 recorded in (a) z and (b) y direction. The distinction between the spinal cord and the semi-phantom signal is not clear, as the semi-phantom trace showed similar yet different activation patterns for the same frequency range.

The TN mean onset was calculated as 6(1) ms with mean spectral density of 640(58) fT/Hz$^{1/2}$ in figure 5.14 (a). Sensor 6 (S6) did not record the activation and was not included in the mean analysis The recorded spectral density in the y-direction did not present the same activation pattern, rather two individual activations similar to the figure 5.13 SC sensor with mean onset at 6(2) Hz and 7(3) Hz. The S2 sensor was saturated during the semi-phantom measurements, hence the measurements in z and y direction were not comparable to the S2 measurements in the TN run. A comparison between spinal cord and phantom measurements was plotted in figure 5.15 for a randomly selected sensor (S4).

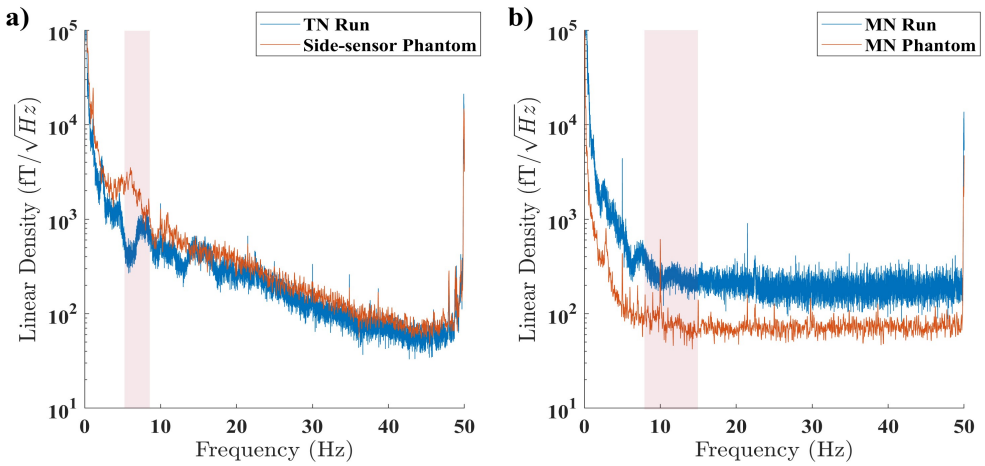

Figure 5.15: Spectral density of spinal cord measurements and phantom measurements for sensor 4. (a) TN run (blue) and side-sensor phantom run (orange) for Participant 2. The coloured bar indicates the activation frequency of 5 Hz-8 Hz. (b) MN run (blue) and MN $phantom_2$ run (orange) for Participant 5. The coloured bar indicates the activation onset between 8 Hz and 15 Hz. The traces were measured in z-direction.

Figure 5.15 (a) showed the spectral density of the TN run and side-sensor run for Participant 2. An activation in 5 Hz - 8 Hz was observed for the spinal cord data but not for the side-sensor phantom data. A different activation pattern was observed at 6 Hz in the side-sensor phantom. The stimulation intensity was the same in both

runs (12 mA).

The MN run and semi-phantom run of Participant 4 showed the activation between 8 Hz-15 Hz for the former while there were no observed activations for the latter. The stimulation intensity for the MN phantom run was at the maximum capacity of the stimulator (99.9 mA) and for the MN run was (8 mA).

5.3.5 Discussion

The simulation study showed that spinal cord imaging using OPM sensors is possible. To test this hypothesis, we used ten 2nd generation QuSpin sensors to simultaneously measure the spinal and cortical evoked fields in response to MN and TN stimulation. Highly reproducible cortical and spinal evoked responses were recorded for six participants (table 5.3).

Spinal cord evoked fields had the characteristic component M in all the measurements. However, this component is not well-defined and the onset varies in most studies (37; 34) The results agreed with some of the studies, with onset at ∼4 ms for MN and ∼5 ms for TN.

Repeating the experimental paradigms in two different stimulated sides (MN and TN) on six participant, showed the SEF and SCEF were highly reproducible (table 5.3).

Electric pulse stimulation combined with the movement of the stimulated area, created significant artifacts in the spinal cord measurements. To differentiate the spinal cord signal from the artifacts, a series of phantom and semi-phantom runs were measured. All the movement and stimulation artifacts were determined by the semi-phantom runs while the phantom runs showed the noise and produced artifacts associated to the stimulus intensity.

A direct comparison between the phantom/semi-phantom signal and the spinal cord signal identified a signal component which may correspond to the spinal cord response (figure 5.11). Although differences between the traces were observed (5.11 $(a)(c)$), for some traces the distinction between the spinal activation and artifact was not clear (see figure5.11 (b)). The spectral density of the results provided additional information and assisted in the validation of the spinal cord signal.

Finally, we illustrated for the first time to our knowledge, reproducible spinal

cord activations similar to the cortical θ-rhythm (4-8 Hz) and α-rhythm (8-12 Hz). For the MN run, the spinal sensors recorded a response between 8 Hz and 15 Hz over the cervical spine. These activations were measured for all participants and sensors and when compared to the semi-phantom run, it showed the neurological origin of the response. Interestingly, in the TN run we observed an activation between 5 Hz and 8 Hz, similar to θ rhythm, at the lumbar spine. These activation were more prompt for the radial measurements. The TN phantom run did not record any activation for the same frequency range (figure 5.13).

The TN semi-phantom run had a similar pattern activation, but instead of a prompt peak there were multiple short peaks for the same frequency range (figure 5.14). The TN semi-phantom activations are similar to the cervical reference sensors (CS) measurement (figure 5.13). In addition to these phantom runs, the side-sensor phantom and MN phantom further supports the neurophysiological origin of the alpha and theta activations (figure 5.15).

Although our results were reproducible and were observed for both stimulations, further investigation of the spinal cord responses is required. The identification of the spinal response between the stimulation and movement artifacts was not clear in all the runs (see figure 5.11(b), 5.14). The limited bandwidth and the 500 Hz bandstop filter of the QuSpin sensor should also be addressed. Different OPM sensors, such as the modular OPM, could be used to replicate the experiment and further validate the results. OPM sensors in an array configuration should be used to measure and characterise the propagating signal through the spinal cord. Furthermore, differences between bilateral and unilateral or electric and thermal stimuli should be further examined using the OPM spinal cord imaging system.

Based on the simulated and in-vivo results, OPM spinal imaging could be a reliable method to identify spinal cord evoked responses in response to various peripheral stimulations. An OPM spinal imaging array could have the potential to accurately measure the spinal neural speed and further explore the spatio-temporal characteristics of the propagating signal as it reaches the cortical area.

Chapter 6

Discussion & future work

6.1 Summary & Discussion

The primary aim of this thesis was to contribute to the characterisation of optically pumped magnetometers as a neuroimaging system. With the use of three key experiments, the advantages of the system were highlighted and compared to more commonly used methods. Apart from the advantages of the OPM based biomagnetic imaging system, the limitations of the current commercially available sensors were described in detail, along with suggested solutions which were tested experimentally and with a simulation.

The improved spatial and temporal resolution of the OPM-MEG system was shown in a pilot study, where two different visual stimuli were presented to three healthy participants. In order to validate and compare the OPM measurements, visually evoked fields were recorded by commercially available OPMs (QuSpin sensors) and SQUIDs.

Studies have shown the great potential of the commercially available OPMs in biomagnetic imaging, and their advantages over SQUID based systems (88; 93; 50). However, OPMs have not yet reached their full potential, with the design and configuration limiting their performance to specific applications. Due to the cross-talk between the QuSpin sensors, a separation distance of at least 2 cm is required to ensure their proper function (47; 89), which could limit the potential spatial coverage of the measured cortical or spinal region. In addition, the bandwidth of the sensors restricts them to measuring low frequency signals (< 100 Hz), excluding

the study of many high frequency biomagnetic responses. As a proposed solution, our team developed a novel modular OPM sensor, with the potential of a multi-axis modular OPM gradiometer array. This modular OPM has an increased bandwidth ($\sim$ 215 Hz) and reduced noise levels as a result of the common light source, and modular construction that could lead to easily improved system designs according to the experimental need.

The bandwidths of the QuSpin sensor and the ^{87}Rb modular OPM sensor are measured differently and that might reflect the bandwidth value difference. When the same bandwidth definition is used, the bandwidth values are comparable (see chapter 5.2.2). Even though the bandwidth of the sensors could be similar, the modular OPM could still have a significant advantage in high-frequency signal measurements due to the lack of the 500 Hz cut-off frequency and the reduced cross-talked.

As a proof of principle, alpha brain rhythms were measured in two healthy participants using a single-axis modular OPM. In humans, the alpha rhythm has a frequency onset of 8-13 Hz (125) and is usually measured over the parieto-occipital lobe (126). Alpha activations are highly enhanced whilst the eyes-closed condition. Hence, the suitability of the modular OPM was shown through the excitement and suppression of the alpha wave through three simple paradigms: open/closed eyes (Run_1), eyes open (Run_2) and eyes closed (Run_3). The results were consistent with the literature (125) and showed the enhanced alpha activation in Run_1 during the eyes-closed condition and the continuous alpha activation in Run_3. Although, the measured alpha activations showed the suitability of the sensors for neurophysiological measurements, further studies are required to characterise the modular OPM system in biomagnetic imaging.

The study of spinal cord responses is challenging, due to the high frequency (91) and deep neuronal sources (92). EEG electrodes have been successfully used for studying spinal cord evoked responses, with the epidural catheter electrodes providing more insight of the spinal cord function. OPMs could assist the evaluation and study of the functional spinal cord, as the skin-to-surface distance is minimised to 3-5 mm (88) and have improved spatiotemporal resolution (93; 50). In order to test this hypothesis, a simulated spinal cord response was measured by the modular OPM and the QuSpin sensor. Although both sensors measured successfully the reference

signal, the limited bandwidth coupled with the 500 Hz bandstop filter effected the QuSpin measurement with a delayed signal onset. Similar, but significantly shorter onset delay was observed in the modular OPM's measurement.

An in-vivo study aimed to verify the simulated results by measuring the spinal cord evoked fields and somatosensory evoked fields using the QuSpin sensors. The study used two well-defined stimulation paradigms to induce evoked responses on the spine and brain; the median nerve and the tibial nerve stimulation (32). A 2×6 QuSpin array was placed over the cervical or tibial spinal cord for median nerve or tibial nerve stimulation, respectively. The in-vivo results showed that the QuSpin sensors can be used for spinal cord measurements, as the characteristic wave patterns were observed in all the six participants (37) . However, the spinal cord measurements were limited by the stimulation artifacts. Thus, the participants' results were compared to phantom and semi-phantom measurements to determine the validity of the hypothesis. Although differences between the spinal cord responses and the phantom/semi phantom traces were observed in most of the experimental runs, for some traces the distinction between the spinal activation and artifact was not clear.

In addition to the characteristic wave patterns, spinal cord measurements had a reproducible frequency response which was observed in all the runs but not in the phantom and semi-phantom runs. The spinal cord responses had a frequency onset between 8-13 Hz in median nerve stimulation runs, while the tibial nerve stimulation had a frequency onset between 4-8 Hz. Although similar activations have not been reported in previous studies to our knowledge, the reproducibility and absence in the phantom or semi-phantom data indicate the neurophysiological origin. However, further research is required in order to validate and understand these observations.

6.2 Future Work

OPM based neuroimaging systems are still an emerging field, and further research is required in order to fully characterise their capabilities and optimise their function. In this section, I suggest a series of studies to further support and validate the experimental results presented in this thesis. These studies would aid the charac-

terisation of the OPM system and address some of its limitations. Furthermore, as a future goal in neuroscientific research, I suggest the implementation of transcranial stimulation techniques coupled with an OPM based imaging system to further expand the possible applications of the method.

The improved spatiotemporal resolution of the QuSpin OPM based system was shown in a well-defined study of the visually evoked response. Although the results were highly reproducible, the experiment was limited by the small number of participants and the poor noise floor of the data acquisition system (DAQ). Future research should focus on conducting similar OPM experiments using different visual stimulation in a larger population – more than 10 participants – to further verify the spatio-temporal localization of the propagating signal between the primary visual cortex (V1) and the associative visual cortex (V2/V3). Such experiments could also validate the increased spatio-temporal resolution of the OPM system compared to other imaging methods. Studies should further confirm the enhanced spatiotemporal resolution of the system under the same or different experimental paradigms, using a larger number of sensors in order to enhance the spatial coverage and to obtain a detailed description of the propagating signal. Then, the comparison between the OPM-MEG and the full-head SQUID-MEG system or EEG system, coupled with an improvement of the DAQ noise floor could further support the enhanced spatiotemporal resolution observed in our results.

The development of the modular OPM sensor provided a new possible application of the OPM-MEG. Further research is required in order to validate the suitability of the modular OPM in biomagnetic measurements. With a focus on the enhanced features of the sensor, further studies should use a well-define paradigm, similar to the one used in the study presented in Chapter 3. Hence, by using one or more single-axis modular OPM, one could use the same or similar experimental paradigm and verify three things: the sensitivity level of the modular OPM compared to the QuSpin OPM, the verification of the localisation of the propagating signal between the primary visual cortex (V1) and the associative visual cortex (V2/V3), and the enhanced spatiotemporal resolution of the OPM based system. With the development of a multi-axis modular OPM gradiometer array, studies should focus on experimental protocols to verify the increased spatio-temporal resolution and the

reduced noise level (hence increased signal to noise ratio) of the system. A significant improvement in the source localisation precision compared to QuSpin sensors or full head SQUID based systems is expected.

Importantly, the OPM system should be tested in a range of research and clinical applications. The implementation of an OPM spinal cord imaging system could aid the characterization of healthy spinal cord responses or even the identification of functional deficiencies in preclinical or prodromal stages.

The study of the functional spinal cord was challenging, even with OPM sensors. The identification of the spinal cord signal and the artifacts was not always clear in the measurements. Future research should measure spinal cord signals in response to different stimulations or stimulated areas, such as: thermal stimulation, the difference of unilateral and bilateral stimulation and stimulation without inducing muscle movement. The different stimulation modalities (type of stimulation, frequency and intensity) could further validate the results shown in Chapter 5 and aid the optimisation of the OPM sensors for spinal cord imaging.

The development of the modular OPM gradiometer system could provide a neuroimaging system able to measure the rapid and weak spinal cord responses. The simulation results already exhibit the enhanced performance of the single-axis modular OPM compared to the QuSpin sensor in high frequency signals. Consequently, the modular OPM gradiometer array would be ideal for spinal cord measurements due to the significantly reduced artifacts induced by the stimulation and movement, which are affecting the current measurements. This is a significant improvement, as the modular OPM array could be an alternative to invasive imaging methods which are currently used to further characterise healthy and clinical spinal cord responses.

OPM biomagnetic imaging could aid the understanding of neural networks and the connectivity of functionally related brain areas. Brain stimulation methods, such as transcranial magnetic stimulation (TMS) (150) and trascranial direct current stimulation (tDCS) (151), are plausible treatments of neurological and psychiatric disorders, with the former already approved by the US Food and Drug Administration (FDA) as a method for language mapping (152) and migraine treatment (153; 154). Therefore, the combination of an OPM system with a noninvasive transcranial brain stimulation could aid the characterization of the healthy and

pathological brain with different disorders and conditions. However, these neuromodulation methods induce electric or magnetic pulses, which interfere with the proper operation of the OPMs, making the combination of the methods challenging. Consequently, I suggest that future research should focus on the development of a compatible OPM method with neuromodulation systems to further investigate the healthy and pathological brain.

The work in this thesis aids the characterisation of the OPM sensors in biomagnetic imaging, highlighting the improved features of the sensors and their limitations. Although further research is essential for the development of a fully integrated neuroimaging system, I believe OPM systems will become the preferred biomagnetic imaging method.

Abbreviations

AP Action Potential

BS Beam Splitter

CNS Central Nervous System

CS Cervical Spine

CSF Cerebrospinal Fluid

CT Computed Tomography

DAQ Data Acquisition System

EEG Electroencephalography

EPSP Excitatory Post Synaptic Potential

fMRI Functional Magnetic Resonansce Imaging

FOI Frequency Of Interest

FS Flash Stimulus

fT Femto Tesla

GSCEF Grand Averaged Spinal Cord Evoked Fields

IPSP Inhibitory Post Synaptic Potential

JJ Josephson Junctions

LIA Lock-In Amplifier

LP Linear Polariser

LS Lumbar Spine

MCG Magnetocardiography

MEG Magnetoencephalography

MN Median Nerve

MRI Magnetic Resonance Imaging

MSC Magnetically Shielded Cylinder

MSE Magnetically Shielded Environment

MSG Magnetospinography

MSR Magnetically Shielded Room

OPM-MEG Optically Pumped Magnetometers-Magnetoencephalography

OPM Optically Pumped Magnetometers

PD Photodiode

PET Positron Emission Tomography

PR Pattern Reversal Stimulus

PSP Post Synaptic Potential

pT Pico Tesla

SCEF Spinal Cord Evoked Fields

SEF Somatosensory Evoked Fields

SERF Spin Exchange Relaxation Free

SLS Sacral Spine

SnR Signal To Noise Ratio

SQUID Superconducting Quantum Interference Device

SQUID-MEG Superconducting Quantum Interference Device-Magnetoencephalography

SRT Spinoreticulothalamic Track

ST Spinotectal Track

STT Spinothalamic Track

TN Tibial Nerve

TS Thoracic Spine

VEF Visually Evoked Fields

VER Visually Evoked Responses

List of Tables

List of Figures

Bibliography

[1] D. S. Bassett and M. S. Gazzaniga, "Understanding complexity in the human brain Danielle," *Trends in Cognitive Sciences*, vol. 15, no. 5, pp. 200–209, 2011. 2

[2] S. E. Arnold, J. Q. Trojanowski, R. E. Gur, P. Blackwell, L.-Y. Han, and C. Choi, "Absence of neurodegeneration and neural injury in the cerebral cortex in a sample of elderly patients with schizophrenia," *Archives of General Psychiatry*, vol. 55, pp. 225–232, 03 1998. 2

[3] H. Berger, "Über das Elektrenkephalogramm des Menschen," *Archiv für Psychiatrie und Nervenkrankheiten*, vol. 87, pp. 527–570, 12 1929. 2

[4] D. Cohen, "Magnetoencephalography: Detection of the Brain's Electrical Activity with a Superconducting Magnetometer," *Science*, vol. 175, pp. 664 LP – 666, feb 1972. 2, 4, 21, 61

[5] S. Ogawa, T.-M. Lee, A. S. Nayak, and P. Glynn, "Oxygenation-sensitive contrast in magnetic resonance image of rodent brain at high magnetic fields," *Magnetic Resonance in Medicine*, vol. 14, pp. 68–78, apr 1990. 2

[6] X. Pan, J. Siewerdsen, P. J. La Riviere, and W. A. Kalender, "Anniversary paper: Development of x-ray computed tomography: The role of medical physics and aapm from the 1970s to present," *Medical Physics*, vol. 35, no. 8, pp. 3728–3739, 2008. 2

[7] J. A. Camprodon and T. A. Stern, "Selecting Neuroimaging Techniques," *The Primary Care Companion For CNS Disorders*, vol. 15, no. 4, pp. 1–13, 2013. 2

[8] A. Filler, "The History, Development and Impact of Computed Imaging in Neurological Diagnosis and Neurosurgery: CT, MRI, and DTI," *Nature Precedings*, pp. 1–76, 2009. 2

[9] P. A. Tataranni and A. DelParigi, "Functional neuroimaging: a new generation of human brain studies in obesity research.," *Obesity reviews : an official journal of the International Association for the Study of Obesity*, vol. 4, no. 4, pp. 229–238, 2003. 2

[10] A. C. Papanicolaou, *Clinical magnetoencephalography and magnetic source imaging*, vol. 9780521873. 2009. 3, 7, 11, 16

[11] E. D. Bigler, "Structural neuroimaging in sport-related concussion," *International Journal of Psychophysiology*, vol. 2018, p. 20002, 2017. 3

[12] J. D. Clayden, "Imaging connectivity: MRI and the structural networks of the brain," *Functional Neurology*, vol. 28, no. 3, pp. 197–203, 2013. 3

[13] M. H. Mohajerani, A. W. Chan, M. Mohsenvand, J. LeDue, R. Liu, D. A. McVea, J. D. Boyd, Y. T. Wang, M. Reimers, and T. H. Murphy, "Spontaneous cortical activity alternates between motifs defined by regional axonal projections," *Nature neuroscience*, vol. 16, pp. 1426–1435, oct 2013. 3

[14] J. Fiser, C. Chiu, and M. Weliky, "Small modulation of ongoing cortical dynamics by sensory input during natural vision," *Nature*, vol. 431, no. 7008, pp. 573–578, 2004. 3

[15] R. M. Chapman, M. N. Gardner, R. Klorman, M. Mapstone, A. P. Porsteinsson, I. M. Antonsdottir, and L. Kamalyan, "Temporospatial components of brain ERPs as biomarkers for Alzheimer's disease," *Alzheimer's & dementia (Amsterdam, Netherlands)*, vol. 10, pp. 604–614, aug 2018. 3

[16] M. Song, M. Kang, H. Lee, Y. Jeong, and S. B. Paik, "Classification of Spatiotemporal Neural Activity Patterns in Brain Imaging Data," *Scientific Reports*, vol. 8, no. 1, pp. 1–12, 2018. 3

[17] F. Di Lorenzo, C. Motta, E. P. Casula, S. Bonnì, M. Assogna, C. Caltagirone, A. Martorana, and G. Koch, "LTP-like cortical plasticity predicts conversion

to dementia in patients with memory impairment," *Brain Stimulation*, vol. 13, no. 5, pp. 1175–1182, 2020. 3

[18] U. B. Barnikol, K. Amunts, J. Dammers, H. Mohlberg, T. Fieseler, A. Malikovic, K. Zilles, M. Niedeggen, and P. A. Tass, "Pattern reversal visual evoked responses of V1/V2 and V5/MT as revealed by MEG combined with probabilistic cytoarchitectonic maps," *NeuroImage*, vol. 31, no. 1, pp. 86–108, 2006. 3, 44

[19] F. Di Russo, A. Martínez, M. I. Sereno, S. Pitzalis, and S. A. Hillyard, "Cortical sources of the early components of the visual evoked potential," *Human Brain Mapping*, vol. 15, no. 2, pp. 95–111, 2002. 3, 29, 38, 44, 45, 47

[20] W. Orrison and J. Lewine, *Functional Brain Imaging*, vol. 52. Mosby, 1995. 3

[21] C. Babiloni, V. Pizzella, C. D. Gratta, A. Ferretti, and G. L. Romani, "Chapter 5 Fundamentals of Electroencefalography, Magnetoencefalography, and Functional Magnetic Resonance Imaging," *International Review of Neurobiology*, vol. 86, no. 09, pp. 67–80, 2009. 3, 7, 8

[22] G. Baule and R. McFee, "Detection of the magnetic field of the heart," *American Heart Journal*, vol. 66, no. 1, pp. 95–96, 1963. 3

[23] D. Cohen, "Magnetic fields around the torso: Production by electrical activity of the human heart," *Science*, vol. 156, no. 3775, pp. 652–654, 1967. 3

[24] Cohen, "Magnetoencephalography: Evidence of Magnetic Fields Produced by Alpha-Rhythm Currents," 1968. 3

[25] J. E. Zimmerman, P. Thiene, and J. T. Harding, "Design and operation of stable rf-biased superconducting point-contact quantum devices, and a note on the properties of perfectly clean metal contacts," *Journal of Applied Physics*, vol. 41, no. 4, pp. 1572–1580, 1970. 3

[26] D. Cohen, E. A. Edelsack, and J. E. Zimmerman, "Magnetocardiograms taken inside a shielded room with a superconducting point-contact magnetometer," *Applied Physics Letters*, vol. 16, no. 7, pp. 278–280, 1970. 3

[27] K. T. E. Olde Dubbelink, A. Hillebrand, D. Stoffers, J. B. Deijen, J. W. R. Twisk, C. J. Stam, and H. W. Berendse, "Disrupted brain network topology in Parkinson's disease: A longitudinal magnetoencephalography study," *Brain*, vol. 137, no. 1, pp. 197–207, 2014. 4, 50

[28] K. Barik, K. Watanabe, J. Bhattacharya, and G. Saha, "Classification of Autism in Young Children by Phase Angle Clustering in Magnetoencephalogram Signals," *2020 National Conference on Communications (NCC)*, pp. 1–6, 2020. 4

[29] P. K. Mandal, A. Banerjee, M. Tripathi, and A. Sharma, "A Comprehensive Review of Magnetoencephalography (MEG) Studies for Brain Functionality in Healthy Aging and Alzheimer's Disease (AD)," *Frontiers in Computational Neuroscience*, vol. 12, pp. 1–40, 2018. 4, 50

[30] B. T. Dunkley, R. Jetly, E. W. Pang, and M. J. Taylor, "New perspectives on the neurobiology of PTSD: High-resolution imaging of neural circuit (dys)function with magnetoencephalography," *Journal of Military, Veteran and Family Health*, vol. 6, no. S1, pp. 16–25, 2020. 4

[31] Y. Adachi, J. Kawai, Y. Haruta, M. Miyamoto, S. Kawabata, K. Sekihara, and G. Uehara, "Recent advancements in the SQUID magnetospinogram system," *Superconductor Science and Technology*, vol. 30, no. 6, 2017. 4, 11, 20

[32] "Somatosensory evoked potentials," *Handbook of Clinical Neurology*, vol. 160, pp. 523–540, 2019. 4, 80, 81, 85, 86, 102

[33] J. F. Burke, N. Kunwar, M. S. Yaroshinsky, K. H. Louie, P. Shirvalkar, P. Su, M. Henry, G. Pasvankas, L. Poree, L. Jacques, and D. D. Wang, "Epidural Spinal Electrogram Provides Direct Spinal Recordings in Awake Human Participants," *Frontiers in Human Neuroscience*, vol. 15, no. October, pp. 1–11, 2021. 4

[34] Y. Miyano, S. Kawabata, M. Akaza, K. Sekihara, Y. Hoshino, T. Sasaki, T. Watanabe, S. C. Kim, S. Sato, Y. Mitani, Y. Adachi, and A. Okawa, "Visualization of electrical activity in the cervical spinal cord and nerve roots after

ulnar nerve stimulation using magnetospinography," *Clinical Neurophysiology*, vol. 131, no. 10, pp. 2460–2468, 2020. 4, 69, 72, 80, 87, 98

[35] S. Ishii, S. Kawabata, S. Tomizawa, M. Tomori, K. Sakaki, K. Shinomiya, K. Sekihara, T. Sato, Y. Adachi, and A. Okawa, "Conductive neuromagnetic fields in the lumbar spinal canal," *Clinical Neurophysiology*, vol. 123, no. 8, pp. 1656–1661, 2012. 4, 87

[36] S. Ushio, Y. Hoshino, S. Kawabata, Y. Adachi, K. Sekihara, S. Sumiya, D. Ukegawa, K. Sakaki, T. Watanabe, Y. Hasegawa, and A. Okawa, "Visualization of the electrical activity of the cauda equina using a magnetospinography system in healthy subjects," *Clinical Neurophysiology*, vol. 130, no. 1, pp. 1–11, 2019. 4, 87

[37] S. Sumiya, S. Kawabata, Y. Hoshino, Y. Adachi, D. Oyama, S. Kawabata, K. Sekihara, Y. Haruta, G. Uehara, and A. Okawa, "Magnetospinography visualizes electrophysiological activity in the cervical spinal cord," *Scientific Reports*, vol. 7:2192, no. 3, pp. 326–333, 2017. 4, 87, 98, 102

[38] J. C. Allred, R. N. Lyman, T. W. Kornack, and M. V. Romalis, "High-Sensitivity Atomic Magnetometer Unaffected by Spin-Exchange Relaxation," *Physical Review Letters*, vol. 89, p. 130801, sep 2002. 4

[39] W. E. Bell and A. L. Bloom, "Optical detection of magnetic resonance in alkali metal vapor," *Physical Review*, vol. 107, no. 6, pp. 1559–1565, 1957. 4

[40] A. L. Bloom, "Principles of Operation of the Rubidium Vapor Magnetometer," *Applied Optics*, vol. 1, no. 1, p. 61, 1962. 4

[41] C. C.-T. J.Dupont-Roc, S. Haroche, "Detection of very weak magnetic fields (109gauss) by 87Rb zero-field level crossing resonances," *Physics Letters*, vol. 28, no. 9, pp. 638–639, 1969. 4, 22

[42] A. Kastler, "The Hanle effect and its use for the measurements of very small magnetic fields," *Nuclear Instruments and Methods*, vol. 110, no. C, pp. 259–265, 1973. 4

[43] D. Budker, D. F. Kimball, S. M. Rochester, V. V. Yashchuk, and M. Zolotorev, "Sensitive magnetometry based on nonlinear magneto-optical rotation," *Phys. Rev. A*, vol. 62, p. 043403, Sep 2000. 5, 21

[44] I. K. Kominis, T. W. Kornack, J. C. Allred, and M. V. Romalis, "A subfemtotesla multichannel atomic magnetometer," *Nature*, vol. 422, no. 6932, pp. 596–599, 2003. 5, 21, 32, 53

[45] G. Bison, R. Wynands, and A. Weis, "A laser-pumped magnetometer for the mapping of human cardiomagnetic fields," *Applied Physics B: Lasers and Optics*, vol. 76, no. 3, pp. 325–328, 2003. 5

[46] H. Xia, A. Ben-Amar Baranga, D. Hoffman, and M. V. Romalis, "Magnetoencephalography with an atomic magnetometer," *Applied Physics Letters*, vol. 89, no. 21, pp. 2004–2007, 2006. 5

[47] V. Shah, J. Osborne, J. Orton, and O. Alem, *Fully integrated, standalone zero field optically pumped magnetometer for biomagnetism.* No. February, 2018. 5, 22, 23, 25, 54, 77, 78, 100

[48] R. A. Seymour, N. Alexander, S. Mellor, G. C. O'Neill, T. M. Tierney, G. R. Barnes, and E. A. Maguire, "Using OPMs to measure neural activity in standing, mobile participants," *NeuroImage*, vol. 244, no. May, p. 118604, 2021. 5, 6

[49] N. An, F. Cao, W. Li, W. Wang, W. Xu, C. Wang, M. Xiang, Y. Gao, B. Sui, A. Liang, and X. Ning, "Imaging somatosensory cortex responses measured by opm-meg: Variational free energy-based spatial smoothing estimation approach," *iScience*, vol. 25, no. 2, p. 103752, 2022. 5, 69

[50] A. Gialopsou, C. Abel, T. M. James, T. Coussens, M. G. Bason, R. Puddy, F. D. Lorenzo, K. Rolfs, J. Voigt, T. Sander, M. Cercignani, and P. Krüger, "Improved spatio-temporal measurements of visually evoked fields using optically-pumped magnetometers," *Scientific Reports*, vol. 11, p. 22412, 123. 5, 52, 53, 100, 101

[51] U. Vivekananda, S. Mellor, T. M. Tierney, N. Holmes, E. Boto, J. Leggett, G. Roberts, R. M. Hill, V. Litvak, M. J. Brookes, R. Bowtell, G. R. Barnes, and M. C. Walker, "Optically pumped magnetoencephalography in epilepsy," *Annals of Clinical and Translational Neurology*, vol. 7, no. 3, pp. 397–401, 2020. 5, 6

[52] S. Knappe, T. Sander, and L. Trahms, *Optically-Pumped Magnetometers for MEG*. Springer Verlag, Heidelberg,, 2014-08-08 2014. 5, 34, 80

[53] T. Coussens, C. Abel, A. Gialopsou, M. G. Bason, T. M. James, F. Oruević, and P. Kruger, "Modular optically-pumped magnetometer system," 2021. 5, 55, 77, 78

[54] W. Fourcault, R. Romain, G. Le Gal, F. Bertrand, V. Josselin, M. Le Prado, E. Labyt, and A. Palacios-Laloy, "Helium-4 magnetometers for room-temperature biomedical imaging: toward collective operation and photon-noise limited sensitivity," *Optics Express*, vol. 29, no. 10, p. 14467, 2021. 5, 54

[55] E. R. Kandel, J. H. Schwartz, and T. M. Jessell, *Principles of Neural Science*. McGraw-Hill Education / Medical, 2013. 7, 9, 11, 13, 14, 16, 69

[56] Peter C. Hansen, M. L. Kringelbach, and R. Salmelin, *MEG: An Introduction to Methods*. Oxford University Press, Inc, 201. 7, 10, 11, 13, 14, 17, 18

[57] G. J. Augustine, D. M. Chikaraishi, M. D. Ehlers, and E. Al, *Neuroscience*, vol. 6. 2004. 8, 9, 12, 13

[58] M. Hämäläinen, R. Hari, R. J. Ilmoniemi, J. Knuutila, and O. V. Lounasmaa, "Magnetoencephalography theory, instrumentation, and applications to noninvasive studies of the working human brain," *Reviews of Modern Physics*, vol. 65, no. 2, pp. 413–497, 1993. 8, 9, 10, 12, 14

[59] D. H. Hubel, "The Brain," *Scientific American*, vol. 241, no. September, pp. 45–53, 1979. 9

[60] D. O. Cheyne, "MEG studies of sensorimotor rhythms: A review," *Experimental Neurology*, vol. 245, pp. 27–39, 2013. 9

[61] M. Raghavan, D. Fee, and P. E. Barkhaus, *Generation and propagation of the action potential*, vol. 160. Elsevier B.V., 1 ed., 2019. 9

[62] S. Baillet, J. C. Mosher, and R. M. Leahy, "Sylvain Baillet, John C. Mosher, and Richard M. Leahy," no. November, 2001. 10

[63] D. B. Geselowitz, "On Bioelectric Potentials in an Inhomogeneous Volume Conductor," *Biophysical Journal*, vol. 7, no. 1, pp. 1–11, 1967. 10

[64] J. Clarke and A. I. Braginski, *The SQUID Handbook: Vol. I Fundamentals and Technology of SQUIDs and SQUID Systems*, vol. 1. 2005. 11, 18, 19

[65] D. A. Sholl, *The organization of the cerebral cortex.* Oxford, England: John Wiley, 1956. 11

[66] R. Hari, S. Baillet, G. Barnes, R. Burgess, N. Forss, J. Gross, M. Hämäläinen, O. Jensen, R. Kakigi, F. Mauguière, N. Nakasato, A. Puce, G. L. Romani, A. Schnitzler, and S. Taulu, "IFCN-endorsed practical guidelines for clinical magnetoencephalography (MEG)," *Clinical Neurophysiology*, vol. 129, no. 8, pp. 1720–1747, 2018. 11

[67] E. Diaz and H. Morales, "Spinal Cord Anatomy and Clinical Syndromes," *Seminars in Ultrasound, CT and MRI*, vol. 37, no. 5, pp. 360–371, 2016. 14, 69, 81

[68] M. Al-Chalabi and S. Gupta, "Neuroanatomy, Spinothalamic Tract," *StatPearls*, pp. 1–5, 2019. 15, 16

[69] T. Tamaki and S. Kubota, "History of the development of intraoperative spinal cord monitoring," *European Spine Journal*, vol. 16, no. SUPPL. 2, pp. 140–146, 2007. 16, 69, 70, 87

[70] J. Bork, H. Hahlbohm, R. Klein, A. Schnabel, *et al.*, "The 8-layered magnetically shielded room of the ptb: Design and construction," in *Biomag2000, Proc. 12th Int. Conf. on Biomagnetism*, pp. 970–73, Citeseer, 2001. 16

[71] A. Borna, T. R. Carter, J. D. Goldberg, A. P. Colombo, Y.-Y. Jau, C. Berry, J. McKay, J. Stephen, M. Weisend, and P. D. D. Schwindt, "A 20-channel

magnetoencephalography system based on optically pumped magnetometers," *Physics in Medicine &amp Biology*, vol. 62, pp. 8909–8923, nov 2017. 16, 54

[72] D. Budker and D. F. Jackson Kimball, "Optical magnetometry," *Optical Magnetometry*, vol. 9781107010, pp. 1–430, 2013. 17, 21

[73] S. Singh, "Magnetoencephalography: Basic principles," *Annals of Indian Academy of Neurology*, vol. 17, no. 5, p. 107, 2014. 18

[74] R. C. Burgess, "Recognizing and Correcting MEG Artifacts.," *Journal of clinical neurophysiology : official publication of the American Electroencephalographic Society*, vol. 37, pp. 508–517, nov 2020. 18

[75] V. Pizzella, S. Della Penna, C. Del Gratta, and G. L. Romani, "SQUID systems for biomagnetic imaging," *Superconductor Science and Technology*, vol. 14, no. 7, 2001. 18, 19, 53

[76] B. D. Josephson, "Possible new effects in superconductive tunnelling," *Physics Letters*, vol. 1, no. 7, p. 251, 1962. 19

[77] J. E. T. Knuutila, A. I. Ahonen, M. S. Hämäläinen, M. J. Kajola, P. P. Laine, O. V. Lounasmaa, L. T. Parkkonen, J. T. A. Simola, and C. D. Tesche, "A 122-channel whole-cortex SQUID system for measuring the brain's magnetic fields," *IEEE transactions on mangetics*, vol. 29, no. 6, pp. 3315–3320, 1993. 19

[78] K. Sata, S. Fujimoto, N. Fukui, E. Haraguchi, T. Kido, K. Nishiguchi, and Y. Kang, "A 61-channel squid system for meg measurement cooled by a gm/jt cryocooler," *IEEE Transactions on Applied Superconductivity*, vol. 7, no. 2, pp. 2526–2529, 1997. 19

[79] Y. Adachi, M. Miyamoto, J. Kawai, G. Uehara, H. Ogata, S. Kawabata, K. Sekihara, and H. Kado, "Improvement of squid magnetometer system for extending application of spinal cord evoked magnetic field measurement," *IEEE Transactions on Applied Superconductivity*, vol. 21, pp. 485–488, June 2011. 19

[80] N. Coquelet, X. De Tiège, F. Destoky, L. Roshchupkina, M. Bourguignon, S. Goldman, P. Peigneux, and V. Wens, "Comparing MEG and high-density EEG for intrinsic functional connectivity mapping," *NeuroImage*, vol. 210, p. 116556, 2020. 19

[81] J. Gross, S. Baillet, G. R. Barnes, R. N. Henson, A. Hillebrand, O. Jensen, K. Jerbi, V. Litvak, B. Maess, R. Oostenveld, L. Parkkonen, J. R. Taylor, V. Van Wassenhove, M. Wibral, and J.-M. Schoffelen, "Comments and Controversies Good practice for conducting and reporting MEG research," *NeuroImage*, vol. 65, pp. 349–363, 2013. 19

[82] S. Masahiro, T. Hiroaki, K. Kunio, and H. Yasuhiro, "Megvision magnetoencephalograph system and its applications," 2004. 20

[83] J. C. Allred, R. N. Lyman, T. W. Kornack, and M. V. Romalis, "High-sensitivity atomic magnetometer unaffected by spin-exchange relaxation," *Phys. Rev. Lett.*, vol. 89, p. 130801, Sep 2002. 21, 23

[84] T. M. Tierney, N. Holmes, S. Mellor, J. D. López, G. Roberts, R. M. Hill, E. Boto, J. Leggett, V. Shah, M. J. Brookes, R. Bowtell, and G. R. Barnes, "Optically pumped magnetometers: From quantum origins to multi-channel magnetoencephalography," *NeuroImage*, vol. 199, no. December 2018, pp. 598–608, 2019. 21, 22

[85] W. HAPPER, "Optical pumping," *Rev. Mod. Phys.*, vol. 44, pp. 169–249, Apr 1972. 22

[86] W. Happer and H. Tang, "Spin-exchange shift and narrowing of magnetic resonance lines in optically pumped alkali vapors," *Phys. Rev. Lett.*, vol. 31, pp. 273–276, Jul 1973. 22

[87] V. Shah, S. Knappe, P. D. D. Schwindt, and J. Kitching, "Subpicotesla atomic magnetometry with a microfabricated vapour cell," *Nature Photonics*, vol. 1, no. 11, pp. 649–652, 2007. 23, 59

[88] E. Boto, R. Bowtell, P. Krüger, T. M. Fromhold, P. G. Morris, S. S. Meyer, G. R. Barnes, and M. J. Brookes, "On the potential of a new generation

of magnetometers for MEG: A beamformer simulation study," *PLoS ONE*, vol. 11, no. 8, pp. 1–16, 2016. 23, 27, 31, 39, 50, 100, 101

[89] N. V. Nardelli, S. P. Krzyzewski, and S. A. Knappe, "Reducing crosstalk in optically-pumped magnetometer arrays," *Physics in Medicine and Biology*, vol. 64, no. 21, pp. 1–8, 2019. 25, 54, 100

[90] S. N. Baker, G. Curio, and R. N. Lemon, "EEG oscillations at 600 Hz are macroscopic markers for cortical spike bursts," *Journal of Physiology*, vol. 550, no. 2, pp. 529–534, 2003. 25, 54

[91] B. S. Chander, M. Deliano, E. Azañon, L. Büntjen, and M.-P. Stenner, "Non-Invasive Recording of High-Frequency Signals from the Human Spinal Cord," *NeuroImage*, p. 119050, 2022. 25, 54, 69, 101

[92] A. Insola, L. Padua, P. Mazzone, and M. Valeriani, "Unmasking of presynaptic and postsynaptic high-frequency oscillations in epidural cervical somatosensory evoked potentials during voluntary movement," *Clinical Neurophysiology*, vol. 119, no. 1, pp. 237–245, 2008. 25, 54, 69, 101

[93] E. Boto, S. S. Meyer, V. Shah, O. Alem, S. Knappe, P. Kruger, T. M. Fromhold, M. Lim, P. M. Glover, P. G. Morris, R. Bowtell, G. R. Barnes, and M. J. Brookes, "A new generation of magnetoencephalography: Room temperature measurements using optically-pumped magnetometers," *NeuroImage*, vol. 149, no. January, pp. 404–414, 2017. 27, 33, 39, 50, 100, 101

[94] X. Zheng, G. Xu, K. Zhang, R. Liang, W. Yan, P. Tian, Y. Jia, S. Zhang, and C. Du, "Assessment of human visual acuity using visual evoked potential: A review," *Sensors (Switzerland)*, vol. 20, no. 19, pp. 1–26, 2020. 28

[95] "A visual encoding model links magnetoencephalography signals to neural synchrony in human cortex," *NeuroImage*, vol. 245, pp. 1–39, 2021. 28

[96] Y. W. Chan, J. G. McLeod, R. R. Tuck, J. C. Walsh, and P. A. Feary, "Visual evoked responses in chronic alcoholics.," *Journal of Neurology, Neurosurgery & Psychiatry*, vol. 49, no. 8, pp. 945–950, 1986. 29

[97] J. E. Arruda, M. C. McInnis, and J. Steele, "The flash visual evoked potential-p2 and the detection of amnestic mild cognitive impairment: A review of empirical literature," *International Journal of Psychophysiology*, vol. 155, pp. 162–167, 2020. 29

[98] D. A. Jeffreys and J. G. Axford, "Source locations of pattern-specific components of human visual evoked potentials. I. Component of striate cortical origin," *Experimental Brain Research*, vol. 16, no. 1, pp. 1–21, 1972. 29, 38, 44, 45, 47

[99] P. E. Roland, A. Hanazawa, C. Undeman, D. Eriksson, T. Tompa, H. Nakamura, S. Valentiniene, and B. Ahmed, "Cortical feedback depolarization waves: A mechanism of top-down influence on early visual areas," *Proceedings of the National Academy of Sciences of the United States of America*, vol. 103, no. 33, pp. 12586–12591, 2006. 29, 36

[100] W. Xu, X. Huang, K. Takagaki, and J.-y. Wu, "Compression and Reflection of Visually Evoked Cortical Waves," *Neuron*, vol. 55, no. 1, pp. 119–129, 2007. 29, 36, 37

[101] S. Vanni, T. Tanskanen, M. Seppä, K. Uutela, and R. Hari, "Coinciding early activation of the human primary visual cortex and anteromedial cuneus," *Proceedings of the National Academy of Sciences*, vol. 98, pp. 2776 LP —- 2780, feb 2001. 29

[102] J. J. Foxe, E. C. Strugstad, P. Sehatpour, S. Molholm, W. Pasieka, C. E. Schroeder, and M. E. McCourt, "Parvocellular and magnocellular contributions to the initial generators of the visual evoked potential: High-density electrical mapping of the "C1" component," *Brain Topography*, vol. 21, no. 1, pp. 11–21, 2008. 29, 38, 44, 45, 47

[103] F. Yoshida, M. Hirata, A. Onodera, T. Goto, H. Sugata, and S. Yorifuji, "Noninvasive spatiotemporal imaging of neural transmission in the subcortical visual pathway," *Scientific Reports*, vol. 7, no. 1, pp. 1–6, 2017. 29

[104] F. Di Russo, A. Martínez, M. I. Sereno, S. Pitzalis, and S. A. Hillyard, "Cortical sources of the early components of the visual evoked potential," *Human Brain Mapping*, vol. 15, no. 2, pp. 95–111, 2002. 29

[105] S. Tan, B. J. Roth, and J. P. Wikswo, "The magnetic field of cortical current sources: the application of a spatial filtering model to the forward and inverse problems," *Electroencephalography and Clinical Neurophysiology*, vol. 76, no. 1, pp. 73–85, 1990. 31

[106] J. H. Storm, P. Hömmen, D. Drung, and R. Körber, "An ultra-sensitive and wideband magnetometer based on a superconducting quantum interference device," *Applied Physics Letters*, vol. 110, no. 7, 2017. 32

[107] B. Hochwald and A. Nehorai, "Magnetoencephalography with diversely oriented and multicomponent sensors," *IEEE Transactions on Biomedical Engineering*, vol. 44, no. 1, pp. 40–50, 1997. 33

[108] S. Warrington, K. L. Bryant, A. A. Khrapitchev, J. Sallet, M. Charquero-Ballester, G. Douaud, S. Jbabdi, R. B. Mars, and S. N. Sotiropoulos, "XTRACT - Standardised protocols for automated tractography in the human and macaque brain," *NeuroImage*, vol. 217, p. 116923, 2020. 34

[109] T. Sander, A. Jodko-Władzińska, S. Hartwig, R. Brühl, and T. Middelmann, "Optically pumped magnetometers enable a new level of biomagnetic measurements," 2020. 34, 80

[110] J. V. Odom, M. Bach, M. Brigell, G. E. Holder, D. L. McCulloch, A. Mizota, and A. P. Tormene, "ISCEV standard for clinical visual evoked potentials: (2016 update)," *Documenta Ophthalmologica*, vol. 133, no. 1, pp. 1–9, 2016. 34

[111] L. Koessler, L. Maillard, A. Benhadid, J. P. Vignal, J. Felblinger, H. Vespignani, and M. Braun, "Automated cortical projection of EEG sensors: Anatomical correlation via the international 10-10 system," *NeuroImage*, vol. 46, no. 1, pp. 64–72, 2009. 36, 59, 81

[112] R. Oostenveld, P. Fries, E. Maris, and J.-M. Schoffelen, "FieldTrip: Open Source Software for Advanced Analysis of MEG, EEG, and Invasive Electrophysiological Data," *Computational Intelligence and Neuroscience*, vol. 2011, p. 156869, 2011. 37, 85

[113] H. Pratt, N. Bleich, and W. H. Martin, "Short latency visual evoked potentials to flashes from light-emitting diodes," *Electroencephalography and Clinical Neurophysiology/ Evoked Potentials*, vol. 96, no. 6, pp. 502–508, 1995. 38, 44, 45, 47

[114] R. Sharma, S. Joshi, K. D. Singh, and A. Kumar, "Visual evoked potentials: Normative values and gender differences," *Journal of Clinical and Diagnostic Research*, vol. 9, no. 7, pp. 12–15, 2015. 38, 44, 45, 47

[115] K. L. Coburn, R. T. Amoss, J. E. Arruda, L. D. Kizer, and Y. S. Marshall, "Effects of flash mode and intensity on P2 component latency and amplitude," *International Journal of Psychophysiology*, vol. 55, no. 3, pp. 323–331, 2005. 38, 44, 45, 47

[116] G. S. Brindley, "The variability of the human striate cortex.," *The Journal of physiology*, vol. 225, no. 2, pp. 1P–3P, 1972. 43, 61

[117] S. P. Ahlfors, G. V. Simpson, A. M. Dale, J. W. Belliveau, A. K. Liu, A. Korvenoja, J. Virtanen, M. Huotilainen, R. B. Tootell, H. J. Aronen, and R. J. Ilmoniemi, "Spatiotemporal activity of a cortical network for processing visual motion revealed by MEG and fMRI," *Journal of Neurophysiology*, vol. 82, no. 5, pp. 2545–2555, 1999. 43, 61

[118] C. Babiloni, K. Blinowska, L. Bonanni, A. Cichocki, W. De Haan, C. Del Percio, B. Dubois, J. Escudero, A. Fernández, G. Frisoni, B. Guntekin, M. Hajos, H. Hampel, E. Ifeachor, K. Kilborn, S. Kumar, K. Johnsen, M. Johannsson, J. Jeong, F. LeBeau, R. Lizio, F. Lopes da Silva, F. Maestú, W. J. McGeown, I. McKeith, D. V. Moretti, F. Nobili, J. Olichney, M. Onofrj, J. J. Palop, M. Rowan, F. Stocchi, Z. M. Struzik, H. Tanila, S. Teipel, J. P. Taylor, M. Weiergräber, G. Yener, T. Young-Pearse, W. H. Drinkenburg, and F. Randall, "What electrophysiology tells us about Alzheimer's disease: a window

into the synchronization and connectivity of brain neurons.," *Neurobiology of aging*, vol. 85, pp. 58–73, jan 2020. 51

[119] E. Boto, Z. A. Seedat, N. Holmes, J. Leggett, R. M. Hill, G. Roberts, V. Shah, T. M. Fromhold, K. J. Mullinger, T. M. Tierney, G. R. Barnes, R. Bowtell, and M. J. Brookes, "Wearable neuroimaging: Combining and contrasting magnetoencephalography and electroencephalography.," *NeuroImage*, vol. 201, p. 116099, nov 2019. 52

[120] T. Ryhänen, H. Seppä, R. Ilmoniemi, and J. Knuutila, "SQUID magnetometers for low-frequency applications," *J. Low Temp. Phys.*, vol. 76, pp. 287–386, Sept. 1989. 53

[121] T. H. Sander, J. Preusser, R. Mhaskar, J. Kitching, L. Trahms, and S. Knappe, "Magnetoencephalography with a chip-scale atomic magnetometer," *Biomedical Optics Express*, vol. 3, no. 5, p. 981, 2012. 54

[122] A. P. Colombo, T. R. Carter, A. Borna, Y.-Y. Jau, C. N. Johnson, A. L. Dagel, and P. D. D. Schwindt, "Four-channel optically pumped atomic magnetometer for magnetoencephalography," *Optics Express*, vol. 24, no. 14, p. 15403, 2016. 54

[123] N. Shamim, Y. P. Koh, S. L. Simon, and G. B. McKenna, "Glass transition temperature of thin polycarbonate films measured by flash differential scanning calorimetry," *J. Polym. Sci. B Polym. Phys.*, vol. 52, pp. 1462–1468, Nov. 2014. 55

[124] J. C. Allred, R. N. Lyman, T. W. Kornack, and M. V. Romalis, "High-Sensitivity Atomic Magnetometer Unaffected by Spin-Exchange Relaxation," *Physical Review Letters*, vol. 89, p. 130801, Sept. 2002. 56

[125] W. Klimesch, "Alpha-band oscillations, attention, and controlled access to stored information," *Trends in Cognitive Sciences*, vol. 16, no. 12, pp. 606–617, 2012. 60, 101

[126] D. Lozano-Soldevilla, "On the physiological modulation and potential mech-

anisms underlying parieto-occipital alpha oscillations," *Frontiers in Computational Neuroscience*, vol. 12, no. April, pp. 1–19, 2018. 60, 101

[127] M. Moccia, S. Ruggieri, A. Ianniello, A. Toosy, C. Pozzilli, and O. Ciccarelli, "Advances in spinal cord imaging in multiple sclerosis.," *Therapeutic advances in neurological disorders*, vol. 12, p. 1756286419840593, 2019. 69

[128] M. M. El Mendili, G. Querin, P. Bede, and P.-F. Pradat, "Spinal Cord Imaging in Amyotrophic Lateral Sclerosis: Historical Concepts-Novel Techniques.," *Frontiers in neurology*, vol. 10, p. 350, 2019. 69

[129] N. Fati, G. Fitiwi, A. Aynalem, and A. Muche, "Depth of spinal needle insertion and its associated factors among patients who underwent surgery under spinal anesthesia," *Translational Research in Anatomy*, vol. 25, no. May, p. 100143, 2021. 69

[130] T. Tamaki, T. Noguchi, H. Takano, H. Tsuji, T. Nakagawa, K. Imai, and S. Inoue, "Spinal cord monitoring as a clinical utilization of the spinal evoked potential," 1984. 70, 87

[131] I. Štětkářová, J. A. Halter, and M. R. Dimitrijevic, "Surface and Epidural Lumbosacral Spinal Cord Evoked Potentials in Chronic Spinal Cord Injury," *Journal of Neurotrauma*, vol. 10, no. 3, pp. 315–326, 1993. 70

[132] M. R. Nuwer and L. M. Schrader, *Spinal cord monitoring*, vol. 160. Elsevier B.V., 1 ed., 2019. 70

[133] B. M. Mackert, M. Burghoff, L. H. Hiss, M. Nordahn, P. Marx, L. Trahms, and G. Curio, "Magnetoneurography of evoked compound action currents in human cervical nerve roots," *Clinical Neurophysiology*, vol. 112, no. 2, pp. 330–335, 2001. 70

[134] M. Akaza, S. Kawabata, I. Ozaki, Y. Miyano, T. Watanabe, Y. Adachi, K. Sekihara, Y. Sumi, and T. Yokota, "Noninvasive measurement of sensory action currents in the cervical cord by magnetospinography," *Clinical Neurophysiology*, vol. 132, no. 2, pp. 382–391, 2021. 70

[135] M. A. Moffitt, B. M. Dale, J. L. Duerk, and W. M. Grill, "Functional magnetic resonance imaging of the human lumbar spinal cord," *Journal of Magnetic Resonance Imaging*, vol. 21, no. 5, pp. 527–535, 2005. 70

[136] Y. Kong, F. Eippert, C. F. Beckmann, J. Andersson, J. Finsterbusch, C. Büchel, I. Tracey, and J. C. Brooks, "Intrinsically organized resting state networks in the human spinal cord," *Proceedings of the National Academy of Sciences of the United States of America*, vol. 111, no. 50, pp. 18067–18072, 2014. 70

[137] M. R. Dimitrijevic, L. D. Lehmkuhl, E. M. Sedgwick, A. M. Sherwood, and W. B. McKay, "Characteristics of spinal cord-evoked responses in man," *Applied Neurophysiology*, vol. 43, no. 3-5, pp. 118–127, 1980. 70, 71

[138] K. Shimoji, H. Higashi, and T. Kano, "Epidural recording of spinal electrogram in man," *Electroencephalography and Clinical Neurophysiology*, vol. 30, no. 3, pp. 236–239, 1971. 70, 87

[139] M. R. Nuwer and E. Dawson, "Intraoperative evoked potential monitoring of the spinal cord: Enhanced stability of cortical recordings," *Electroencephalography and Clinical Neurophysiology/ Evoked Potentials*, vol. 59, no. 4, pp. 318–327, 1984. 70

[140] F. Wang, L. Zhang, L. Yue, Y. Zeng, Q. Zhao, Q. Gong, J. Zhang, D. Liu, X. Luo, X. Xia, L. Wan, and L. Hu, "A novel method to simultaneously record spinal cord electrophysiology and electroencephalography signals," *NeuroImage*, vol. 232, no. February, 2021. 70

[141] D. G. Small, W. B. Matthews, and M. Small, "The cervical somatosensory evoked potential (SEP) in the diagnosis of multiple sclerosis," *Journal of the Neurological Sciences*, vol. 35, no. 2-3, pp. 211–224, 1978. 70

[142] D. Norman, C. M. Mills, M. Brant-Zawadzki, A. Yeates, L. E. Crooks, and L. Kaufman, "Magnetic resonance imaging of the spinal cord and canal: Potentials and limitations," *American Journal of Neuroradiology*, vol. 5, no. 1, pp. 9–14, 1984. 71

[143] H. Iwasaki, T. Tamaki, M. Yoshida, M. Ando, H. Yamada, S. Tsutsui, and M. Takami, "Efficacy and limitations of current methods of intraoperative spinal cord monitoring," *Journal of Orthopaedic Science*, vol. 8, no. 5, pp. 635–642, 2003. 71

[144] S. Harita and P. W. Stroman, "Confirmation of resting-state bold fluctuations in the human brainstem and spinal cord after identification and removal of physiological noise," *Magnetic Resonance in Medicine*, vol. 78, no. 6, pp. 2149–2156, 2017. 71

[145] G. Cruccu, M. J. Aminoff, G. Curio, J. M. Guerit, R. Kakigi, F. Mauguiere, P. M. Rossini, R. D. Treede, and L. Garcia-Larrea, "Recommendations for the clinical use of somatosensory-evoked potentials," *Clinical Neurophysiology*, vol. 119, no. 8, pp. 1705–1719, 2008. 80, 81

[146] R. Kakigi, "Somatosensory evoked magnetic fields following median nerve stimulation," *Neuroscience Research*, vol. 20, no. 2, pp. 165–174, 1994. 85

[147] S. Ali, P. Balaji, K. Kutty, S. Poornima, and V. Shankar, "Median nerve somatosensory evoked potentials in medical students: Normative data," *Advanced Biomedical Research*, vol. 2, no. 1, p. 56, 2013. 85

[148] C. Kany and R. D. Treede, "Median and tibial nerve somatosensory evoked potentials: Middle-latency components from the vicinity of the secondary somatosensory cortex in humans," *Electroencephalography and Clinical Neurophysiology - Evoked Potentials*, vol. 104, no. 5, pp. 402–410, 1997. 85

[149] R. Kakigi, S. Koyama, M. Hoshiyama, M. Shimojo, Y. Kitamura, and S. Watanabe, "Topography of somatosensory evoked magnetic fields following posterior tibial nerve stimulation," *Electroencephalography and Clinical Neurophysiology*, vol. 95, no. 2, pp. 127–134, 1995. 85

[150] J.-P. Lefaucheur, "Transcranial magnetic stimulation.," *Handbook of clinical neurology*, vol. 160, pp. 559–580, 2019. 104

[151] M. Q. Hameed, S. C. Dhamne, R. Gersner, H. L. Kaye, L. M. Oberman, A. Pascual-Leone, and A. Rotenberg, "Transcranial Magnetic and Direct Cur-

rent Stimulation in Children.," *Current neurology and neuroscience reports*, vol. 17, p. 11, feb 2017. 104

[152] M. C. Eldaief, D. Z. Press, and A. Pascual-Leone, "Transcranial magnetic stimulation in neurology: A review of established and prospective applications.," *Neurology. Clinical practice*, vol. 3, pp. 519–526, dec 2013. 104

[153] T. J. Schwedt and B. Vargas, "Neurostimulation for Treatment of Migraine and Cluster Headache.," *Pain medicine (Malden, Mass.)*, vol. 16, pp. 1827–1834, sep 2015. 104

[154] M. M. Klein, R. Treister, T. Raij, A. Pascual-Leone, L. Park, T. Nurmikko, F. Lenz, J.-P. Lefaucheur, M. Lang, M. Hallett, M. Fox, M. Cudkowicz, A. Costello, D. B. Carr, S. S. Ayache, and A. L. Oaklander, "Transcranial magnetic stimulation of the brain: guidelines for pain treatment research.," *Pain*, vol. 156, pp. 1601–1614, sep 2015. 104